

AGN EVOLUTION REVEALED FROM X-RAY SURVEYS

Yoshihiro Ueda

Department of Astronomy, Kyoto University, 606-8502 Kyoto, Japan

ABSTRACT

I review the cosmological evolution of Active Galactic Nuclei (AGNs) revealed from X-ray surveys, mainly based on studies by using hard (>2 keV) X-ray selected samples. The hard X-ray luminosity function of type-1 and type-2 AGNs is well described by the luminosity dependent density evolution, where the cut-off redshift of density evolution increases with luminosity. This suggest anti-hierarchical (or down-sizing) growth of supermassive black holes in galactic centers. The black hole mass function at $z < 1$ can be explained, on average, as the consequence of “standard” accretion with a radiative efficiency of ≈ 0.1 . Population synthesis models constructed from the observational results of hard X-ray luminosity function and absorption function of AGNs are now close to finalization. However, toward complete understanding of the X-ray background origin, there still remains several issues to be solved by current and future missions.

Key words: X-rays; AGN; Surveys; X-ray Background.

1. INTRODUCTION

The X-ray background (XRB) is the integration of emission from all accreting black holes in the universe, and hence carries key information on the growth history of supermassive black holes (SMBHs) in galactic centers. The tight correlation between bulge mass and black-hole mass in the local universe indicates a strong link between formation of stars and that of SMBHs. Thus, revealing the accretion history of SMBHs is a crucial issue, to which X-ray astronomy should give a definitive answer, for understanding the whole history of the universe including galaxy formation processes.

To solve the XRB origin is equivalent to revealing the cosmological evolution of AGNs that constitute the XRB. Since the discovery of the XRB in 1962, efforts to resolve the XRB by surveys with increasing sensitivities have been main stream of extra-galactic X-ray astronomy. Figure 1 shows a summary of $\log N \log S$ relations in the

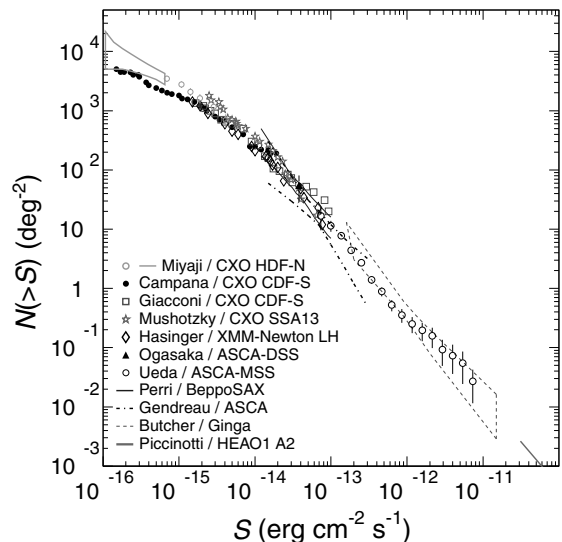


Figure 1. $\log N \log S$ relations in the 2–10 keV band obtained from various X-ray surveys. Compiled by Kushino *et al.* (2002).

2–10 keV band determined with various hard X-ray satellites. Thanks to the heritage from past X-ray satellites together with the recent missions, Chandra and XMM-Newton, that have mostly resolved the faintest part of the XRB, we can now have the entire picture for the evolution of AGNs contributing to the XRB radiation. The most fundamental observational quantity describing the AGN evolution is a “luminosity function”, the co-moving space density given as a function of luminosity and redshift. In order to determine an X-ray AGN luminosity function, straightforward but very time consuming work is required: we need to resolve the XRB into discrete AGNs, define statistical samples, and measure the redshift of each object as complete as possible, usually by means of optical spectroscopic observations.

The “hard” shape of the XRB spectrum, whose energy

density peaks around 30 keV, indicates that the majority of AGNs should be absorbed in X-rays. Hard X-ray surveys provide one of the most efficient and complete methods to pick up major AGN populations, since hard X-rays are much less affected by absorption or by dilution from star light in the host galaxy compared with soft X-rays or visible lights. X-ray absorbed AGNs are in most cases optical type-2 AGNs (i.e., those not showing broad emission lines) as expected from the unified scheme (Awaki et al., 1991), although the classification does not always match between in the X-ray and optical bands (e.g., Maiolino et al. 2001). Table 1 lists surveys conducted in hard X-ray band ($\gtrsim 3$ keV) with optical identification program in bright to medium flux range ($10^{-11} - 10^{-15}$ erg cm $^{-2}$ s $^{-1}$ in the 2–10 keV band). For comparison, the detection limit of each survey band is converted into the 2–10 keV flux by assuming a typical AGN spectrum of detected sources. (The list of “deep” surveys with Chandra and XMM is given in Table 1 of Brandt & Hasinger 2005.) Hard X-ray surveys can trace the evolution of both type-1 and type-2 AGNs and their number ratio as a function of luminosity and redshift. On the other hand, soft X-ray surveys generally reach fainter flux limits, although they are subject to biases against type-2 AGNs. Thus, hard-band and soft-band surveys are quite complementary each other. The latest result on soft X-ray luminosity function (SXLf) of type-1 AGNs is presented in Hasinger et al. (2005).

2. HARD X-RAY LUMINOSITY FUNCTION

To determine an X-ray AGN luminosity function in the wide luminosity and redshift range, it is important to use a combination of multiple surveys with different flux limits and survey area, in order to decouple luminosity and redshift dependences. Another key point is identification completeness of the sample used in the analysis. Figure 2 shows the correlation between hard X-ray and R-band fluxes for hard X-ray selected AGNs. As noticed, a significant fraction of X-ray sources with fluxes of $\sim 10^{-13}$ erg cm $^{-2}$ s $^{-1}$ (2–10 keV) have optical magnitudes of $R > 24$, for which spectroscopic identification is difficult even with 8-m class telescopes. This fact makes accurate determination of hard X-ray luminosity function (HXLf) more challenging than in soft X-rays. Several methods are adopted by different groups to correct for incompleteness in the calculation of HXLf:

1. Use only samples with high ($> 90\%$) completeness (Ueda et al. 2003, hereafter U03; Hasinger et al. 2005).
2. Obtain absolute upper limits on the AGN number density by putting all the unidentified sources at each redshift, although the limit may become not very constraining if the completeness is relatively low (see e.g., Cowie et al. 2003).
3. Consider optical and X-ray flux limit in the volume calculation (Hasinger et al., 2005).

Table 1. List of Hard X-ray Surveys in Bright to Medium Flux Range

Survey	Flux limit erg cm $^{-2}$ s $^{-1}$ (2–10 keV)	ref.
HEAO1 A2	3×10^{-11}	1
HEAO1 A1	2×10^{-11}	2
RXTE ASM	1×10^{-11}	3
Integral	$\approx 10^{-11}$	4
Swift BAT	$\approx 10^{-11} - 10^{-12}$	5
XMM Slew	4×10^{-12}	6
ASCA MSS	3×10^{-13}	7
ASCA LSS	1×10^{-13}	8
BeppoSAX HELLAS	1×10^{-13}	9
XMM Bright	9×10^{-14}	10
ASCA Deep	4×10^{-14}	11
XMM Medium	2×10^{-14}	12
XMM LSS	2×10^{-14}	13
Chandra LSS	$\approx 10^{-14}$	14
HELASS2XMM	8×10^{-15}	15
CLASXS	4×10^{-15}	16
ChaMP	3×10^{-15}	17
CYDER	2×10^{-15}	18
SEXSI	$\approx 10^{-15}$	19
Chandra/XMM Deep	$10^{-15} - 2 \times 10^{-16}$	20

References: 1. Piccinotti et al. (1982) 2. Grossan (1992) 3. Revnivtsev et al. (2004) 4. Beckmann et al. (2005) 5. Markwardt et al. (2005) 6. Saxton et al. (2005) 7. Ueda et al. (2001; 2005) 8. Ueda et al. (1999) 9. Fiore et al. (1999) 10. Della Ceca et al. (2004) 11. Ishisaki et al. (2001), Ohta et al. (2003) 12. Barcons et al. (2002) 13. Chiappetti et al. (2005) 14. Murray et al. (2004) 15. Fiore et al. (2003) 16. Steffen et al. (2004) 17. Kim et al. (2004) 18. Treister et al. (2005) 19. Harrison et al. (2003) 20. Brandt & Hasinger (2005) and references therein

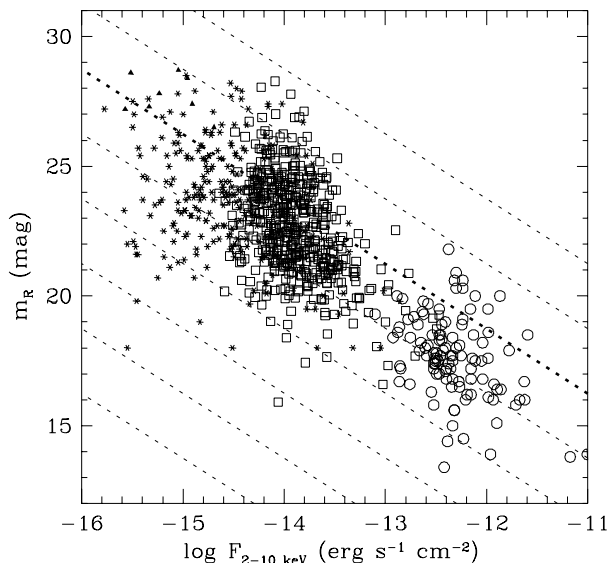


Figure 2. The 2–10 keV flux versus R-band magnitude diagram for hard X-ray selected samples. Asterisk: from Chandra deep field north (Barger et al., 2003) and Chandra deep field south (Szokoly et al., 2004). Squares: from the Subaru-XMM deep survey (Akiyama et al., in prep). Circles: from ASCA surveys (Akiyama et al. 2000; Akiyama et al. 2003).

4. Make area correction in the X-ray flux versus optical flux plane. In this method there is an implicit assumption that the unidentified sources have the same redshift distribution of that of identified sources. Adopted by Silverman et al. (2005).
5. Consider the correlation between X-ray luminosity and optical luminosity. There is an implicit assumption that the same correlation found from low redshift objects holds at higher redshift. Adopted by La Franca et al. (2005).

Studies using hard X-ray selected AGNs reveal that the comoving space density of AGNs (type-1 and type-2) shows evolution that differs with luminosity range (e.g., Cowie et al. 2003, Fiore et al. 2003, U03, Steffen et al. 2003). With a highly complete hard X-ray selected sample consisting of 243 AGNs detected with HEAO-1, ASCA, and Chandra, U03 have found that the overall AGN evolution in the luminosity range of $\text{Log } L_X = 41.5 - 46.5$ over $z=0-3$ can be well described by the luminosity dependent density evolution (LDDE), where the cutoff redshift above which the density evolution terminates increases with luminosity. Representing the present-day HXLF with smoothly-connected two power-law form,

$$\frac{d\Phi(L_X, z=0)}{d\text{Log}L_X} = A[(L_X/L_*)^{\gamma_1} + (L_X/L_*)^{\gamma_2}]^{-1}, \quad (1)$$

they model the evolution as

$$\frac{d\Phi(L_X, z)}{d\text{Log}L_X} = \frac{d\Phi(L_X, 0)}{d\text{Log}L_X} e(z, L_X), \quad (2)$$

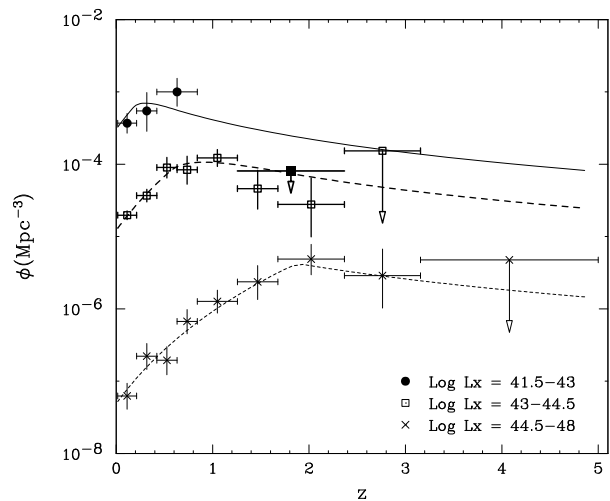


Figure 3. The comoving spatial density of AGNs as a function of redshift in three luminosity ranges, $\text{Log } L_X = 41.5-43$ (upper), $43-44.5$ (middle), $44.5-48$ (lower), taken after U03. The lines are calculated from their best-fit HXLF. The errors are 1σ , while the long arrows denote the 90% upper limits (corresponding to 2.3 objects). The short arrow (marked with a filled square, red) corresponds to the 90% upper limit on the average spatial density of AGNs with $\text{Log } L_X = 43-44.5$ at $z=1.2-2.3$ when all the unidentified sources are assumed to be in this redshift bin.

where

$$e(z, L_X) = \begin{cases} (1+z)^{p1} & (z \leq z_c(L_X)) \\ e(z_c) \left(\frac{1+z}{1+z_c(L_X)} \right)^{p2} & (z > z_c(L_X)) \end{cases}$$

and the cut-off redshift can be approximated as

$$z_c(L_X) = \begin{cases} z_c^* & (L_X \geq L_a) \\ z_c^* (L_X/L_a)^\alpha & (L_X < L_a) \end{cases}$$

The best-fit parameters obtained by U03 are $A = 5.04 \pm 0.33 [10^{-6} h_{70}^3 \text{ Mpc}^{-3}]$, $\text{Log } L_* = 43.94^{+0.21}_{-0.26}$, $\gamma_1 = 0.86 \pm 0.15$, $\gamma_2 = 2.23 \pm 0.13$, $p1 = 4.23 \pm 0.39$, $\alpha = 0.335 \pm 0.070$ for fixed values of $p2 = -1.5$, $z_c^* = 1.9$, and $\text{Log } L_a = 44.6$. Figure 3 shows the comoving spatial density of all Compton-thin AGNs as a function of redshift in different luminosity ranges. This behavior is essentially confirmed by La Franca et al. (2005) who added the CDFS and HELLAS2XMM samples in the similar analysis. The LDDE also gives a good representation of the SXLF of type-1 AGNs (Hasinger et al., 2005), as shown earlier by Miyaji et al. (2000) but with slightly different parameterization. Barger et al. (2005) argue that the HXLF at $z < 1.2$ is consistent with pure luminosity evolution (PLE), which is often used to model optical luminosity functions of type-1 quasars (e.g., Croom et al. 2004). The PLE does not, however, describe the overall evolution of XLF in the wider redshift range from $z = 0$ to $z=3-5$ (e.g., U03; Hasinger et al. 2005).

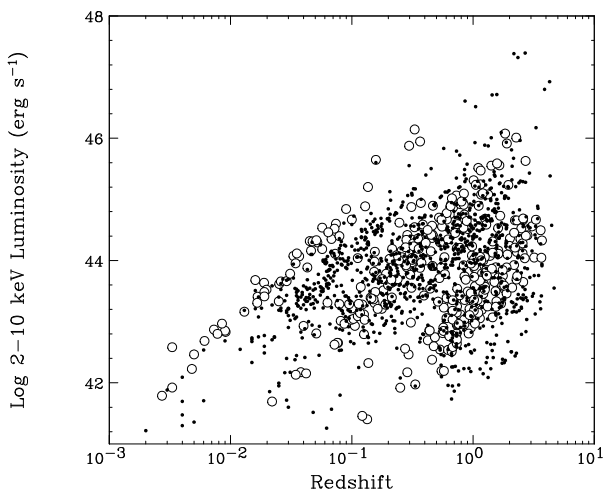


Figure 4. The redshift versus luminosity plot for the soft+hard combined sample. The luminosity L_X is an “intrinsic” one in the rest frame 2–10 keV band before being absorbed. Filled circles: soft-band selected AGNs. Open circles: hard-band selected AGNs.

To determine the AGN XLF in the rest frame 2–10 keV band with the best accuracy, a combined analysis using both hard-band and soft-band selected AGNs is now ongoing (Ueda et al. in prep.). The combined sample consists of 1341 sources in total selected from extended samples used in U03 and Hasinger et al. (2005). We utilize a maximum likelihood method to reproduce the count-rate versus redshift distribution for each survey, taking account of all selection effects. Figure 4 shows the redshift-luminosity diagram of the combined sample. The best-fit XLF is plotted in Figure 5 for different redshift ranges.

The LDDE of AGNs, where the peak redshift increases with luminosity, indicates that SMBHs finally growing to larger mass formed earlier than smaller mass ones. This fact is apparently contradictory to a naive expectation from the standard, hierarchical structure-formation theory of the universe where larger mass dark halo formed later as the consequence of bottom-up growth. Thus, the AGN evolution is called “anti-hierarchical” growth or “down-sizing”. Note that evidence for down-sizing is also seen in the star-formation history (e.g., Cowie et al. 1996, Heavens et al. 2004, Kodama et al. 2004). These results challenge theories of SMBH and galaxy formation, requiring consideration of physical processes of baryons, such as feedback of AGNs and/or supernova to the accretion and star formation. Several theoretical models or simulations that reproduce the anti-hierarchical evolution have been proposed (e.g., Di Matteo et al. 2003, Granato et al. 2004, Hopkins et al. 2005).

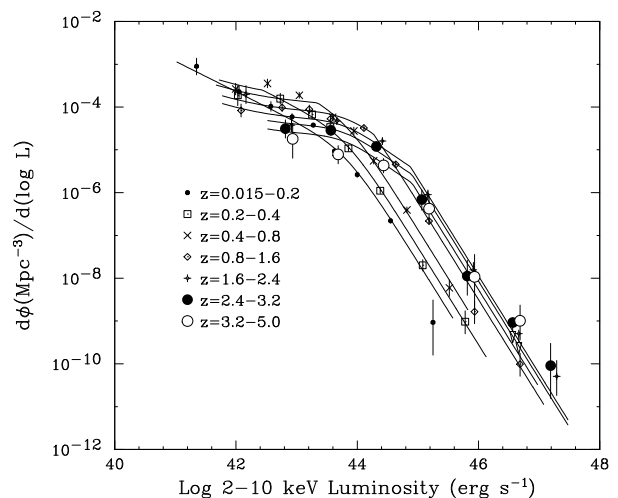


Figure 5. The intrinsic 2–10 keV luminosity function of all the Compton-thin AGNs determined from the combined analysis of the hard and soft X-ray selected samples. The curves represent the best-fit LDDE model. The data are plotted with 1σ Poisson errors.

3. LUMINOSITY DEPENDENCE OF THE ABSORBED-AGN FRACTION

The ratio of absorbed to unabsorbed AGNs (or optical type-1 to type-2 AGNs) is another key issue for AGN evolution, which is described by the column-density distribution function (N_H function; see U03). U03 find from their hard X-ray selected sample that the fraction of absorbed AGNs ($\text{Log } N_H < 22$) in the total (Compton-thin) AGNs decreases with luminosity. The trend was pointed out by Lawrence & Elvis (1982), and is consistent with the deficiency of luminous, absorbed AGNs in the ASCA and HEAO1 surveys (e.g., Akiyama et al. 2000; Shinozaki et al. 2005). Similarly, the fraction of optical type-1 AGNs in total AGNs also decreases at low luminosity (Steffen et al. 2003; Barger et al. 2005). The result indicates that simple extension of the “unified scheme” to higher luminosity where the fraction of absorbed AGNs is assumed to be constant needs to be modified, and is consistent with population synthesis of the XRB (U03; Treister & Urry 2005). In addition to the luminosity dependence, La Franca et al. (2005) recently claim that the absorbed-AGN fraction increases toward higher redshift.

4. THE ACCRETION HISTORY OF THE UNIVERSE

The HXLF of type-1 and type-2 AGNs provides strong observational constraints on the growth history of SMBHs through accretion. The bolometric luminosity L_{bol} of an AGN is related to the mass accretion rate through the mass-to-energy conversion factor ϵ as

$$L_{\text{bol}}(\equiv \eta L_{\text{Edd}}) = \epsilon \dot{M} c^2. \quad (3)$$

Here η is the Eddington ratio. As argued by Soltan (1982), the evolution of total accreted mass density, $\rho(z)$, is related to the HXLF as

$$\rho(z) = \int_{z_{\max}}^z \frac{(1-\epsilon)\dot{\lambda}(z)}{\epsilon c^2} \left(\frac{dt}{dz}\right) dz, \quad (4)$$

where

$$\dot{\lambda}(z) = \int L_{\text{bol}} \Phi(L_X, z) d\text{Log} L_X \quad (5)$$

is the comoving bolometric luminosity density. Thus, comparison of $\rho(0)$ with the local black hole mass density independently estimated from the $M-\sigma$ relation can be used to constrain ϵ . It is essential to use a luminosity function of all AGNs including type-2 objects, otherwise $\rho(z)$ would be significantly underestimated. Previous studies (Salluci et al. 1999; Elvis et al. 2002), estimated $\rho(0)$ from the hard XRB intensity assuming a single effective redshift for the XRB sources. Now the HXLF has been observationally determined, which enables us to obtain $\rho(z)$ more accurately by integrating the formula (4).

To calculate $\dot{\lambda}$, an X-ray luminosity must be converted to a bolometric one, L_{bol} . This correction is an issue, however, because the spectral energy distribution (SED) of AGNs has large scatter, depends on luminosity, and could be affected by selection biases in the survey band (see the discussion in Hasinger 2005). Phenomenological models for AGN SED are proposed by e.g., Marconi et al. (2004) and Shankar et al. (2004). Here, assuming the relation $L_X \propto L_B^{0.9}$ between the 2–10 keV and B-band luminosity obtained from a large X-ray selected sample (Anderson et al., 2003), we consider two extreme cases: the bolometric luminosity is proportional to the B-band luminosity, $L_{\text{bol}} = 11.8\nu_B L_B [= 4.5 \times 10^{45} (\frac{L_X}{10^{44}})^{1/0.9}]$ (case I), where ν_B is the B-band frequency, and to the 2–10 keV luminosity, $L_{\text{bol}} = 30L_X$ (case II). The correction factors are based on the averaged spectrum of quasars compiled by Elvis et al. (1994). The difference between the two cases would give an estimate for the uncertainty in the bolometric correction.

Figure 6 shows the results of $\dot{\lambda}(z)$ and $\rho(z)$ obtained from the U03 HXLF (thick lines for case I and thin lines for case II) by assuming $\epsilon = 0.1$ and $z_{\max} = 5$. The dashed lines correspond to the case when 1.6 times as many Compton-thick AGNs as those with $\text{Log } N_{\text{H}} = 23\text{--}24$ are included according to the result by Risaliti et al. (1999). Compared with the results of $\rho(z)$ by Yu & Tremaine (2002), where the optical luminosity function of type-1 quasars by Boyle et al. (2000) is utilized, the mass growth continues more significantly after $z < 1$, owing to the contribution from absorbed, low luminosity AGNs. The estimated total accreted mass density is $\rho(0) = (2.2 - 5.3) \times 10^5 \text{ M}_{\odot} \text{Mpc}^{-3}$, in agreement with that of the local black hole mass density of $(4.2 \pm 1.1) \times 10^5 \text{ M}_{\odot} \text{Mpc}^{-3}$ (Shankar et al., 2004). Further, Marconi et al. (2004) compared the accreted black hole mass function (BHMF) derived from the continuity equation with the local BHMF, and obtained that $\epsilon \approx 0.1$ and $\eta \approx 1$ (see also Shankar et al. 2004 who introduce the redshift

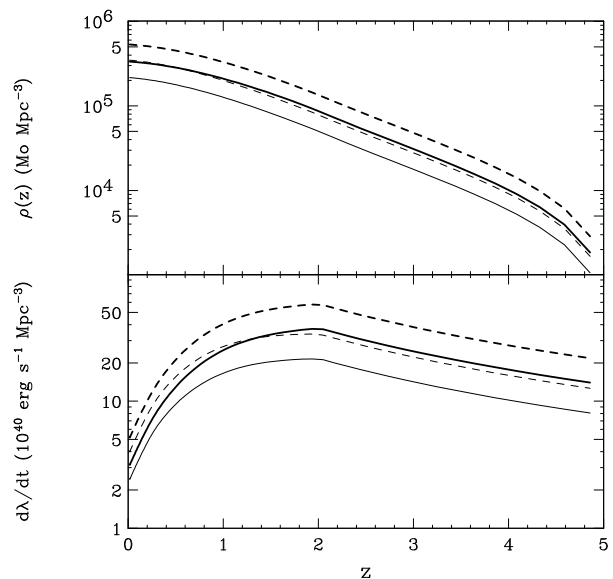


Figure 6. Upper panel: the growth curve of SMBHs traced by the U03 HXLF (total accreted mass density as a function of redshift). The mass-to-energy conversion factor $\epsilon = 0.1$ is assumed. Lower panel: evolution of the comoving bolometric luminosity density for $L_X > 10^{41.5} \text{ erg s}^{-1}$. The HXLF model is extrapolated to the range of $z > 3$. Solid line: only Compton-thin AGNs are considered. Dashed line: Compton-thick AGNs are included. The bolometric correction is made assuming $L_{\text{bol}} = 11.8L_B \propto L_X^{1/0.9}$ (case I: thick lines) and $L_{\text{bol}} = 30L_X$ (case II: thin lines).

dependence for η). Tamura et al. (2005) show that the accreted BHMF at $z \simeq 1$ with $\epsilon = 0.1$ and $\eta = 1$ is broadly consistent with the BHMF estimated from early-type galaxy luminosity functions at the redshift. These results suggest that the standard accretion with $\epsilon \simeq 0.1$ is the major process for the overall growth of SMBHs. However, considering the uncertainties particularly in the bolometric correction and Compton-thick AGN fraction, partial contribution from other accretion mode (such as radiatively inefficient accretion flow) is not entirely excluded, which could be important in the early stage of BH growth (e.g., Kawaguchi et al. 2004).

5. SUMMARY

Thanks to the continuous efforts for 43 years since the beginning of X-ray astronomy, we might be able to say that the origin of the XRB is almost solved at energies below $\simeq 6$ keV. Population synthesis models that takes into the HXLF and N_{H} function are now close to finalization with fine parameter tuning (see also Gilli 2005, this volume). However, when referring to “models”, one always has to keep in mind which are direct observational facts and which are assumptions. In fact, a significant portion of the XRB above 6 keV has not been resolved into discrete sources even in the currently deepest sur-

veys (Worsley et al., 2005), for which discussion still relies on extrapolation from observational results at lower energies. For instance, the shape of the N_{H} function including Compton-thick regimes ($\text{Log } N_{\text{H}} > 24$) has large uncertainties even in the local universe, and its evolution must be examined by much larger hard X-ray selected samples. The fraction of Compton-thick AGNs has direct impact on the accretion history of the universe. In population synthesis models that reproduce shape of the XRB spectrum, the assumed number of Compton-thick AGNs strongly couples with the mean amount of the reflection component, for which our knowledge is still limited. Obviously, higher sensitivity observations at energies above $\simeq 10$ keV are indispensable to address the remaining issues of the XRB.

ACKNOWLEDGEMENTS

I would like to thank my colleagues in this field for stimulating discussion. I am grateful to my collaborators for their help for this presentation, especially Masayuki Akiyama, Kouji Ohta, Takamitsu Miyaji, Yoshitaka Ishisaki, and Günther Hasinger.

REFERENCES

- Akiyama, M., et al. 2000, ApJ, 532, 700
- Akiyama, M., et al. 2003, ApJS, 148, 275
- Anderson, S. F. et al. 2003, AJ, 126, 2209.
- Awaki, H., Koyama, K., Inoue, H., & Halpern, J.P. 1991, PASJ, 43, 195
- Barcons, X., et al. 2002, A&A, 382, 522
- Barger, A.J., et al. 2003, AJ, 126, 632
- Barger, A.J., et al. 2005, AJ, 129, 578
- Beckmann, V, Gehrels, N., Shrader, C.R., Soldi, S. ApJ, 2005, in press
- Boyle, B.J., et al. 2000, MNRAS, 317, 1014, 2000
- Brandt, W.N., & Hasinger, G. 2005, ARA&A, 43, 827
- Chiappetti, L. et al. 2005, A&A, 439, 413
- Cowie, L.L., Songaila, A., Hu, E.M., Cohen, J.G. 1996, AJ, 112, 839
- Cowie, L.L., et al. 2003, ApJ, 584, L57
- Croom, S.M., et al. 2004, MNRAS, 349, 1397
- Della Ceca, R., et al. 2004, A&A, 428, 383
- Di Matteo, T., Croft, R.A.C., Springel, V., Hernquist, L. 2003, ApJ, 593, 56
- Elvis, M., et al. 1994, ApJS, 95, 1.
- Elvis, M., Risaliti, G., & Zamorani, G. 2002, ApJ, 565, L75.
- Fabian, A.C., & Iwasawa, K., 1999, MNRAS, 303, L34
- Fiore, F., et al. 1999, MNRAS, 306, L55
- Fiore, F., et al. 2003, A&A, 409, 79
- Granato, G.L., et al. 2004, ApJ, 600, 580
- Grossan, B., 1992, PhD thesis, MIT
- Harrison, F. A., Eckart, M. E., Mao, P. H., Helfand, D. J., & Stern, D. 2003, ApJ, 596, 944
- Hasinger, G., 2005, in “Growing black holes”, Merloni, A., Nayakshin S., Sunyaev R.A. (Eds.). Berlin: Springer, p. 418 (astro-ph/0412576)
- Hasinger, G., Miyaji, T., Schmidt, M. 2005, A&A, 441, 417
- Heavens, A., Panter, B., Jimenez, R., Dunlop, J. 2004, Nature, 428, 625
- Hopkins, P.F., et al. 2005, ApJ, in press (astro-ph/0506398)
- Ishisaki, Y., et al. 2001, PASJ, 53, 445
- Kawaguchi, T. et al. 2004, A&A, 420, L23
- Kim, D.-W., et al. 2004, ApJS, 150, 19
- Kodama, T. et al. 2004, MNRAS, 350, 1005
- Kushino, A., et al. 2002, PASJ, 54, 327
- La Franca, F., et al. 2005, ApJ, in press
- Lawrence, A. & Elvis, M. 1982, ApJ, 256, 410
- Maiolino, R., et al. 2001, A&A, 365, 28
- Marconi, A. et al. 2004, MNRAS, 351, 169
- Markwardt, C.B., et al. 2005, ApJL, in press
- Miyaji, T., Hasinger, G., & Schmidt, M. 2000, A&A, 353, 25
- Murray, S.S. et al. 2004, SPIE, 5488, 242
- Ohta, K., et al. 2003, ApJ, 598, 210
- Piccinotti, G., et al. 1982, ApJ, 253, 485
- Revnivtsev, M., Sazonov, S., Jahoda, K., & Gilfanov, M. 2004, A&A, 418, 927
- Risaliti, G., Maiolino, R., & Salvati, M. 1999, ApJ, 522, 157
- Salluci, P., Szuszkiewicz, E, Monaco, P., & Danese, L. 1999, MNRAS, 307 637
- Saxton, R.D., et al. 2005, SPIE 5898, 73
- Shankar, F., et al. 2004, MNRAS, 354, 1020

- Shinozaki, K., et al. 2005, AJ, submitted
- Silverman, J.D. et al. 2005, ApJ, 624, 630
- Soltan, A. 1982, MNRAS, 200, 115
- Steffen, A.T., et al. 2003, ApJ, 596, L23
- Steffen, A.T., et al. 2004, AJ, 128, 1483
- Szokoly, G.P., et al. 2004, ApJS, 155, 271
- Tamura, N., Ohta, K., Ueda, Y. 2005, MNRAS, in press
- Treister, E., et al. 2005, ApJ, 621, 104
- Treister, E., & Urry, C.M. 2005, ApJ, 630, 115
- Ueda, Y., et al. 1999, ApJ, 518, 656
- Ueda, Y., Ishisaki, Y., Takahashi, T., Makishima, K., & Ohashi, T. 2001, ApJS, 133, 1
- Ueda, Y., Akiyama, M., Ohta, K., & Miyaji, T. 2003, ApJ, 598, 886 (U03)
- Ueda, Y., Ishisaki, Y., Takahashi, T., Makishima, K., & Ohashi, T. 2005, ApJS, in press
- Worsley, M.A. et al. 2005, MNRAS, 357, 1281
- Yu, Q. & Tremaine, S. 2002, MNRAS, 335, 965

MINING *XMM-NEWTON* AND *CHANDRA* FIELDS FOR NORMAL GALAXIES

P. Tzanavaris¹, I. Georgantopoulos¹, A. Georgakakis², E. Koulouridis¹, A. Akylas¹, M. Plionis¹, I. Leonidaki¹, S. Basilakos¹, V. Chavmusyan³, and A. Mercado³

¹Institute of Astronomy and Astrophysics, National Observatory Athens, 152 36 Penteli, Greece

²Astrophysics Group, Imperial College London, Blackett Laboratory, Prince Consort Road, SW7 2AW, London, United Kingdom

³Instituto Nacional de Astrofísica, Óptica y Electrónica, Apartado Postal 51 y 216, 72000, Puebla, Pue., Mexico

ABSTRACT

We present results from our work on ‘normal’ X-ray selected galaxies (NGs). The $\log N - \log S$ relation for 46 NG candidates is fitted with a Euclidean power law (slope -1.46 ± 0.13 , cumulative number counts). For the largest set of NG candidates in the local Universe (68 galaxies) the best fit Schechter luminosity function (LF) parameters are $L^* = 41.02_{-0.12}^{+0.14}$, $\alpha = 1.76 \pm 0.10$. We discuss the discrepancy with a higher redshift LF at the bright end. We cross-correlated 1XMM and *Chandra*-XASSIST with the *2dFGRS* and found no luminous ($L_X > 10^{42}$) NGs but we found 8 NGs with $\log f_X/f_O > -2$. We complemented this sample with two samples from the literature and concluded that the $\log f_X/f_O < -2$ criterion for separating NGs from AGN mainly selects against massive elliptical NGs.

Key words: *XMM-Newton*; X-rays; galaxies.

1. INTRODUCTION

It is a well established fact that galaxies hosting an active galactic nucleus (AGN) give off copious amounts of X-ray emission. On the other hand, galaxies which are ‘normal’ (NGs), in the sense that they may not be AGN dominated, have only recently been studied in detail in the X-ray band. The likely source of X-ray emission in such systems is diffuse hot gas and/or X-ray binary stars. In the most massive early-type galaxies the X-ray emission is dominated by the hot interstellar medium with temperatures $kT \sim 1$ keV. A smaller fraction of the observed X-ray luminosity is due to low mass X-ray binaries associated with the older stellar population. In late-type galaxies, the X-ray emission originates in hot gas with temperature $kT \sim 1$ keV, which is heated by supernova remnants, as well as in a mixture of low and high-mass X-ray binaries (see Fabbiano, 1989, for a review). The diffuse hot gas contributes significantly in the soft X-ray

band (< 2 keV) while the X-ray binary systems are responsible for the bulk of the emission at harder energies (e.g. Stevens et al., 2003). The integrated X-ray emission of ‘normal’ galaxies is believed to be a good indicator of the star-formation activity in these systems (e.g. Gilfanov et al., 2004).

The X-ray luminosity of NGs is usually weak, $\lesssim 10^{42}$ erg s⁻¹, i.e. a few orders of magnitude below that of powerful AGN (Moran et al., 1999; Zezas et al., 1998). As a result, observed X-ray fluxes are faint and, until recently, only the very local systems (< 100 Mpc) were accessible to X-ray missions. With the new generation of X-ray missions, *Chandra* and *XMM-Newton*, the situation has changed dramatically. The *Chandra* Deep Fields North and South (CDF-N, CDF-S; Alexander et al., 2003; Giacconi et al., 2002) have reached fluxes $f(0.5 - 2.0$ keV) $\sim 10^{-17}$ erg cm⁻² s⁻¹, thus providing the first ever X-ray selected NG sample. Using the 2 Ms CDF-North, Hornschemeier et al. (2003) provided a sample of 43 NG candidates for which optical spectroscopic observations are available. These galaxies have X-ray-to-optical flux ratios $\log f_X/f_O < -2$, which these authors use as an empirical boundary, separating NGs from AGN. Norman et al. (2004) extended this study and identified over 100 NG candidates in the combined CDF-N and CDF-S, although optical spectroscopic data are available only for a fraction of these objects. However, these authors have identified NGs with $\log f_X/f_O > -2$. On the other hand, Georgakakis et al. (2003) and Georgakakis et al. (2004a) have identified NGs with $\log f_X/f_O \approx 2$. Here, we present some recent results and address possible selection caveats.

2. THE NEEDLES IN THE HAYSTACK SURVEY

The ‘Needles in the Haystack Survey’ (NHS) was a long-term project aiming to identify X-ray selected NGs in the local Universe. Within the framework of the NHS project (Georgakakis et al., 2004b; Georgantopou-

los et al., 2005), 70 *XMM-Newton* fields have been used in total. These cover an area of 11 square degrees and overlap with the Sloan Digital Sky Survey Data Release-2 (SDSS DR-2). The SDSS dataset is complete down to $g \approx 23$ (imaging) and $r \approx 17.7$ (spectroscopy). Using a search radius $r < 7''$ we identified optical counterparts for X-ray sources, from which NGs were selected according to the following selection criteria:

1. Galaxies should be resolved, i.e. have an extended optical light profile,
2. $\log f_X/f_O < -2$,
3. hardness ratios (HRs) *not* indicative of large amounts of absorption,
4. optical spectrum (where available) consistent with star-forming galaxies, based on diagnostic emission-line ratios and lack of broad emission lines.

The NG sample thus compiled comprises 28 galaxies. For only 5 of these are there no optical spectra. 16 of the galaxies have either a narrow emission-line optical spectrum or a spectral energy distribution (SED) consistent with a late-type spectrum. 12 of the galaxies have either exclusively absorption lines or a SED consistent with an early-type spectrum. The median redshift is 0.05.

A comparison of the luminosity-redshift relation for this sample with the NG samples from the CDF-N and S (Figure 1) shows that the NHS and CDF samples are complementary. After combination with 18 local galaxies from CDF-N and S, a local NG X-ray luminosity function was constructed.

3. NORMAL GALAXIES IN 1XMM

The above work has been extended in Georgakakis et al. (2005) by using the First *XMM-Newton* Serendipitous Source Catalogue (1XMM). The sample covers an area of ≈ 6 square degrees to a flux limit $\approx 10^{-14}$ erg cm $^{-2}$ s $^{-1}$. The galaxy selection criteria were as above with optical counterparts identified using the U.S. Naval Observatory Catalog (USNO), version A2.0. Follow-up spectroscopy was performed at the Guillermo Haro 2-m class telescope in Cananea, Mexico, and was complemented with the SDSS and the literature. A sample of 28 NGs was thus obtained, with optical spectra for 26 of these.

The inset plot in Figure 2 shows the ‘ $\log N - \log S$ ’ relation for our NG candidates. For the main plot, we combined the 1XMM and NHS samples into a new sample comprising a total of 46 NGs covering ≈ 15 square degrees. This can be fitted with a power law, obtaining a slope of -1.46 ± 0.13 (cumulative number counts, Euclidean), in excellent agreement with Hornschemeier et al. (2003) at faint fluxes and Tajer et al. (2005) at the very bright end.

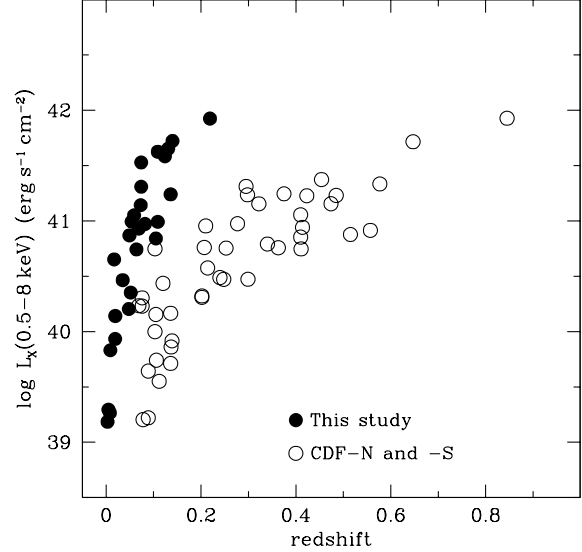


Figure 1. L_X (0.5-8.0 keV) against redshift, from Georgakopoulos et al. (2005). Filled circles are from the NHS NG candidate sample. Open circles are from the CDF samples. The two surveys cover complementary regions of $L_X - z$ space.

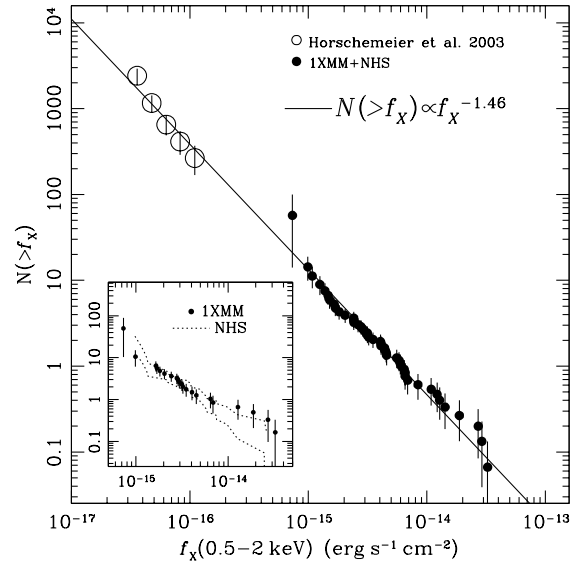


Figure 2. Cumulative normal galaxy counts in the 0.5-2.0 keV spectral band from Georgakakis et al. (2005). Filled circles are the combined sample of NG candidates from the NHS and 1XMM studies. Open circles are source counts from Hornschemeier et al. (2003). The continuous line is the best fit to the $\log N - \log S$ relation at bright fluxes from the combined NHS and 1XMM samples. The inset plot shows the $\log N - \log S$ for galaxies in the 1XMM study only, compared with counts from the NHS.

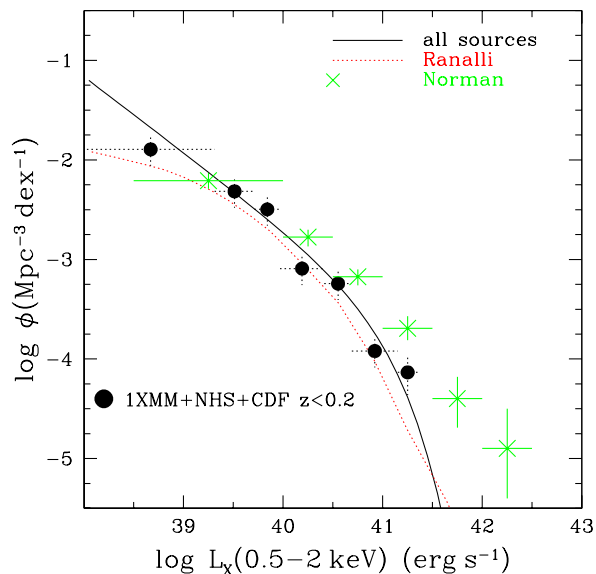


Figure 3. The 0.5 – 2.0 keV LF for the combined sample 1XMM, NHS and CDF of $z < 0.2$ NGs (adapted from Georgakakis et al., 2005). Filled circles are from the 68 NG sample described in the text. The solid line shows the maximum likelihood fit. The dashed line shows the IRAS LF (Ranalli et al., 2005) corrected to the X-ray band. The crosses are from Norman et al. (2004).

3.1. Luminosity Functions

We combined the 46 1XMM+NHS NGs with 22 local ($z < 0.2$) galaxies from the CDFs to obtain the largest sample of NGs in the local Universe, comprising 68 galaxies. As described in Georgantopoulos et al. (2005), we derived both the binned X-ray luminosity function (LF, Page & Carrera, 2000) and a parametric Maximum Likelihood fit (Tammann et al., 1979) adopting a Schechter (1976) form for the LF.

The 0.5 – 2.0 keV LF for the combined sample is shown in Figure 3. The best fit Schechter parameters are $L^* = 41.02^{+0.14}_{-0.12}$, $\alpha = 1.76 \pm 0.10$. Also shown are the IRAS LF of Ranalli et al. (2005) and the LF data points from the higher redshift sample of Norman et al. (2004). We note the good overall agreement with the IRAS LF. There is good agreement with the Norman et al. (2004) as well, except for the bright end. This may suggest (i) contamination of the Norman et al. (2004) sample by AGN, (ii) bias in our sample against luminous systems ($L_X \gtrsim 10^{42}$ erg s $^{-1}$) because of the $\log f_X/f_0 < -2$ cut or (iii) evolution of the NG LF.

In Figure 4 we are showing best fit LFs for all sources, as well as separately for emission line and absorption line NGs from our sample. The LFs are comparable.

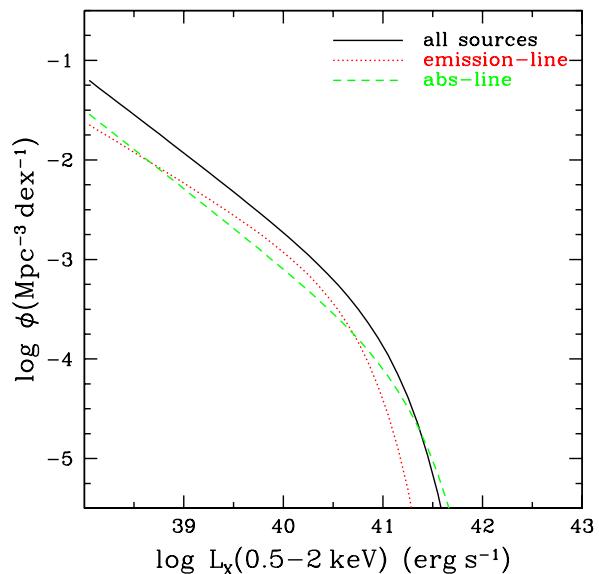


Figure 4. LFs for early and late type NGs. Solid line: best fit to all NGs. Dashed line: best fit to absorption line NGs. Dotted line: best fit to emission line NGs. LFs for the two categories are comparable. Adapted from Georgakakis et al. (2005).

4. NORMAL GALAXIES IN 2DFGRS

We have searched the Two Degree Field Galaxy Redshift Survey (2dFGRS) database for X-ray selected NGs (Tzanavaris et al., 2006). The $b_J = 19.45$ faint limit of this survey allows detection of galaxies up to $\log f_X/f_0 \sim 1$ for X-ray fluxes of a few $\times 10^{-14}$ erg cm $^{-2}$ s $^{-1}$.

We cross-correlated the 1XMM catalogue with the 2dFGRS and obtained 18 X-ray/optical pairs within a 6'' matching radius. We also cross-correlated the Chandra XASSIST catalogue with the 2dFGRS and obtained 20 X-ray/optical pairs within a 3'' matching radius. We used selection criteria similar to those described above to separate NGs from AGN. Our aim was to look for NGs which were (i) ‘luminous’ ($L_X > 10^{42}$ erg s $^{-1}$), and/or (ii) had $\log f_X/f_0 > -2$. We did not find any luminous NGs in our sample. However, we found 8 NGs (H II nuclei and absorption-line galaxies) with $\log f_X/f_0 > -2$.

We complemented our results with data from the literature. Specifically, we used the nearby star-forming galaxy sample compiled by Zezas (2001). This comprises 44 galaxies detected by ROSAT PSPC, spanning the luminosity range $L_X(0.1 - 2.4\text{keV}) \approx 4 \times 10^{37} - 3 \times 10^{41}$ erg s $^{-1}$. Galaxies in this sample have been classified on the basis of high quality nuclear spectra from Ho et al. (1997). Further, we used the nearby galaxy sample of Fabbiano et al. (1992). Galaxies in this sample have been observed with the Einstein observatory and comprise all morphological types. Galaxies flagged as AGN

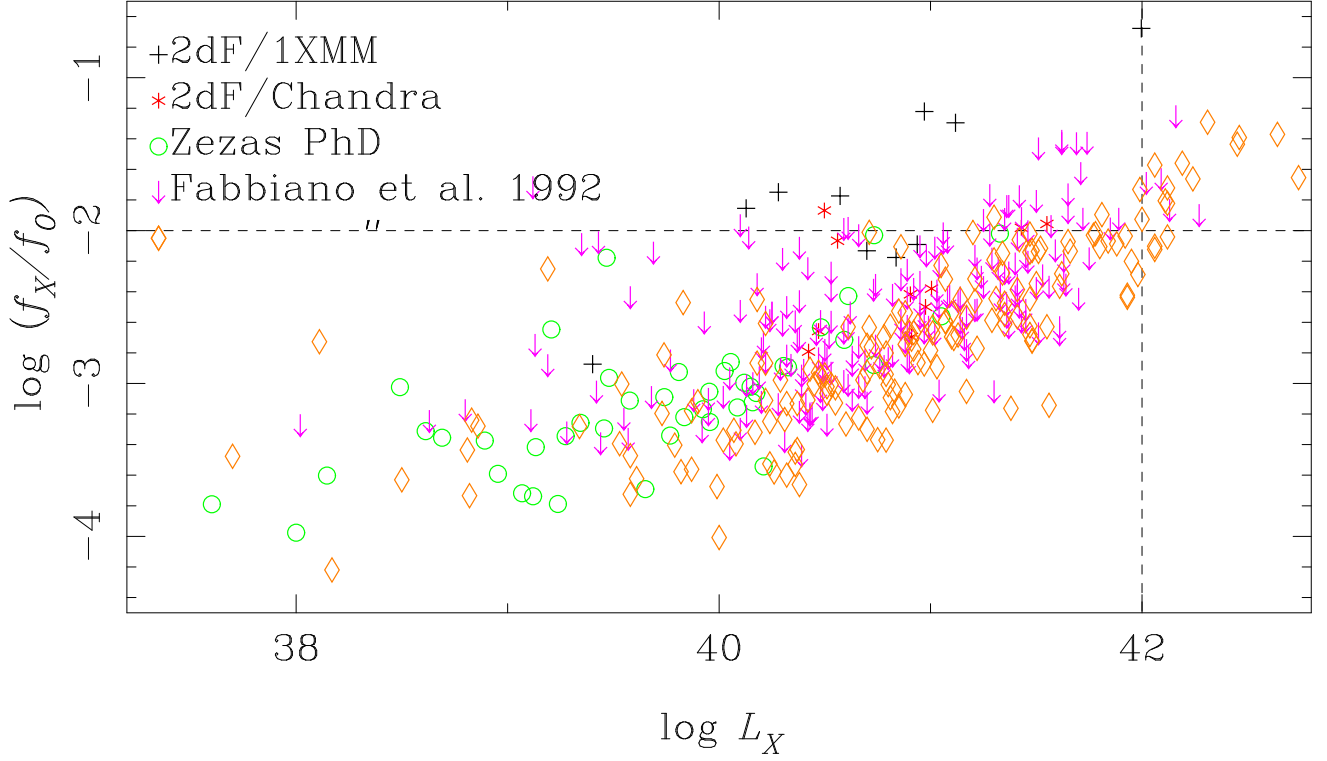


Figure 5. Plot of $\log f_X/f_0$ versus $\log L_X$. Plotted here are values calculated from our XMM-Newton and Chandra data, as well as from the literature (see legend in the plot). For all samples only galaxies which are classified as non-AGN are plotted. The two dashed lines demarcate the regions of $\log f_X/f_0$ – L_X space which may be inhabited mainly either by NGs ($\log L_X < 42$, $\log f_X/f_0 < -2$) or by AGN.

Table 1. NGs with $\log f_X/f_0 > -2$. Groups of rows separated by horizontal lines correspond to the sample indicated in the first column. 2dFGRS stands for the combined correlation samples 2dFGRS–XMM-Newton and 2dFGRS–Chandra. Each row corresponds to the NG type indicated in the second column. H II stands for H II nucleus, A for absorption-line spectrum, S for spiral, E for elliptical, Irr for irregular. Each of the last three columns gives the fraction of NGs with $\log f_X/f_0 > -2$ in the $\log L_X$ region indicated at the top of the column. Galaxies for which only upper limit information is available have not been taken into account. Empty entries indicate that no NGs of this type have been found.

Sample	NG type	$\log L_X < 42$	$41 < \log L_X < 42$	$\log L_X \geq 42$
2dFGRS	H II	4/26		
	H II?	1/26		
	A	2/26	2/10	1/12
Zezas (2001)	any	0	0	0
Fabbiano et al. (1992)	S/H II	1/194	1/75	1/40
	Irr	1/194	1/75	
	E	1/194	1/75	13/40

hosts in the original sample have been excluded. We have also carried out a further literature search to exclude more AGN from the final sample.

The combined samples are plotted in Figure 5. The observed correlation follows from the $L_X \sim L_B^{1.8}$ (Fabbiano et al., 1992). Results for galaxies with $\log f_X/f_O > -2$ are tabulated in Table 1. Note that in the Zezas (2001) sample there are no luminous or $\log f_X/f_O > -2$ galaxies, unlike the Fabbiano et al. (1992) sample. The latter sample clearly suggests that the $\log f_X/f_O < -2$ criterion selects against massive elliptical NGs. This sample and our *2dFGRS* sample also suggest some selection against star-forming NGs. However, the *2dFGRS* results are more tentative, because they are largely based on diagnostic emission-line ratios, without previous stellar template subtraction. Reliable stellar-template subtraction is not possible for *2dFGRS* fibre spectra, so the question remains open until better spectra are available.

5. FUTURE PROSPECTS

We are further expanding the 68-galaxy sample described above by using *Chandra*-SDSS fields, in order to reach fainter fluxes and luminosities. We are also in the process of obtaining higher-quality spectra for further assessing the effect of the $\log f_X/f_O < -2$ criterion on galaxy selection.

REFERENCES

- Alexander, D. M., Bauer, F. E., Brandt, W. N., et al. 2003, *AJ*, 126, 539
- Fabbiano, G. 1989, *ARA&A*, 27, 87
- Fabbiano, G., Kim, D.-W., & Trinchieri, G. 1992, *ApJS*, 80, 531
- Georgakakis, A., Georgantopoulos, I., Stewart, G. C., Shanks, T., & Boyle, B. J. 2003, *MNRAS*, 344, 161
- Georgakakis, A., Georgantopoulos, I., Vallbé, M., et al. 2004a, *MNRAS*, 349, 135
- Georgakakis, A. E., Chamvusyan, V., Plionis, M., et al. 2005, submitted, *MNRAS*
- Georgakakis, A. E., Georgantopoulos, I., Basilakos, S., Plionis, M., & Kolokotronis, V. 2004b, *MNRAS*, 354, 123
- Georgantopoulos, I., Georgakakis, A., & Koulouridis, E. 2005, *MNRAS*, 360, 782
- Giacconi, R., Zirm, A., Wang, J., et al. 2002, *ApJS*, 139, 369
- Gilfanov, M., Grimm, H.-J., & Sunyaev, R. 2004, *MNRAS*, 347, L57

- Ho, L. C., Filippenko, A. V., & Sargent, W. L. W. 1997, *ApJS*, 112, 315
- Hornschemeier, A. E., Bauer, F. E., Alexander, D. M., et al. 2003, *AJ*, 126, 575
- Moran, E. C., Lehnert, M. D., & Helfand, D. J. 1999, *ApJ*, 526, 649
- Norman, C., Ptak, A., Hornschemeier, A., et al. 2004, *ApJ*, 607, 721
- Page, M. J. & Carrera, F. J. 2000, *MNRAS*, 311, 433
- Ranalli, P., Comastri, A., & Setti, G. 2005, *A&A*, 440, 23
- Schechter, P. 1976, *ApJ*, 203, 297
- Stevens, I. R., Read, A. M., & Bravo-Guerrero, J. 2003, *MNRAS*, 343, L47
- Tajer, M., Trinchieri, G., Wolter, A., et al. 2005, *A&A*, 435, 799
- Tammann, G. A., Yahil, A., & Sandage, A. 1979, *ApJ*, 234, 775
- Tzanavaris, P., Georgantopoulos, I., & Georgakakis, A. 2006, in preparation, *A&A*
- Zezas, A. L. 2001, PhD thesis, Univ. of Leicester
- Zezas, A. L., Georgantopoulos, I., & Ward, M. J. 1998, *MNRAS*, 301, 915

RESULTS FROM THE FIRST *INTEGRAL* AGN CATALOGUE

Volker Beckmann^{1,2}, Simona Soldi^{3,4}, Chris R. Shrader¹ and Neil Gehrels¹

¹NASA Goddard Space Flight Center, Exploration of the Universe Division, Code 661, Greenbelt, MD 20771, USA

²Joint Center for Astrophysics, Department of Physics, University of Maryland, Baltimore County, MD 21250, USA

³*INTEGRAL* Science Data Centre, 16 chemin d'Écogia, 1290 Versoix, Switzerland

⁴Observatoire de Genève, 51 chemin des Maillettes, 1290 Sauverny, Switzerland

ABSTRACT

We present results based on the first *INTEGRAL* AGN catalogue. The catalogue includes 42 AGN, of which 10 are Seyfert 1, 17 are Seyfert 2, and 9 are intermediate Seyfert 1.5. The fraction of blazars is rather small with 5 detected objects, and only one galaxy cluster and no starburst galaxies have been detected so far. The sample consists of bright ($f_X > 5 \times 10^{-12} \text{ erg cm}^{-2} \text{ s}^{-1}$), low luminosity ($\bar{L}_X = 2 \times 10^{43} \text{ erg s}^{-1}$), local ($\bar{z} = 0.020$) AGN. Although the sample is not flux limited, we find a ratio of obscured to unobscured AGN of 1.5 – 2.0, consistent with luminosity dependent unified models for AGN. Only four Compton-thick AGN are found in the sample. This implies that the missing Compton-thick AGN needed to explain the cosmic hard X-ray background would have to have lower fluxes than discovered by *INTEGRAL* so far.

Key words: galaxies: active, catalogues, gamma rays: observations, X-rays: galaxies, galaxies: Seyfert.

1. INTRODUCTION

The X-ray sky as seen by satellite observations over the past 40 years, shows a substantially different picture than for example the optical band. While the visual night sky is dominated by main sequence stars, Galactic binary systems and super nova remnants form the brightest objects X-rays. Common to both regimes is the dominance of active galactic nuclei (AGN) toward lower fluxes. In the X-ray range itself, one observes a slightly different population of AGN at soft and at hard X-rays. Below 5 keV the X-ray sky is dominated by AGN of the Seyfert 1 type; above 5 keV the absorbed Seyfert 2 objects appear to become more numerous. These type 2 AGN are also believed to be the main contributors to the cosmic X-ray background above 5 keV (Setti & Woltjer 1989; Comastri et al. 1995; Gilli et al. 2001), although only $\sim 50\%$

of the XRB above 8 keV can be resolved (Worsley et al. 2005).

The hard X-ray energy range is not currently accessible to X-ray telescopes using grazing incidence mirror systems. Instead detectors without spatial resolution like the PDS on *BeppoSAX* and OSSE on *CGRO* have been applied. A synopsis of these previous results is as follows: the 2 – 10 keV Seyfert 1 continua are approximated by a $\Gamma \simeq 1.9$ powerlaw form (Zdziarski et al. 1995). A flattening above ~ 10 keV has been noted, and is commonly attributed to Compton reflection (George & Fabian 1991). There is a great deal of additional detail in this spectral domain - “warm” absorption, multiple-velocity component outflows, and relativistic line broadening - which are beyond the scope of this paper. The Seyfert 2 objects are more poorly categorized here, but the general belief is that they are intrinsically equivalent to the Seyfert 1s, but viewed through much larger absorption columns.

Above 20 keV the empirical picture is less clear. The $\sim 20 - 200$ keV continuum shape of both Seyfert types is consistent with a thermal Comptonization spectral form, although in all but a few cases the data are not sufficiently constraining to rule out a pure powerlaw form. Nonetheless, the non-thermal scenarios with pure powerlaw continua extending to \sim MeV energies reported in the pre-*CGRO* era are no longer widely believed, and are likely a result of background systematics. However, a detailed picture of the Comptonizing plasma - its spatial, dynamical, and thermo-dynamic structure - is not known. Among the critical determinations which *INTEGRAL* or future hard X-ray instruments will hopefully provide are the plasma temperature and optical depth (or Compton “Y” parameter) for a large sample of objects.

The other major class of gamma-ray emitting AGN - the blazars (FSRQs and BL Lac objects) are even more poorly constrained in the *INTEGRAL* spectral domain (for early *INTEGRAL* results see for example Pian et al. 2005).

Critical to each of these issues is the need to obtain improved continuum measurements over the hard X-ray to soft gamma-ray range for as large a sample of objects as possible. *INTEGRAL*, since its launch in October 2002, offers unprecedented > 20 keV collecting area and state of the art detector electronics and background rejection capabilities. Thus it offers hope of substantial gains in our knowledge of the AGN phenomenon and in particular of the cosmic hard X-ray background.

The first *INTEGRAL* AGN catalogue offers the possibility to address these questions and to compare the results with previous missions.

2. THE *INTEGRAL* AGN SAMPLE

Our *INTEGRAL* AGN sample¹ consists of 42 extragalactic objects, detected in the 20 – 40 keV energy band with the imager IBIS/ISGRI. Spectra have been extracted from IBIS/ISGRI, the spectrometer SPI, and the X-ray monitor JEM-X in order to cover the energy range from 3 – 500 keV. The list of sources with their redshift, the optical counterpart type, the flux in the 20 – 40 keV band as measured by ISGRI, the luminosity in the 20 – 100 keV band, and the intrinsic absorption as measured at soft X-rays is given in Table 1. Details on the analysis and on individual spectra can be found in Beckmann et al. (2006). The distribution of sources in the sky is shown in Figure 2.

The Seyfert type AGN found in the sample are preferentially low redshift objects. Figure 1 shows the distribution of redshifts in the sample. The blazars all show higher redshifts ($0.15 < z < 2.51$) and are not included in the histogram. The one object on the right is PG 1416–129 ($z = 0.1293$) and is an anomalous radio quiet quasar with similar spectroscopic properties as radio-loud sources (Sulentic et al. 2000).

In order to investigate the AGN subtypes, we have derived averaged spectra of the Seyfert 1 and 2 types, as well as for the intermediate Seyferts and the blazars. The average Seyfert 1 spectrum was constructed using the weighted mean of 10 ISGRI spectra, the Seyfert 2 composite spectrum includes 15 sources, and 8 objects form the intermediate Seyfert 1.5 group. The two brightest sources, Cen A and NGC 4151, have been excluded from the analysis as their high signal-to-noise ratio would dominate the averaged spectra. The average spectra have been constructed by computing the weighted mean of all fit results on the individual sources. In order to do so, all spectra had been fit by an absorbed single powerlaw model. When computing the weighted average of the various sub-classes, the Seyfert 2 objects show flatter hard X-ray spectra ($\Gamma = 1.95 \pm 0.01$) than the Seyfert 1.5 ($\Gamma = 2.10 \pm 0.02$), and Seyfert 1 appear to have the steepest spectra ($\Gamma = 2.11 \pm 0.05$) together with the blazars ($\Gamma = 2.07 \pm 0.10$).

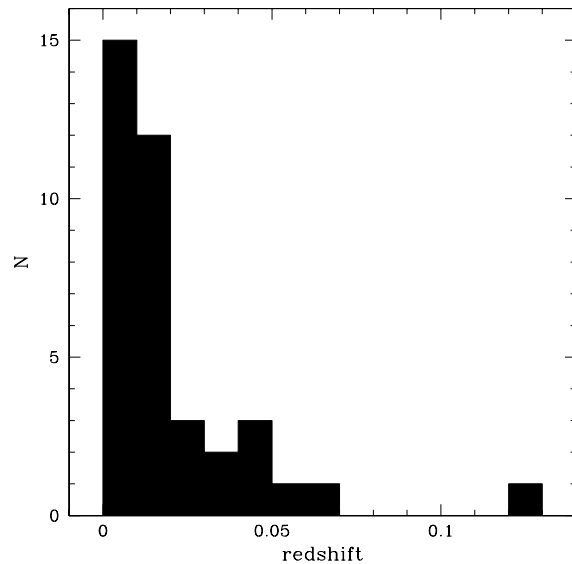


Figure 1. Redshift distribution of the AGN detected by *INTEGRAL*. Blazars are not shown. The average redshift is $\bar{z} = 0.020$. The object on the right is the quasar PG 1416–129.

The Seyfert type classification of the objects is based on optical observations. An approach to classifying sources according to their properties in the X-rays can be done by separating the sources with high intrinsic absorption ($N_H > 10^{22} \text{ cm}^{-2}$) from those objects which do not show significant absorption. The distribution of absorption at soft X-rays for the AGN sample is shown in Figure 3. The black part of the histogram represents the Seyfert 2 AGN (including the Seyfert 1.8 and Seyfert 1.9 subtypes). It has to be pointed out that not all objects which show high intrinsic absorption in the X-rays are classified as Seyfert 2 galaxies in the optical, and the same applies for the other AGN subtypes. Nevertheless a similar trend in the spectral slopes can be seen: the 21 absorbed AGN show a flatter hard X-ray spectrum ($\Gamma = 1.98 \pm 0.01$) than the 13 unabsorbed sources ($\Gamma = 2.08 \pm 0.02$). The blazars have again been excluded from these samples.

Among the Seyfert 2 galaxies we find 4 objects with low absorption ($N_H < 10^{23} \text{ cm}^{-2}$), 7 with intermediate absorption ($N_H = 10^{23} - 10^{24} \text{ cm}^{-2}$), and four Compton thick AGN ($N_H > 10^{24} \text{ cm}^{-2}$).

Although the *INTEGRAL* AGN sample discussed here is not a complete flux limited one, the number counts give a first impression regarding the flux distribution within the sample (Fig. 4). Excluding the two brightest objects (Cen A and NGC 4151) and the objects with $f_X < 2 \times 10^{-11} \text{ erg cm}^{-2} \text{ s}^{-1}$ (where the number counts shows a turnover), the number counts relation shows a gradient of 1.4 ± 0.1 , and is consistent with the value of 1.5 expected for Euclidian geometry and no evolution in the local universe.

¹<http://heasarcdev.gsfc.nasa.gov/docs/integral/spi/pages/agn.html>

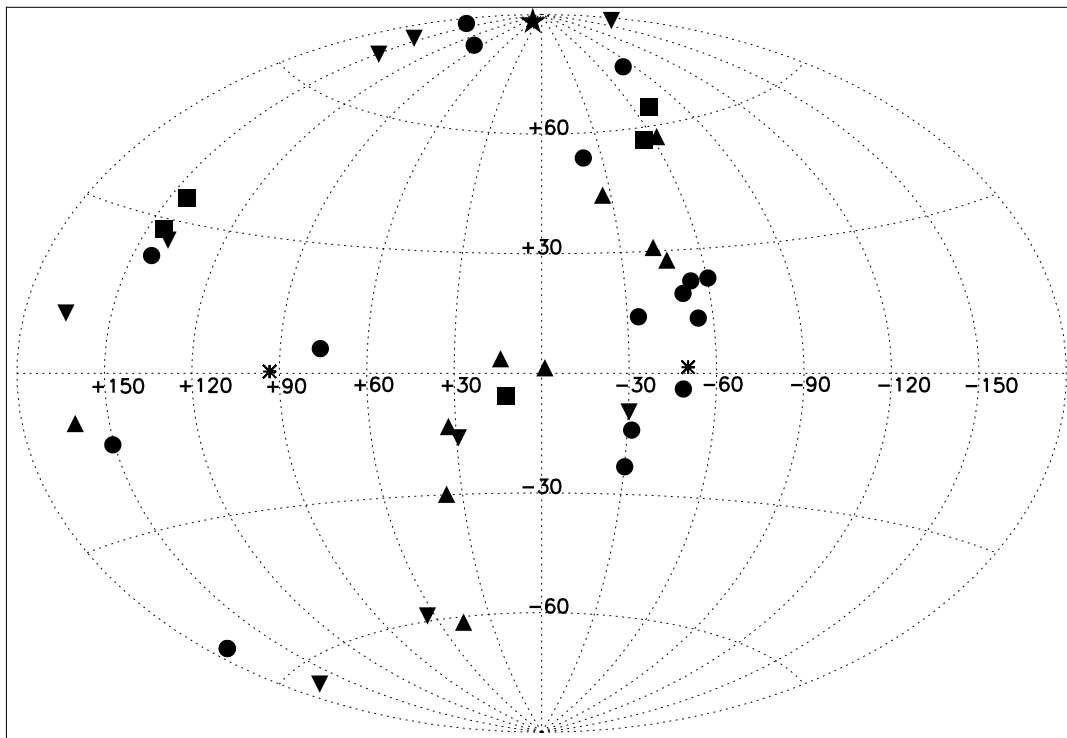


Figure 2. The distribution of INTEGRAL AGN in the sky in Galactic coordinates. Seyfert 1 are marked with up-triangles, Seyfert 1.5 with down-triangles, Seyfert 2 with circles, blazars with squares, optically unidentified with asterisks, and the Coma Cluster is represented by a star.

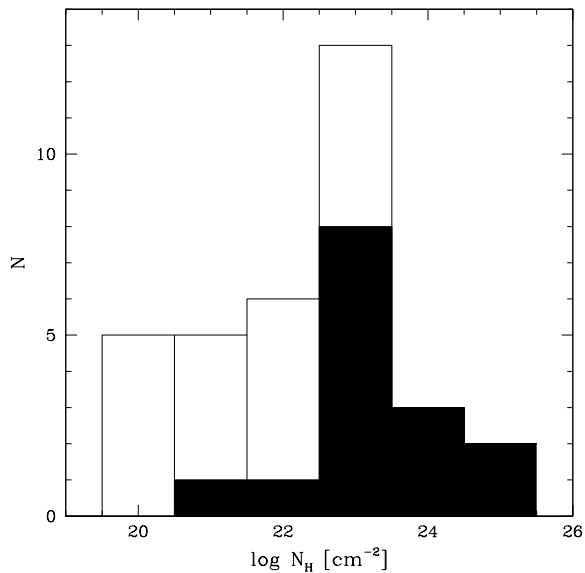


Figure 3. Distribution of intrinsic absorption, as measured in the soft X-rays. The Seyfert 2 objects (including the Seyfert 1.8 and 1.9 subtypes) are shown in black.

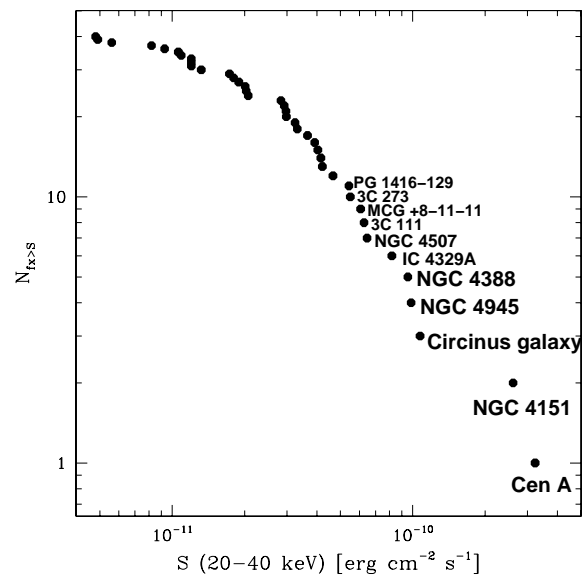


Figure 4. Number counts of the INTEGRAL AGN sample. The brightest objects have been labelled.

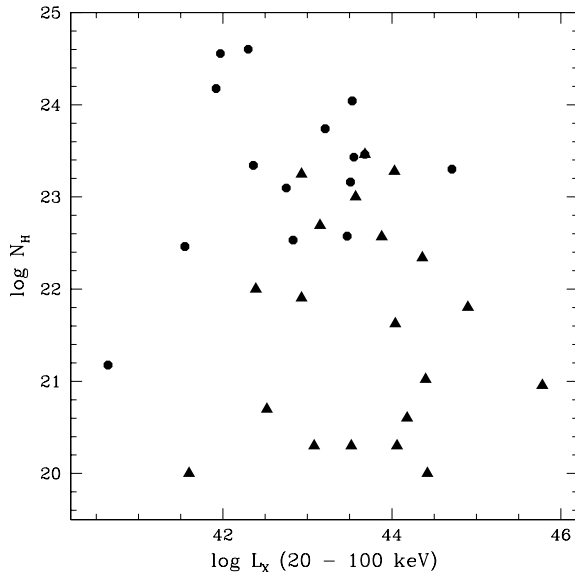


Figure 5. Intrinsic absorption, as measured at soft X-rays, versus the luminosity in the 20 – 100 keV band. Circles represent Seyfert 2 type AGN (including Sy 1.8 and Sy 1.9), triangles other Seyfert types.

Figure 5 shows the intrinsic absorption of the objects, as measured in the soft X-rays, versus the luminosity in the 20 – 100 keV energy band as measured by *INTEGRAL*. There is no discernible correlation between those values. The optically classified Seyfert 2 objects naturally populate the area with higher intrinsic absorption.

3. DISCUSSION

The typical *INTEGRAL* spectrum can be described by a simple powerlaw model with average photon indices ranging from $\Gamma = 2.0$ for obscured AGN to $\Gamma = 2.1$ for unabsorbed sources. The simple model does not give reasonable results in high signal-to-noise cases, where an appropriate fit requires additional features such as a cut-off and a reflection component (Soldi et al. 2005, Beckmann et al. 2005). The results presented here show slightly steeper spectra than previous investigations of AGN in comparable energy ranges. The same trend is seen in the comparison of Crab observations, where the *INTEGRAL*/ISGRI spectra also appear to be slightly steeper than in previous observations, and in comparison of *RXTE* and *INTEGRAL*/ISGRI spectra of Cen A (Rothschild et al. 2006). This trend might be based on improper calibration and/or background subtraction.

The average properties, like spectral slope, redshift, luminosity, are rather similar compared to previous studies (e.g. Zdziarski et al. 1995, Gondek et al. 1996).

Comparing the ratio X of obscured ($N_H > 10^{22} \text{ cm}^{-2}$) to unabsorbed AGN we find in the *INTEGRAL* data that

$X = 1.7 \pm 0.4$. The ratios change slightly when taking into account only those objects which belong to the complete sample with an ISGRI significance of 7σ or higher (Beckmann et al. 2006). This sub-sample includes 32 AGN, with 18 obscured and 10 unabsorbed objects (absorption information is missing for the remaining four objects). Using only the complete sample gives a similar ratio of $X = 1.8 \pm 0.5$. Splitting this result up into objects near the Galactic plane ($|b| < 20^\circ$) and off the plane shows for all objects a ratio of $X = 3.3 \pm 1.1$ and $X = 1.1 \pm 0.5$, respectively. This trend shows that the harder spectra of those objects, where the absorption in the line of sight through the Galaxy is low compared to the intrinsic absorption, are more likely to shine through the Galactic plane.

Risaliti et al. (1999) studied a large sample of Seyfert 2 galaxies focusing especially on the intrinsic absorption measured at soft X-rays. They also find a fraction of 75% of Seyfert 2 with an intrinsic absorption $N_H > 10^{23} \text{ cm}^{-2}$, but a 50% fraction of Compton-thick objects with $N_H > 10^{24} \text{ cm}^{-2}$, where the *INTEGRAL* sample only finds 4 objects (27 %).

Optical studies in the local universe find evidence that type 2 AGN are about a factor of four more numerous than type 1 AGN (Setti & Woltjer 1989; Comastri et al. 1995). In X-rays the situation is similar, although not all Seyfert 1 objects show low intrinsic absorption and vice versa (see Fig. 5). Recent studies have shown that the fraction of absorbed sources depends both on luminosity and redshift in a way that the fraction of type 2 AGN increases towards higher redshifts and lower luminosity (e.g. Gilli et al. 2001; Ueda et al. 2003; La Franca et al. 2005). Ueda et al. (2003) studied 247 AGNs in the 2 – 10 keV band with luminosities in the range $L_X = 10^{41.5} - 10^{46.5} \text{ erg s}^{-1}$, similar to the luminosity range of the *INTEGRAL* AGN but extending to higher redshifts ($z = 0 - 3$) and to fainter fluxes ($f_X = 10^{-10} - 3.8 \times 10^{-15} \text{ erg cm}^{-2} \text{ s}^{-1}$). They find that the number of AGN decreases with the intrinsic X-ray luminosity of the AGN and therefore favour a luminosity dependent density evolution (LDDE) to explain the luminosity function in the 2 – 10 keV band. La Franca et al. (2005) used an even larger sample and confirmed the necessity of a LDDE model, where low luminosity AGN peak at $z \sim 0.7$, while high luminosity AGN peak at $z \sim 2.0$. In addition, they find evidence that the fraction of absorbed ($N_H > 10^{22} \text{ cm}^{-2}$) AGN decreases with the intrinsic luminosity in the 2 – 10 keV energy range. Consistent with our study, La Franca et al. also find a ratio of $X = 2.1$ at $L_X = 10^{42.5} \text{ erg s}^{-1}$.

All these results based on the 2 – 10 keV band are consistent with the findings of the *INTEGRAL* AGN sample at higher energies (20 – 40 keV). It is surprising though that different from the findings of Risaliti et al. (1999) we do not detect a large fraction of Compton-thick AGN. These AGN, if existing, could explain the peak in the hard X-ray background around 30 keV (e.g. Maiolino et al. 2003). In view of recent results this lack of Compton-thick objects is explainable by the type of

AGN detected so far by *INTEGRAL*. All objects are local AGN, with a mean redshift of $\bar{z} = 0.020$ (Fig. 1). The objects are bright ($f_{20-40 \text{ keV}} > 5 \times 10^{-12}$; Fig. 4), but have low luminosities ($L_X = 2 \times 10^{43} \text{ erg s}^{-1}$). This still leaves room in the parameter space of AGN to locate Compton-thick AGN. Those objects could have lower fluxes and therefore even lower luminosities in the local universe than the objects studied by *INTEGRAL*. This possibility is supported by the unified model for AGN as described by Treister & Urry (2005). They predict a strong correlation of the fraction of broad line AGN with luminosity, and expect up to a factor of 10 more absorbed than un-absorbed AGN at very low luminosities ($L_X \simeq 10^{42} \text{ erg s}^{-1}$). This trend can be seen also in the *INTEGRAL* AGN sample. When considering only the 14 objects with $L_{20-100 \text{ keV}} < 10^{43} \text{ erg s}^{-1}$ the ratio of obscured to unobscured objects increases to $X = 2.5$.

Studying the population of sources at lower limiting fluxes should also reveal further highly absorbed sources at high redshifts, because these have been missed so far and with increasing redshift an increase of absorbed AGN fraction is expected (La Franca et al. 2005).

The energy range in the 15 – 200 keV is now also accessible through the BAT instrument aboard *Swift* (Gehrels et al. 2005). A study by Markwardt et al. (2005) used data from the first three months of the *Swift* mission for studying the extragalactic sky and reached a flux limit of $f_{(14-195 \text{ keV})} \simeq 10^{-11} \text{ erg cm}^{-2} \text{ s}^{-1}$. The source population is similar to the *INTEGRAL* one, with an average redshift of $\bar{z} = 0.012$, and a ratio of $X = 2$ between obscured and unobscured AGN, fully consistent with *INTEGRAL*. Although the *Swift*/BAT survey covers different areas of the sky, the energy band is similar to the *INTEGRAL*/ISGRI range and the type of AGN detectable should be the same. Within their sample of 44 AGN they detect 5 Compton-thick AGN, the same ratio as in the *INTEGRAL* sample. The only difference appears in the relation between luminosity and absorption. While in the *INTEGRAL* sample no correlation is detectable (Fig. 5), Markwardt et al. find in their sample evidence for an anti-correlation of luminosity and absorption.

4. CONCLUSIONS

The *INTEGRAL* AGN sample opens the window to the hard X-ray sky above 20 keV for population studies. With the 42 extragalactic objects discussed here, a fraction of about 60% shows absorption above $N_H = 10^{22} \text{ cm}^{-2}$, but only four objects are actually Compton-thick ($N_H > 10^{24} \text{ cm}^{-2}$). This shows that the source population above 20 keV, at least at the high flux end, is very similar to the one observed in the 2 – 10 keV energy region. The results are consistent with observations by the *Swift*/BAT instrument, although we cannot confirm a correlation of X-ray luminosity with intrinsic absorption. Further investigations are necessary and with the ongoing *INTEGRAL* and *Swift* mission it will be revealed in the near future, if there is a significant Compton-thick AGN pop-

ulation to explain the peak in the extragalactic X-ray background around 30 keV. These objects would have to have lower fluxes than the objects studied here (i.e. $f_X < 10^{-11} \text{ erg cm}^{-2} \text{ s}^{-1}$) and might therefore be low-redshift, low-luminosity ($L_X \lesssim 10^{42} \text{ erg s}^{-1}$) Seyfert galaxies, or higher redshift ($z \gg 0.05$) objects.

REFERENCES

- Beckmann V., Shrader C. R., Gehrels N., et al. 2005, ApJ in press, astro-ph/0508327
- Beckmann V., Gehrels N., Shrader C. R., & Soldi S. 2006, ApJ accepted, astro-ph/0510530
- Comastri A., Setti G., Zamorani G., Hasinger G. 1995, A&A, 296, 1
- Gehrels N., Chincarini G., Giommi P., 2004, ApJ, 611, 1005
- George I. M., & Fabian A. C. 1991, MNRAS, 249, 352
- Gilli R., Salvati M., Hasinger G., 2001, A&A, 366, 407
- Gondek D., Zdziarski A. A., Johnson W. N., et al. 1996, MNRAS, 282, 646
- La Franca F., Fiore F., Comastri A., et al. 2005, ApJ in press, astro-ph/0509081
- Maiolino R., Comastri A., Gilli R., et al. 2003, MNRAS, 344, L59
- Markwardt C. B., Tueller J., Skinner G. K., et al. 2005, ApJL in press, astro-ph/0509860
- Pian E., Foschini L., Beckmann V., et al. 2005, A&A, 429, 427
- Rothschild R. E., Wilms J., Tomsick J., et al. 2006, ApJ submitted
- Setti G., & Woltjer L. 1989, A&A, 224, L21
- Soldi S., Beckmann V., Bassani L., et al. 2005, A&A accepted, astro-ph/0509123
- Sulentic J. W., Marziani P., Zwitter T., et al. 2000, ApJ, 545, L15
- Treister E., Urry C. M., 2005, ApJ in press, astro-ph/0505300
- Ueda Y., Akiyama M., Ohta K., Miyaji T. 2003, ApJ, 598, 886
- Worsley M. A., Fabian A. C., Bauer F. E., et al. 2005, MNRAS, 357, 1281
- Zdziarski A. A., Johnson W. N., Done C., et al. 1995, ApJ, 438, L63

Table 1. The INTEGRAL AGN sample

Name	z	type	$f_{(20-40\text{ keV})}$ [$10^{-11}\text{ erg cm}^{-2}\text{ s}^{-1}$]	$\log L_{(20-100\text{ keV})}$ [erg s^{-1}]	N_H [10^{22} cm^{-2}]
NGC 788	0.0136	Sy 1/2	2.98 ± 0.24	43.52	< 0.02
NGC 1068	0.0038	Sy 2	0.93 ± 0.27	41.92	> 150
NGC 1275	0.0176	Sy 2	1.89 ± 0.21	43.47	3.75
3C 111	0.0485	Sy 1	6.27 ± 0.57	44.90	0.634
MCG +8-11-11	0.0205	Sy 1.5	6.07 ± 0.97	44.06	< 0.02
MRK 3	0.0135	Sy 2	3.65 ± 0.39	43.53	110
MRK 6	0.0188	Sy 1.5	2.01 ± 0.20	43.57	10
NGC 4051	0.0023	Sy 1.5	1.80 ± 0.20	41.60	< 0.01
NGC 4151	0.0033	Sy 1.5	26.13 ± 0.16	43.15	4.9
NGC 4253	0.0129	Sy 1.5	0.93 ± 0.22	42.93	0.8
NGC 4388	0.0084	Sy 2	9.54 ± 0.25	43.55	27
NGC 4395	0.0011	Sy 1.8	0.56 ± 0.22	40.64	0.15
NGC 4507	0.0118	Sy 2	6.46 ± 0.36	43.68	29
NGC 4593	0.0090	Sy 1	3.31 ± 0.16	43.08	0.02
Coma Cluster	0.0231	GClstr.	1.09 ± 0.12	43.40	< 0.01
NGC 4945	0.0019	Sy 2	9.85 ± 0.23	42.30	400
ESO 323-G077	0.0150	Sy 2	1.20 ± 0.19	43.21	55
NGC 5033	0.0029	Sy 1.9	1.06 ± 0.24	41.55	2.9
Cen A	0.0018	Sy 2	32.28 ± 0.17	42.75	12.5
MCG-06-30-015	0.0077	Sy 1	2.98 ± 0.19	42.93	17.7
4U 1344-60	0.043	?	2.83 ± 0.15	44.36	2.19
IC 4329A	0.0161	Sy 1.2	8.19 ± 0.17	44.04	0.42
Circinus gal.	0.0014	Sy 2	10.73 ± 0.18	41.97	360
NGC 5506	0.0062	Sy 1.9	4.21 ± 0.33	42.83	3.4
PG 1416-129	0.1293	Sy 1	5.43 ± 0.64	45.78	0.09
IC 4518	0.0157	Sy 2	0.49 ± 0.32	42.92	?
NGC 6221	0.0050	Sy 1/2	1.32 ± 0.20	42.39	1
NGC 6300	0.0037	Sy 2	3.91 ± 0.37	42.36	22
GRS 1734-292	0.0214	Sy 1	4.03 ± 0.09	43.88	3.7
IGR J18027-1455	0.0350	Sy 1	2.03 ± 0.16	44.03	19.0
ESO 103-G35	0.0133	Sy 2	2.97 ± 0.66	43.51	13 - 16
1H 1934-063	0.0106	Sy 1	0.48 ± 0.25	42.51	?
NGC 6814	0.0052	Sy 1.5	2.92 ± 0.23	42.52	< 0.05
Cygnus A	0.0561	Sy 2	3.24 ± 0.14	44.71	20
MRK 509	0.0344	Sy 1	4.66 ± 0.47	44.42	< 0.01
IGR J21247+5058	0.020	radio gal.?	4.15 ± 0.27	44.00	?
MR 2251-178	0.0634	Sy 1	1.20 ± 0.17	44.40	0.02 - 0.19
MCG -02-58-022	0.0469	Sy 1.5	1.20 ± 0.28	44.18	< 0.01 - 0.08
S5 0716+714	0.3 ^a	BL Lac	0.14 ± 0.11	45.21 ^a	< 0.01
S5 0836+710	2.172	FSRQ	1.73 ± 0.28	47.87	0.11
3C 273	0.1583	Blazar	5.50 ± 0.15	45.92	0.5
3C 279	0.5362	Blazar	0.82 ± 0.24	46.37	0.02 - 0.13
PKS 1830-211	2.507	Blazar	2.07 ± 0.14	48.09	< 0.01 - 0.7

^a tentative redshift

THE BRIGHT SIDE OF THE HARD X-RAY SKY: THE XMM-NEWTON BRIGHT SURVEY

R. Della Ceca^{1,3}, A. Caccianiga^{1,3}, P. Severgnini^{1,3}, T. Maccacaro^{1,3}, F. Cocchia^{1,3}, and V. Braito^{2,3}

¹INAF-Osservatorio Astronomico di Brera, via Brera 28, I-20121 Milan, Italy

²Johns Hopkins University, 3400 N. Charles Street, Baltimore, MD 21218, USA

³on behalf of the XMM-Newton SSC collaboration

ABSTRACT

We discuss here the main goals and some interesting results of the “XMM-Newton Bright Serendipitous Survey”, a research program conducted by the XMM-Newton Survey Science Center ¹ in two complementary energy bands (0.5–4.5 keV and 4.5–7.5 keV) in the bright (above $\sim 7 \times 10^{-14}$ erg cm⁻² s⁻¹) flux regime. The very high identification rate (96%) for the X-ray source sample selected in the 4.5–7.5 keV band is used here to have, in this energy range, an “unbiased” view of the extragalactic hard X-ray sky at bright fluxes.

Key words: Diffuse X-ray Background – X-ray Surveys – Active Galactic Nuclei.

1. INTRODUCTION

Deep *Chandra* and *XMM-Newton* observations have resolved $\sim 80\%$ and $\sim 60\%$ of the 0.5–5 keV and 5–10 keV cosmic X-ray background (CXB) into discrete sources down to $f_x \sim 3 \times 10^{-16}$ erg cm⁻² s⁻¹ and $f_x \sim 3 \times 10^{-15}$ erg cm⁻² s⁻¹, respectively (Worsley et al. 2005 and reference therein).

The X-ray data (stacked spectra and hardness ratios) of these faint samples are consistent with AGN being the dominant contributors to the CXB (Brandt & Hasinger 2005 and references therein; G. Hasinger and Y. Ueda contributions to this meeting) and, as inferred by the X-ray colors, a significant fraction of these sources have hard, presumably obscured, X-ray spectra, in agreement with the predictions of CXB synthesis models (Setti and Woltjer 1989; Comastri et al. 2001; Gilli et al. 2001; Ueda et al. 2003; Treister & Urry 2005).

On the other hand, the majority of the sources found in medium to deep fields are too faint to provide good X-ray spectral information. Furthermore, the extremely faint magnitudes of a large number of their optical counterparts make the spectroscopic identifications very difficult, or even impossible, with the present day ground-based optical telescopes. Thus, notwithstanding the remarkable results obtained by reaching very faint X-ray fluxes, the broad-band physical properties (e.g. the relationship between optical absorption and X-ray obscuration and the reason why AGN with similar X-ray properties have completely different optical appearance) are not yet completely understood. In the medium flux regime a step forward toward the solution of some of these problems has been undertaken by Mainieri et al. (2002), Piconcelli et al. (2003), Perola et al. (2004) and Mateos et al. (2005).

With the aim of complementing the results obtained by medium to deep X-ray surveys, we have built the “The XMM-Newton Bright Serendipitous Source Sample” (Della Ceca et al. 2004). We describe below the main characteristics of this sample and discuss some of the results obtained so far. The contribution of this project to the solution of some critical open (and “hot”) questions like the relationship between optical absorption and X-ray obscuration and the physical nature of the “X-ray bright optically normal galaxies” have been already discussed in Caccianiga et al. (2004) and Severgnini et al. (2003), respectively. We stress that many of these issues are investigated with difficulties when using the fainter X-ray samples because of the typical poor counts statistics available for each source. Here we consider the cosmological model with $(H_o, \Omega_M, \Omega_\lambda) = (65, 0.3, 0.7)$.

2. THE XMM-NEWTON BRIGHT SERENDIPITOUS SOURCE SAMPLE

The XMM Bright Serendipitous Source Survey, a project led by the *Osservatorio Astronomico di Brera*, consists of two flux-limited samples: the XMM BSS and the XMM HBSS sample having a flux limit of $\sim 7 \times 10^{-14}$ erg

¹The XMM-Newton Survey Science Center (SSC, see <http://xmsscwww.star.le.ac.uk>) is an international collaboration, involving a consortium of 10 institutions, appointed by ESA to help the SOC in developing the software analysis system, to pipeline process all the XMM-Newton data, and to exploit the XMM serendipitous detections. The OABrera is one of the Consortium Institutes.

Table 1. The current optical breakdown of the BSS and HBSS samples

	BSS	HBSS
Objects ¹	389	67
Area Covered (deg ²)	28.10	25.17
Identified	308	64
Identification rate	79%	96%
AGN-1	201	38
AGN-2	29	20
Galaxies ²	8	1
Clusters of Galaxies ³	6	1
BL Lacs	6	2
Stars ⁴	58	2

¹ Fifty-six sources are in common between the BSS and HBSS samples; ² we stress that some of the sources classified as “Optically Normal Galaxy” could indeed host an optically elusive AGN (Severgnini et al. 2003); ³ the source detection algorithm is optimized for point-like objects, so the sample of clusters of galaxies is not statistically complete nor representative of the cluster population; ⁴ all but one of the sources classified as stars are coronal emitters. The stellar content of the XMM-BSS has been presented to this meeting by J. Lopez-Santiago.

cm⁻² s⁻¹ in the 0.5–4.5 keV and 4.5–7.5 keV energy bands, respectively. This approach was determined by the need of studying the composition of the source population as a function of the selection band and in order to reduce the strong bias against absorbed sources. which occurs when selecting in soft X-rays.

Two-hundred and thirty-seven suitable XMM fields (211 for the HBSS) at $|b| > 20$ deg were analyzed and a sample of 400 sources was selected (see Table 1 for details and Della Ceca et al. 2004). It is worth noting that among the ongoing surveys performed with *Chandra* and XMM-Newton the XMM BSS survey is currently covering the largest area; furthermore, unlike deep pencil beam surveys, the XMM BSS is unbiased by problems connected to the cosmic variance.

The majority of the BSS X-ray sources have enough statistics (hundreds to thousands counts when the data from the three EPIC detectors are considered) to allow X-ray studies in terms of energy distributions, absorption properties, source extent and flux variability. Moreover the optical counterpart of $\sim 90\%$ of the X-ray sources has a magnitude brighter than the POSS II limit ($R \sim 21$ mag), thus allowing spectroscopic identification at a 2–4 meter class telescope; this fact, combined with the XMM positional accuracy for bright sources (90% error circle of 4'') implies that, in almost all cases, only one object needs to be observed to secure the optical identification.

Up to now 318 X-ray sources have been spectroscopi-

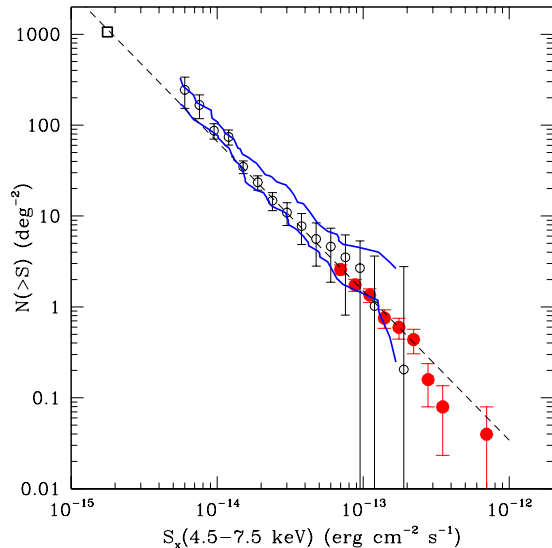


Figure 1. The extragalactic number-flux relationship in the 4.5–7.5 keV energy band obtained using the HBSS sample (binned representation: filled circles). We have also reported for comparison other XMM-Newton based $\text{Log}(N>S)\text{--}\text{Log}S$, obtained in a similar energy range, converted to the 4.5–7.5 keV energy range. In particular we have reported the HELLAS2XMM 5–10 keV $\text{Log}(N>S)\text{--}\text{Log}S$ (area inside the thick solid lines, Baldi et al. 2002) and the AXIS 4.5–7.5 keV $\text{Log}(N>S)\text{--}\text{Log}S$ (open circles, Carrera & Barcons 2005, private communication). The open square at $S \simeq 2 \times 10^{-15}$ ergs cm⁻² s⁻¹ represents the extragalactic surface density in the Lockman hole field according to Hasinger et al. (2001). The dashed line represents the best fit $\text{Log}(N>S)\text{--}\text{Log}S$ obtained using the HBSS source sample (Della Ceca et al. 2004); for comparison the power-law best fit model has been extrapolated down to $\simeq 10^{-15}$ ergs cm⁻² s⁻¹.

cally identified (220 sources from our own observations and the remaining from the literature) leading to a 79% and 96% identification rate for the BSS and HBSS samples respectively (see Table 1 for a summary). The optical selection criteria for the spectroscopic classification have been discussed in Caccianiga et al. (2004) and Della Ceca et al. (2004); a full description of the optical properties of the sources will be presented in Caccianiga et al., in preparation.

3. THE HBSS SAMPLE

The HBSS sample is now almost completely identified (96% of spectroscopic identifications with only three sources currently unidentified), therefore it can be used to have an unbiased view of the high galactic ($|b| > 20$ deg) 4.5–7.5 keV sky in the bright flux regime. First results, based on a complete subsample of 28 objects completely identified, have been already discussed in Caccianiga et al. (2004). We stress that an identification rate around

80% (as e.g. in the BSS sample or in other samples appeared in literature) could be not enough to have this unbiased view. Indeed, interesting classes of X-ray emitting sources (e.g. the narrow line AGN population), which could represent an important minority of the source population, could be more difficult to identify. We concentrate here the discussion on three main results concerning the HBSS sample: the 4.5–7.5 keV extragalactic number-flux relationship, the position of the AGN sample in the L_x - N_H plane, and the correlation between X-ray colours and intrinsic N_H .

3.1. The 4.5–7.5 keV extragalactic number-flux relationship

In Fig. 1 we compare the extragalactic number-flux relationship in the 4.5–7.5 keV energy band obtained using the HBSS sample (binned representation: filled circles) with other XMM-Newton based $\text{Log}(N>S)$ – $\text{Log}S$, obtained in a similar energy domain: the agreement is very good making us confident about the reliability of the data selection and analysis. Furthermore, since we are covering the largest area in the bright flux regime we are able to set the most stringent constraints on the extragalactic source surface densities above $S \simeq 7 \times 10^{-14}$ ergs cm^{-2} s^{-1} . In Fig. 1 we have also reported the best fit power-law $\text{Log}(N>S)$ – $\text{Log}S$ obtained using the HBSS source sample (Della Ceca et al. 2004) extrapolating it down to $\simeq 10^{-15}$ ergs cm^{-2} s^{-1} ; it is clear that we have no compelling evidence of a flattening of the 4.5–7.5 keV energy extragalactic number-flux relationship down to the flux limits sampled so far.

3.2. The $L_x - N_H$ plane

In Fig. 2 we show the intrinsic $L_{(2-10\text{keV})}$ versus intrinsic N_H for the sources belonging to the HBSS sample. Both the intrinsic 2–10 keV luminosity (e.g. de-absorbed from the measured N_H at the source redshift) and the intrinsic N_H have been derived from a complete X-ray spectral analysis using, when possible, data from all the three instruments on-board XMM-Newton (MOS1, MOS2, pn).

As already discussed in Caccianiga et al. (2004) some hot questions could be investigated from a close inspection of Fig. 2, **especially considering the fact that we are dealing with a well defined and complete sample which has been almost completely identified.**

The main results can be summarized in these points:

- We do not find a strong evidence of a large population of absorbed ($N_H > 10^{22}$ cm^{-2}) optically Type 1 AGN. We only have two objects belonging to this category, i.e. about 3% of the total extragalactic population and 5% of the Type 1 AGN population shining in the 4.5–7.5 keV sky at the sampled fluxes. For one of these two objects the X-ray spectra could also be described by a typical Type 1 AGN power-law model with a large relativistic

iron line; a deeper investigation (using all the data in the XMM archive) is in progress to assess the presence of intrinsic absorption. The other absorbed object is a nearby ($z=0.019$) and well known Narrow Line Seyfert 1 galaxy (MKN 1239) studied in X-ray also by Grupe et al. (2004) using pointed XMM observations;

- Among optically Type 2 AGN about 65% are characterized by an $N_H > 10^{22}$ cm^{-2} , 20% by an N_H between $10^{21.5}$ and 10^{22} cm^{-2} and 15% are apparently unabsorbed ($N_H < 10^{21.5}$ cm^{-2} ; the three objects marked with thick arrows). Two unabsorbed sources have an intrinsic luminosity of $\sim 2 \times 10^{42}$ ergs s^{-1} and $\sim 2 \times 10^{43}$ ergs s^{-1} and are both classified as Seyfert 1.9. The latter unabsorbed Type 2 AGN is apparently a high luminosity ($L_X \sim 2 \times 10^{44}$ ergs s^{-1}) narrow line AGN although, unfortunately, the H_α line is not sampled at the moment. Similar unabsorbed Type 2 QSOs have been discussed in Wolter et al. (2005) (see also the A. Wolter contribution to this meeting);

- As already found by other surveys we note a strong deficiency of the number of high luminosity ($L_x > 10^{44}$ erg s^{-1}) absorbed ($N_H > 10^{22}$ cm^{-2}) AGN, the so called absorbed Type 2 QSOs predicted to be a consistent number by the synthesis models of the CXB. The HBSS sample lists 5 Type 2 QSOs with 4 of them having an absorbing column density in a narrow range between 10^{22} cm^{-2} and $\sim 3 \times 10^{22}$ cm^{-2} ;

- At the fluxes covered by the HBSS survey the 4.5–7.5 keV selection is an efficient way to sample AGN with absorbing column densities up to $N_H \simeq 10^{24}$ cm^{-2} . Furthermore we have no strong evidence of $N_H > 10^{24}$ cm^{-2} (e.g. the presence of a strong iron line) for the three optically Type 2 AGN that are unabsorbed in the X-ray regime. Therefore, unless some of our absorbed objects are characterized by a dual absorber model (with an absorbed component not visible below 10 keV) we do not find Compton thick AGN. A new, unexpected and interesting result is that very few Compton thick AGN seem also to emerge from the Swift/BAT and INTEGRAL surveys of the hard (20–100 keV) sky above a flux limit of 10^{-11} ergs cm^{-2} s^{-1} (see V. Beckmann and R. Mushotzky contributions to this meeting). We are now evaluating if the results from the HBSS can be used to constraint the density of the elusive Compton thick AGN at fainter fluxes;

- We only have one object that is optically classified as normal galaxy, but the H_α line is not sampled at the moment. Its absorbing column density and luminosity are highly indicative of the presence of an absorbed AGN. A deeper investigation is in progress.

3.3. X-ray colors versus absorbing column densities

One of the responsibilities of the XMM-Newton SSC is the production of the XMM-Newton Source Catalogue. This catalogue will provide a rich and unique resource for generating well-defined samples for specific studies,

considering the fact that X-ray selection is a highly efficient way of selecting AGN, clusters of galaxies and active stars.

Having completed the X-ray spectral analysis of the sources in the HBSS sample we can investigate the (expected) correlation between the hardness ratios and the absorbing column densities for the AGN population. We have used here the hardness ratios HR2 as defined from the XMM-Newton pipeline processing :

$$HR2 = \frac{C(2 - 4.5 \text{ keV}) - C(0.5 - 2 \text{ keV})}{C(2 - 4.5 \text{ keV}) + C(0.5 - 2 \text{ keV})}$$

where $C(0.5-2 \text{ keV})$, $C(2-4.5 \text{ keV})$ are the “PSF and vignetting corrected” count rates in the 0.5–2 and 2–4.5 keV energy bands, respectively. We stress that a “Hardness Ratio” is often the only X-ray spectral information available for the faintest sources in the XMM-Newton catalogue, and thus, a “calibration” in the parameter space is needed to select “clean” and well-defined samples. With the data we have accumulated so far we can work out this “calibration” for e.g. absorbed AGN.

In Fig. 3 we show the expected correlation between the hardness ratio HR2, the absorbing column densities and the optical spectral properties of the selected AGN.

A few considerations are needed:

- The 4.5–7.5 keV selection, at the flux limits investigated here, seem to be extremely efficient in selecting sources that are described at the “first” order by an absorbed power-law model. This emerge from the consideration that there are very few objects which significantly deviate from the correlation between the hardness ratio HR2 and the N_H . A close inspection of the X-ray spectra of these few sources show best fit spectral models more complex than a simple absorbed power-law. We have some indications that the situation could be a bit more complicated for the sample of sources selected in the 0.5–4.5 keV energy band;
- We strengthen the results first discussed in Caccianiga et al. (2004) and Della Ceca et al. (2004). First, all but one source characterized by an intrinsic $N_H > 10^{21.5} \text{ cm}^{-2}$, have $HR2 > -0.35$. Second, all but 3 of the objects optically classified as Type 2 AGN have $HR2 > -0.35$. Third, only three objects classified as optically Type 1 AGN have $HR2 > -0.35$ and only one of them have (but see the discussion above) $N_H > 10^{22} \text{ cm}^{-2}$.

The results shown in Fig. 3 allow us to design a very simple process to pinpoint absorbed AGN *with very high efficiency* using XMM-Newton data: selection in the 4.5–7.5 keV energy band combined with the condition that the selected sources should have $HR2 > -0.35$. The fact that we are dealing with a well defined and complete sample which has been almost completely identified allows us to make a step forward: from a simple selection of sources to a sample with well defined statistical properties. In fact, using the current HBSS sample as an “unbiased” view of the X-ray sky in the 4.5–7.5 keV energy band, we

gain information on which kind of sources we are leaving out by imposing the constraint of $HR2 > -0.35$. The incoming 2XMM catalog will allow us to build up a sample of about 100 absorbed AGN (from the analysis of about 1000 useful XMM fields) having fluxes above $\sim 10^{-13} \text{ ergs cm}^{-2} \text{ s}^{-1}$. Extrapolating the results obtained so far on the HBSS (Della Ceca et al. in preparation) these sources should allow us to study the cosmological evolution properties (XLF and evolution) of the absorbed AGN population in the luminosity range from 10^{42} to $10^{45} \text{ ergs s}^{-1}$ and up to $z=1$, i.e. a useful redshift and luminosity range to investigate their connection with galaxy evolution and star formation in the Universe (Ballantyne, Everett, & Murray 2005).

ACKNOWLEDGMENTS

We acknowledge partial financial support by ASI (grants: I/R/062/02 and I/R/071/02), by MURST (Cofin-03-02-23) and by INAF. We thank the TNG and the ESO NTT Time Allocation Committee for a generous and continuous allocation of observing time.

REFERENCES

- Baldi, A., et al. 2002, ApJ, 564, 190
- Ballantyne, D.R., Everett, J.E. and Murray N. 2005, in press [astro-ph/0509356]
- Brandt, W.N. & Hasinger, G. 2005, ARAA, 43, 827
- Caccianiga, A., et al. 2004, A&A, 416, 901
- Comastri, A., et al. 2001, MNRAS, 327, 781
- Della Ceca, R., et al. 2004, A&A, 428, 383.
- Gilli, R., et al. 2001, A&A, 366, 407
- Grupe, D., et al. 2004, AJ, 127, 3161
- Hasinger, G., et al. 2001, A&A, 365, L45
- Mainieri, V., et al. 2002, A&A, 393, 425
- Mateos, S., et al. 2005, A&A, 433, 855
- Perola, G.C., et al. 2004, A&A, 421, 491
- Piconcelli, E., et al. 2003, A&A, 412, 689
- Severgnini, P., et al. 2003, A&A, 406, 483
- Setti, G. & Woltjer, L. 1989, A&A, 224, 21
- Treister, E. & Urry, C. M. 2005, ApJ, 630, 115
- Ueda, Y., et al. 2003, ApJ, 598, 886
- Veron-Cetty, M. P. & Veron, P. 2001, A&A, 374, 92
- Wolter, A., et al. 2005, in press [astro-ph/0510045]
- Worsley, M. A., et al. 2005, MNRAS, 357, 1281

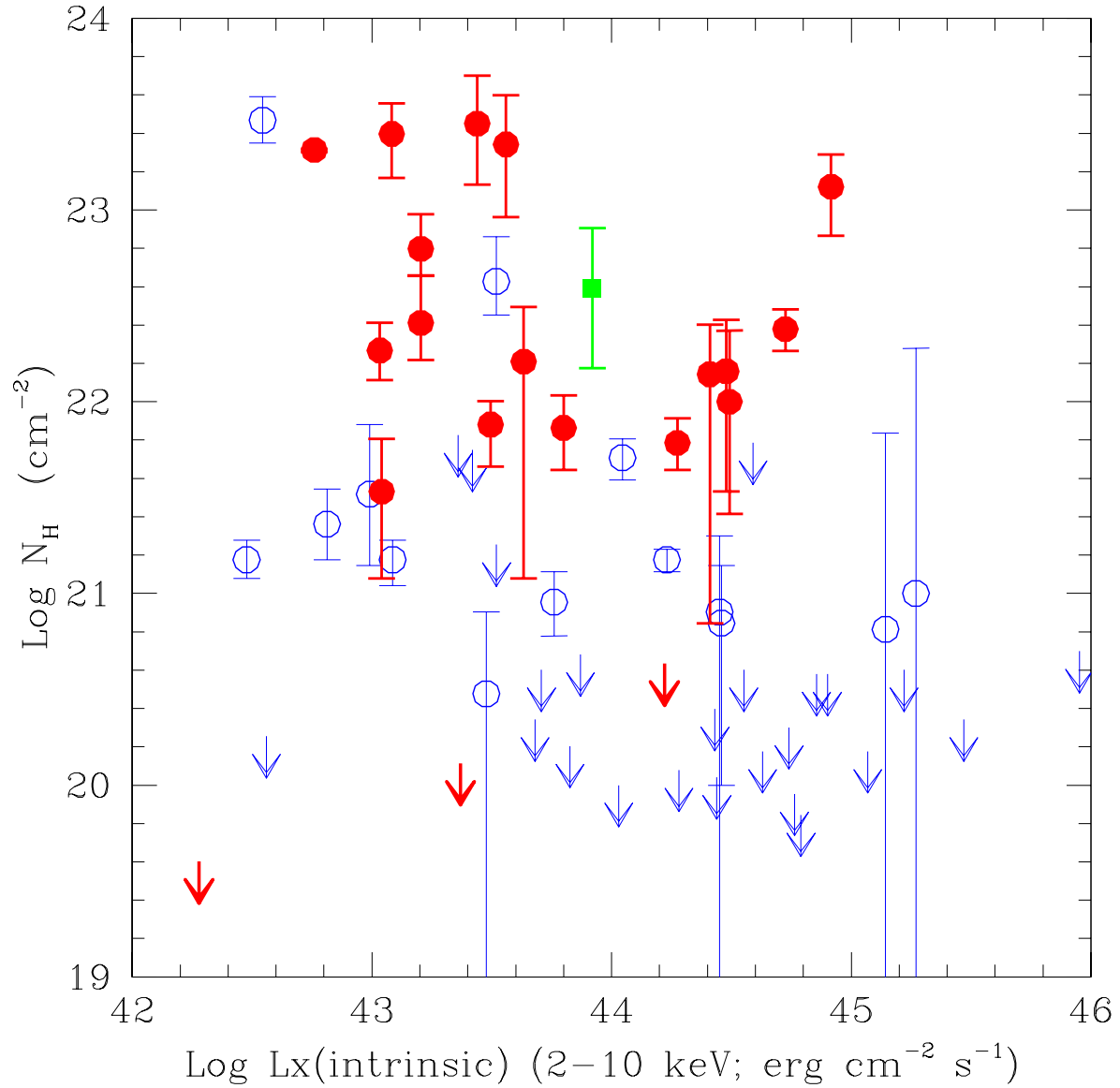


Figure 2. Intrinsic 2-10 keV luminosity versus intrinsic absorption column densities (both quantities derived from a complete spectral analysis) for the sources belonging to the HBS sample. We have used different symbols to mark the different optical classification of the objects. The arrows indicate the 90% upper limit on N_H . Optically Type 1 AGN: open circles and thin arrows. Optically Type 2 AGN: filled circles and thick arrows. Optically normal galaxies: filled squares.

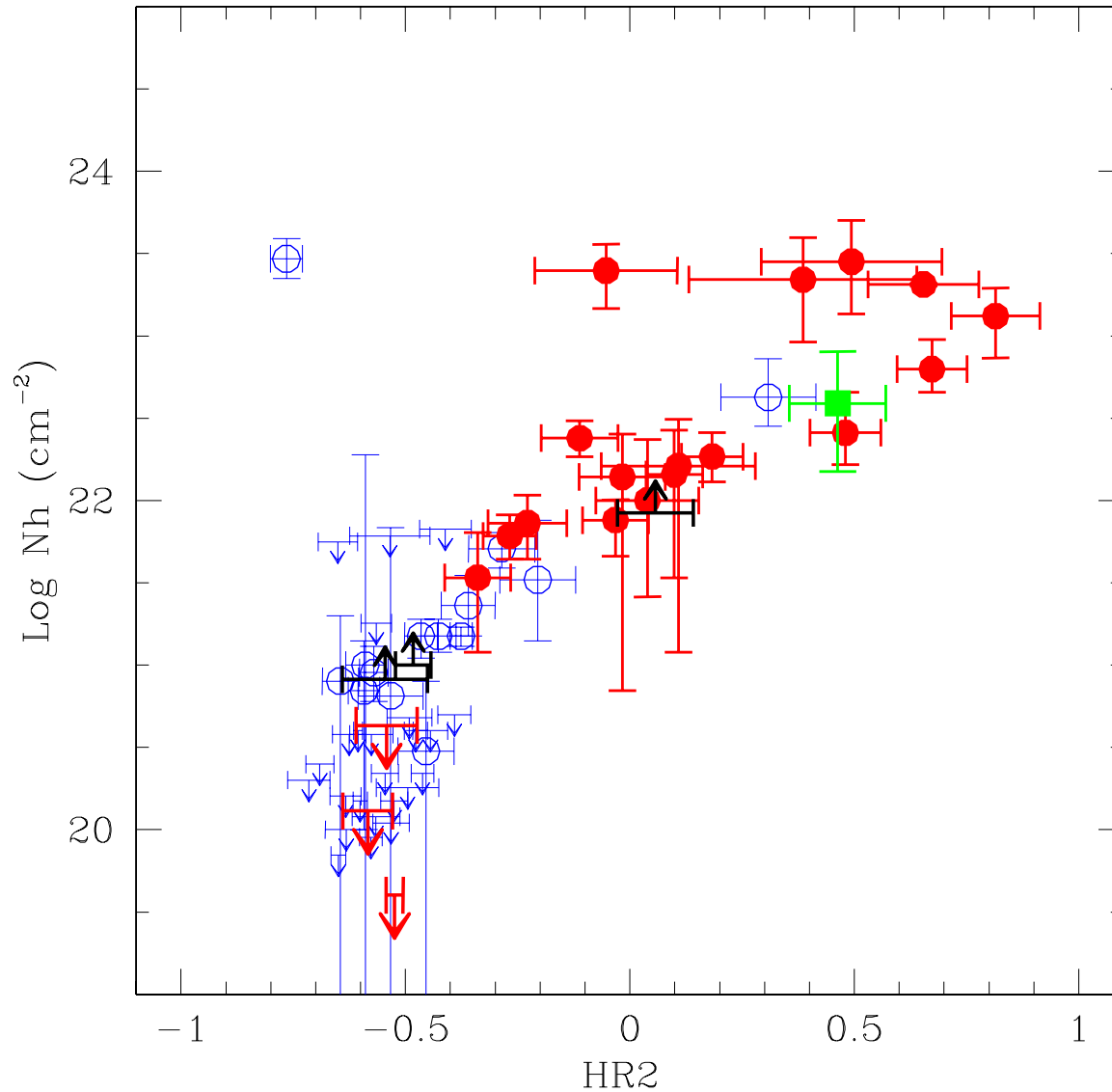


Figure 3. Intrinsic absorbing column densities versus their observed HR2 X-ray colours for the sources in the HBSS sample. The arrows indicated the 90% upper limit on N_H . Symbols are as follows: optically Type 1 AGN – open circles and downward thin arrows; optically Type 2 AGN – filled circles and downward thick arrows; optically normal galaxies – filled squares; unidentified objects – upward thick arrows.

TRACING COSMIC ACCRETION THROUGH THE XMM-NEWTON MEDIUM SURVEY (XMS)

X. Barcons, F.J. Carrera & M.T. Ceballos

Instituto de Física de Cantabria (CSIC-UC), 39005 Santander, Spain

ABSTRACT

We discuss the XMM-Newton Medium Survey (XMS), a large serendipitous X-ray source sample at intermediate X-ray fluxes which is where most of the energy from accretion onto super-massive black holes is released. The XMS is now spectroscopically identified to 85%, and this enables us to study a number of statistical properties of the X-ray source population at these fluxes.

Key words: Active Galactic Nuclei, X-ray Surveys.

1. INTRODUCTION

Serendipitous X-ray source surveys conducted with the help of XMM-Newton observations are yielding a detailed picture of the contents of the X-ray sky, in particular at high galactic latitudes (Watson et al 2001). Although the limited spatial resolution of XMM-Newton does not allow these surveys to go as deep as the ones conducted with Chandra (see Brandt & Hasinger 2005 for a review), the larger collecting area of XMM-Newton along with the larger field of view of the EPIC cameras make XMM-Newton optimum to conduct surveys at intermediate and bright fluxes. At the same time, the large effective area of XMM-Newton ensures that enough counts are accumulated in many of the sources detected as to conduct - at least a simple - spectroscopic analysis.

The XMM-Newton Medium Survey (XMS) was among the first serendipitous X-ray surveys to be started with XMM-Newton. It began as part of the AXIS¹ programme, where a large number of X-ray sources at all galactic latitudes and of various brightness were imaged in the optical and spectroscopically identified. The XMS is a flux limited survey in the 0.5-4.5 keV band (the band was chosen to optimize the sensitivity of XMM-Newton), with a limit of 2×10^{-14} erg cm⁻² s⁻¹. This implies a source density around 100 sources deg⁻² and optical

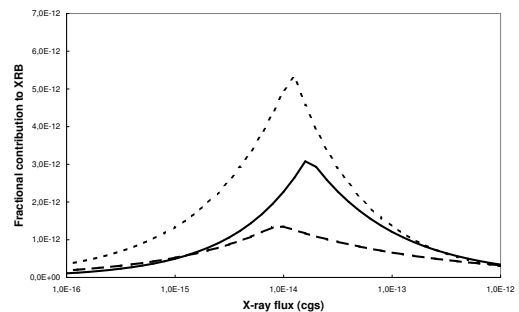


Figure 1. Differential contribution (in arbitrary units) to the XRB per flux decade in the 0.5-2 keV (dashed), 0.5-4.5 keV (continuous) and 2-10 keV (dotted).

counterparts that in their majority are accessible for optical spectroscopy from 4m class telescopes.

There are a number of reasons on why such surveys are important. The first one is that they are needed to bridge the gap between the deep surveys (Hasinger et al 2001, Brandt & Hasinger 2005) and the more local bright surveys (Della Ceca et al 2004, Caccianiga et al 2004). A second reason is that the XMM-Newton source catalogue (of which the first version 1XMM was released in April 2003, and the second one is expected in 2006 containing between 100,000 and 150,000 X-ray sources) is in itself a huge medium sensitivity sample, given the average exposure time of the XMM-Newton observations. By building the XMS we can therefore know how to characterize, and possibly classify, most of the sources in the XMM-Newton catalogue. But possibly the most important reason to pay attention to intermediate flux surveys is that most of the Cosmic X-ray Background (XRB, see Fabian & Barcons 1992, for a still valid review) arises at these fluxes. Fig. 1 shows the fractional contribution to the XRB per flux decade at different fluxes and for various X-ray energy bands, where it is clear that most of the action occurs around intermediate fluxes. More specifically, with the most recent source counts, the XMS

¹An XMM-Newton International Survey,
<http://www.ifca.unican.es/~xray/AXIS>

resolves about 50% of the XRB in its own 0.5-4.5 keV energy band.

In this paper we summarize the XMS and its optical identification status (section 2), the content of the XMS (section 3) and some prospects on statistical identification based upon X-ray and optical colour information (section 4).

2. THE XMS AND ITS OPTICAL IDENTIFICATION

The XMS has been built from a parent serendipitous source list built from 25 XMM-Newton pointings. The fields were selected according to a number of criteria, including being at high galactic latitude ($|b| > 20^\circ$), the EPIC-pn observations being in full frame mode, having a resulting Good Time Interval in this instrument larger than 10 ks, not containing very bright (either in X-rays or in the optical) sources, the target itself not being too much extended and being available early on in the mission. This last point was important, as the first observations were carried out in April 2000.

The data have been reprocessed using the latest available version of the SAS (6.1.1) and best available calibration. This SAS version was used to produce exposure and background maps as well as to search for X-ray sources in the EPIC-pn field of view. Regions around the target, the CCD gaps (where gaps were broadened a bit) and near the pn "Out of Time events" trails were excluded from any further analysis and the corresponding solid angle not computed in the survey. To conduct any X-ray spectral analysis, events were extracted from all 3 EPIC detectors for each source, calibration matrices produced and background spectra extracted. We also constructed empirical sensitivity maps from detected source parameters, from which we computed solid angles. The EPIC-pn source lists were screened in detail to prevent any spurious source entering the final source list.

After this filtering process, the XMS contains 284 X-ray sources brighter than 2×10^{-14} erg cm $^{-2}$ s $^{-1}$ in the 0.5-4.5 keV band, covering a solid angle of 3.3 deg 2 .

To conduct the optical identification of this sample, we first performed optical imaging of the XMM-Newton fields. In all fields but 1, we used the 2.5m INT within the AXIS programme. Sloan filters g' , r' and i' were used in all cases, and in a fraction of them we also obtained images with the u(RGO) and Z (Gunn) filters. The approximate depth of the images is $\sim 23-24$ (depending on seeing, airmass and sky brightness) in r' .

Candidate counterparts for each XMS source were searched for in the r' images (primarily). These X-ray source lists were first registered to the USNO A2 reference frame by applying a possible shift to their coordinates after a number of matches in every field were found. Around the corrected X-ray source positions, candidate

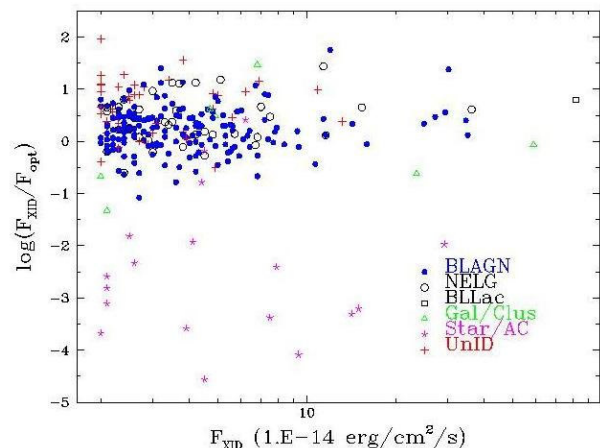


Figure 2. X-ray to optical flux ratio versus 0.5-4.5 keV X-ray flux for the XMS sources. Filled dots are BLAGN, hollow circles are NELGs, triangles are ALGs, asterisks are stars and crosses are unidentified sources.

Table 1. Breakdown of XMS sources.

Sources	Number	%
X-ray	284	100
Identified	242	85
Unid $r' < 20$	6	2.5
Unid $20 < r' < 21$	6	2.5
Unid $21 < r' < 22$	4	1.5
Unid $r' > 22$	26	9
Unid <i>Noimage</i>	1	0

optical counterparts were considered if their position was within a 5σ error circle from the X-ray source (σ is the statistical error in the centroid of the X-ray position, the optical positions being much more accurate) or within $5''$. With this selection criteria the vast majority of the XMS sources had a unique and unambiguous candidate counterpart. Barcons et al (2002) presented the analysis of a 10 times smaller XMS based on 2 XMM-Newton fields only.

Optical spectroscopy was then conducted to properly identify the sources. The AXIS programme provided about 50% of the XMS identifications with the use of fibre and long-slit spectrographs at the 4.2m WHT, the 3.5m TNG and the 2.6m NOT. A further 20% of identifications were obtained in 3 successive runs at the 3.5m telescope in the Spanish German Astronomical Centre in Calar Alto. A further $\sim 15\%$ of the identifications were obtained in a run at the VLT, especially those with a faint optical counterpart. A handful of additional sources had been identified in a variety of telescopes (AAT, SUBARU, etc.). Table 1 shows the breakdown of unidentified sources, classified in terms of their optical magnitude.

The XMS is therefore identified to 85%. There is however an obvious residual bias which is reflected in Tab. 1, as 9% of the full sample remains unidentified and the optical counterparts are fainter than $r' = 22$. These sources cannot be identified with a 4m class telescope, and they are all in the North and inaccessible from the VLT. The impact of these sources is also seen in Fig. 2, as they show up as relatively large F_X/F_{opt} sources, particularly at the faint end of our survey. This very fact implies that some conclusions from the present work are to be considered preliminary until a larger fraction of these sources are spectroscopically identified.

3. THE CONTENT OF THE XMS

3.1. Source counts

We used the full X-ray source lists in the XMM-Newton XMS fields along with the Bright Source Survey (BSS, Della Ceca et al 2004) to build source counts in the 0.5-4.5 keV. Although both surveys operate in the same band, our source lists are derived from EPIC-pn, while the EPIC-MOS2 detector is used for the BSS. As usual a broken power law was fitted to the differential source counts:

$$\frac{dN(S)}{dS} \propto S^{-\Gamma_d} \quad S < S_b \quad (1)$$

$$\frac{dN(S)}{dS} \propto S^{-\Gamma_u} \quad S > S_b \quad (2)$$

The result of the maximum likelihood fitting yields $S_b = 1.69^{+0.02}_{-0.01} \times 10^{-14} \text{ erg cm}^{-2} \text{ s}^{-1}$, with $\Gamma_d = 1.34^{+0.01}_{-0.07}$ and $\Gamma_u = 2.55^{+0.03}_{-0.04}$. The fact, already seen in other bands, that the source counts flatten from euclidean ($\Gamma_u \sim 2.5$) to highly sub-euclidean implies that most of the contribution to the XRB in this band arises from sources around S_b (see Fig. 1). Ebrero et al. (2006, this volume) discuss source counts in other X-ray bands.

3.2. The identified sources

The 242 identified sources have been classified solely in terms of their optical spectrum. Extragalactic sources have been divided in Broad-line Active Galactic Nuclei (BLAGN) when permitted lines are broader than 2000 km s^{-1} , Narrow-line Emission Galaxies (NELG) when emission lines are narrower than the above limit, and Absorption Line Galaxies (ALG) when no emission line can be detected. One of the ALGs is a catalogued BL Lac and therefore is classified as such. At least two of the X-ray sources where the counterpart is an ALG show some evidence of a galaxy overdensity, and therefore could be groups or clusters. We do not separate clusters as a subclass any further, as this will require a proper assessment

Table 2. Breakdown of XMS identifications. Percentages refer to the identified sources (242)

Source Class	Number	%
Total id	242	100
BLAGN	178	74
NELG	37	15
ALG	8	4
Stars	18	7
BL Lac	1	0

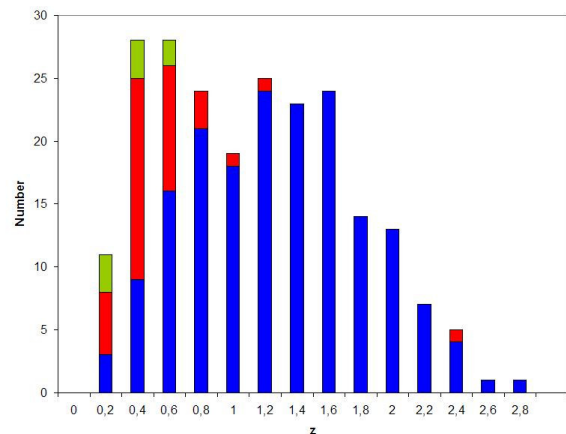


Figure 3. Redshift distribution of the extragalactic component of the sources identified in the XMS. Dark is for BLAGN, lighter for NELG and still lighter for ALG.

on whether the X-ray source is extended or not and a proper quantification of galaxy number densities around all sources. This work is now in progress. Finally, a number of stars were found as counterparts. Table 2 shows the breakdown of the identified sources.

The results from the identifications conducted so far reveal that BLAGN dominate the source population at this flux limit. The X-ray luminosity of all of the extragalactic sources, but one ALG, is in excess of $10^{42} \text{ erg s}^{-1}$ and are therefore consistent with being powered by an AGN. Assuming that NELG and ALG are obscured AGN, they represent 25% of the whole AGN population at this flux level.

The redshift distribution of the XMS sources identified as extragalactic is shown in Fig. 3. We see that most of the "obscured" AGN lie at relatively low redshift, although a few high-luminosity examples of these (i.e., type 2 QSOs) are also found in the sample.

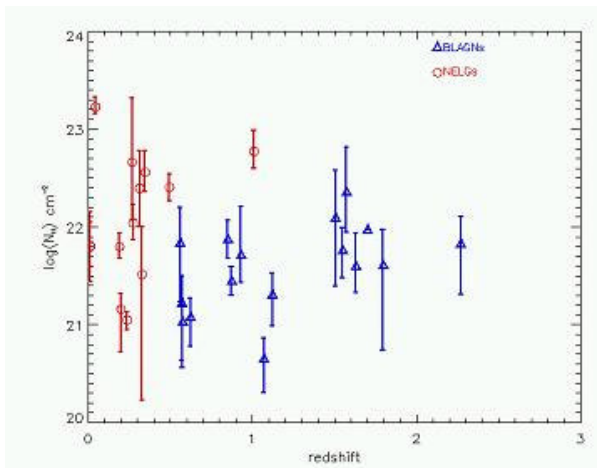


Figure 4. Intrinsic absorption column density versus redshift for those AGN where absorption is detected. Adapted from Mateos et al. (2005).

3.3. X-ray spectral properties of XMS sources

Mateos et al (2004) have studied the X-ray spectral properties of a superset of the XMS sample, consisting of ~ 1000 X-ray sources with fairly good spectral quality. The main results from that work are that a fraction $< 10\%$ of the BLAGN are moderately absorbed in X-rays, and that in the NELGs absorption is common, typically with higher column densities, but not universal. Fig. 4 illustrates this. These results are consistent with previous work from Piconcelli et al (2002) and have been confirmed by Mateos et al (2006) from the study of the much better quality X-ray spectra of serendipitous sources in the Lockman Hole.

A lot of excitement has recently arisen on the detection of a large equivalent width Fe emission line in the average, de-redshifted spectra of type 1 and type 2 AGN. The results from Streblyanska et al (2005), based on XMM-Newton observations of the Lockman Hole, are now at least qualitatively confirmed by Brusa et al (2005) using Chandra data. Corral et al. (2006, this volume) report on preliminary results from a similar exercise conducted with the XMS. Although the quality of individual spectra is much lower than that of the Lockman Hole survey, the number of BLAGN is much larger. These preliminary results appear to indicate an Fe line in the average spectra too, again in qualitative agreement with previous work.

4. TIPS FOR STATISTICAL IDENTIFICATION

Although the incompleteness in the identifications of the XMS, with a bias against high X-ray to optical flux ratio sources, prevents us from computing X-ray luminosity functions and other overall statistical descriptors of the sample itself, other applications can be already explored at its current stage. In what follows we will present a few

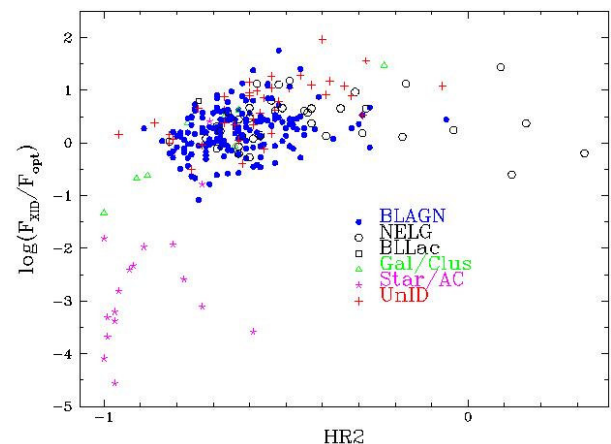


Figure 5. X-ray to optical flux ratio as a function of the hardness ratio HR_2 . Symbols as in figure 1.

preliminary tips on the classification of XMS sources, based on X-ray properties and optical photometric properties. The ultimate goal of all this is to develop a statistical identification tool, whereby X-ray sources in the XMM-Newton source catalogue can be classified without the costly optical spectroscopy in hand. In a second step, and with enough optical photometric data available, even approximate redshifts could be obtained.

To properly develop a statistical identification tool will ultimately require some sort of mathematical algorithm like a principal component analysis, an artificial neural network or some other sophisticated tool. This is well beyond the scope of the present discussion, where we only aim at exploring the parameter space in the search of potentially interesting quantities that can guide the statistical identification process.

The first diagram we explore is the X-ray to optical flux ratio versus X-ray hardness ratio HR_2 defined as

$$HR_2 = \frac{H - S}{H + S} \quad (3)$$

where H and S are the exposure-time corrected count rates in the 2-4.5 keV and 0.5-2 keV bands respectively. Fig. 5 shows the location of XMS sources in this diagram, already used by Della Ceca et al (2004). This diagram is very useful indeed to separate the stars from the sample, as all sources with $F_X/F_{opt} < 0.1$ are either stars or ALGs. Stars are the only point-like objects in this part of the diagram, the remainder being ALGs. Only 2 out of our 18 stars do not reside in this part of the diagram.

The very soft ($HR_2 < -0.85$) part of this diagram at larger F_X/F_{opt} is dominantly populated by ALGs. In these sources it is likely that a soft excess possibly due to the host galaxy provides an important contribution to the X-ray spectrum, although most likely the majority of the X-ray flux is dominated by an AGN, given the large X-ray to optical flux ratio.

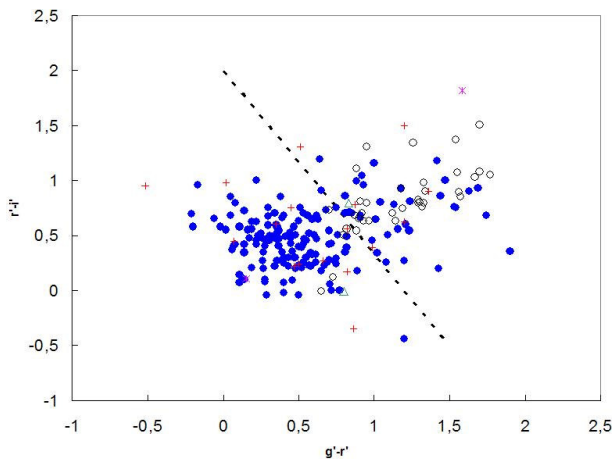


Figure 6. Optical colour-colour diagram for XMS sources. The dotted line separates approximately the QSO and emission line galaxy location (bottom left) from the early type galaxy location (top right) in the SDSS. Labels as in fig. 1.

Working from the opposite end in HR_2 , all sources with $HR_2 > 0$ are NELGs. When going to lower values of HR_2 , the contamination from BLAGN starts to appear, possibly because some of them display photoelectric absorption as discussed in section 3.2. At $HR_2 > -0.4$ and $F_X/F_{opt} > 0.1$ only $> 50\%$ of the objects are NELGs and $> 20\%$ are BLAGN.

A further parameter space worth inspecting is the optical colour-colour diagram (Fig. 6). Since these are Sloan colours, we can compare the location of our sources with those from the SDSS as in Barcons et al (2002). The dotted line separates the expected location of blue galaxies (QSOs and emission line galaxies) from that of red early type galaxies in the SDSS. Barcons et al (2002) noted in their much more reduced XMS sample that the optically red part of that diagram was almost entirely populated by NELGs. With our current sample we now see that optically red objects are almost 50/50 BLAGNs and NELG+ALG. In fact, about 10% of our BLAGN are red. A preliminary inspection does not show a one to one relation between red and X-ray absorbed BLAGN, but this needs more work. The optically blue part of this diagram is, however, almost entirely populated by BLAGN, but still with some exceptions, like 10% of the NELGs.

We finally inspect an optical colour vs X-ray hardness ratio diagram, as shown in Fig. 7. Not surprisingly the blue part of this diagram is almost entirely populated by BLAGN (again with a few exceptions), but the red part shows some interesting hints. In fact, the combination of red and hard picks up almost nothing but NELGs, and the red and soft part is especially rich in ALGs.

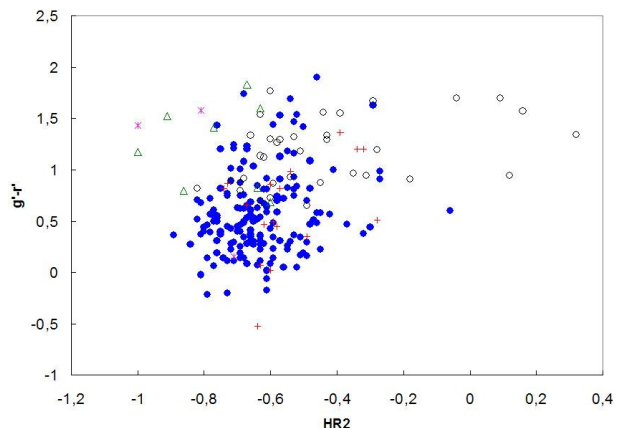


Figure 7. Optical colour versus X-ray hardness ratios of XMS sources. Labels as in fig. 1.

5. OUTLOOK

We have presented preliminary results on the XMS. Although incomplete optical identification prevents us from reaching stronger conclusions, we foresee directions where progress can be made in the immediate future, concerning statistical identification. The parameter space that can be built with X-ray and optical photometric parameters only is huge, and we have explored some interesting subspaces. What we have explored so far indicates that a classification based on a few parameters like F_X/F_{opt} , HR_2 , extent of the optical counterpart, $g' - r'$ and $r' - i'$ can yield without much sophistication to a classification of serendipitous X-ray sources which is reliable to $> 90\%$. In the near future we will cover this with the appropriate mathematical apparatus to provide a preliminary statistical identification tool for the XMM-Newton source catalogue. Unfortunately, photometric redshifts do not appear to work with our limited set of optical filters, even by reducing the number of templates in view of the classification of the source.

ACKNOWLEDGMENTS

We are grateful to a large number of people for a long-standing collaboration in building the XMS, including the AXIS collaboration and to the full XMM-Newton Survey Science Centre. Special thanks are due to S. Mateos, A. Corral, F. Panessa, J. Ebrero, M.J. Page, A. Schwobe, M.G. Watson, R. Della Ceca, J.A. Tedds, W. Yuan, R.G. McMahon and T. Maccararo. Partial financial support was provided by the Spanish Ministerio de Educación y Ciencia, under project ESP2003-00812.

REFERENCES

- [1] Barcons, X., et al., 2002, A&A, 382, 522
- [2] Brandt, W.N. & Hasinger G., 2005, ARAA, 43, 827
- [3] Brusa, M., Gilli, R., Comastri, A., 2005, ApJ, 621, L5
- [4] Caccianiga, A., et al., 2004, A&A, 416, 201
- [5] Corral, A., et al, 2006, these proceedings
- [6] Della Ceca, R., et al., 2004, A&A, 428, 383
- [7] Ebrero, J. et al., 2006, these proceedings
- [8] Hasinger, G., et al., 2001, A&A, 365, L45
- [9] Mateos, S. et al., 2005, A&A, 433, 855
- [10] Mateos, S. et al., 2006, A&A, in the press (astro-ph/0506718)
- [11] Piconcelli, E., Cappi, M., Bassani, L., Fiore, F., Di Cocco, G., Stephen, J.B., 2002, A&A, 394, 835
- [12] Streblyanska A., et al., 2005, A&A, 432, 395
- [13] Watson, M.G. et al., 2001, A&A, 365, L51

EXTENDING THE X-RAY LUMINOSITY FUNCTION OF AGN TO HIGH REDSHIFT

J. Silverman¹, P. Green², W. Barkhouse², R. Cameron², M. Kim², D.-W. Kim², B. Wilkes², G. Hasinger¹, and the full ChaMP project²

¹Max-Planck-Institut für extraterrestrische Physik, D-84571 Garching, Germany

²Harvard-Smithsonian Center for Astrophysics, 60 Garden Street, Cambridge, MA 02138

ABSTRACT

X-ray surveys of the extragalactic universe are now able to detect significant numbers of AGN out to high redshift ($z \sim 5$). We highlight some results from the *Chandra* Multiwavelength Project (ChaMP) to measure the X-ray luminosity function out to these early epochs. At $z > 3$, we show that the comoving space density of luminous ($\log L_X > 44.5$) AGN has a behavior similar to the optical QSO luminosity function. With a newly compiled sample of AGN from ChaMP supplemented with those from additional surveys including the *Chandra* Deep fields, we present a preliminary measure of the luminosity function in the hard (2-8 keV) band. With 37 AGN at $z > 3$, we continue to see a decline in the space density at high redshift over a wider range in luminosity. We discuss the need to identify a larger sample of obscured AGN at high redshift to determine if an early epoch of hidden supermassive black hole growth occurred.

Key words: galaxies: active — quasars: general — X-rays: galaxies — surveys.

1. INTRODUCTION

Our present understanding of the evolution of accreting supermassive black holes (SMBHs) over vast lengths of cosmic time comes from our measure of the luminosity function (i.e. the number undergoing a luminous phase within a specific comoving volume as a function of luminosity and redshift). Energy production through mass accretion onto SMBHs allows us to identify these sites that manifest themselves observationally as the familiar Active Galactic Nuclei (AGN). The luminosity function provides a key constraint to discern the underlying black hole mass and accretion rate distributions as a function of redshift from the observed global properties of AGN. An accurate assessment of these should elucidate the mechanisms (i.e. galaxy mergers and/or self-regulated growth) that are instrumental in their formation and evolution.

To date, an enormous effort has been undertaken to measure the luminosity function over the wide range in luminosity spanned by AGN out to high redshift. The bright end has been well established to $z \sim 5$ by optical imaging surveys which primarily select QSOs using a multi-color criteria. The most dramatic feature found is the rise and fall of the comoving space density with peak activity at $z \sim 2.5$. With an unprecedented sample of 23,338 in the 2dF QSO Redshift Survey (2QZ), Croom et al. (2004) convincingly show a systematic decrease in luminosity (pure luminosity evolution; PLE) from $z = 2$ to the present with very few bright QSOs in the local universe in compliance with past surveys (e.g. Boyle et al. 1988). This fading of the luminous QSO population may be due to a decrease in the mass accretion rate (e.g. Cavaliere & Vittorini 2000) that appears to be linked to the evolution of the galaxies in which they reside (e.g. Croton et al. 2005; Di Matteo et al. 2005). The dropoff in the space density at $z > 3$ (Warren, Hewett & Osmer 1994; Schmidt, Schneider & Gunn 1995; Fan et al. 2001; Wolf et al. 2003) may be indicative of either the detection of the onset of accretion onto young SMBHs or a high-redshift population that has been missed, possibly under a veil of obscuration (Fabian 1999). Excessive amounts of dust and gas may be ubiquitous in galaxies at early epochs as a result of enhanced galaxy formation.

It has been evident for quite some time that optical surveys miss a significant fraction of the AGN population. With the luminosity function being a steeply declining function of luminosity, optical techniques fail to find the majority of AGN due to spectroscopic dilution by host galaxy starlight. Though current techniques do show considerable improvement (Richards et al. 2005), they still fail to account for many low luminosity AGN selected by other means. Of equal significance, many AGN (e.g. Seyerts 2s) are underrepresented due to intrinsic dust obscuration and can only be adequately selected in the low redshift universe (e.g. Hao et al. 2005). As pertinent for this proceeding, current models and recent observations continue to attribute the bulk of the Cosmic X-ray Background (CXRB), the previously unresolved X-ray emission, to various types of obscured AGN (see Brandt & Hasinger 2005 for a review).

In the current era of *Chandra* and *XMM-Newton*, X-ray surveys are detecting AGN and QSOs not only enshrouded by heavy obscuration ($N_H > 10^{22} \text{ cm}^{-2}$) but those at high redshift ($z > 3$) with statistics comparable to the optical surveys due to their superb resolving power between 0.5 to 10 keV. Previous observatories such as *EINSTEIN* and *ROSAT* were limited to the soft band which biases samples against absorption. With 1-2 Msec observations of the *Chandra* Deep Field North (CDF-N; Alexander et al. 2003), Deep Field South (CDF-S; Rosati et al. 2002) and Lockman Hole (Hasinger et al. 2001), $\sim 89\%$ of the hard (2-8 keV) CXRB has been resolved into point sources (Moretti et al. 2003). Many of the hardest serendipitous sources found so far arise in optically unremarkable bright galaxies (e.g. Barger et al. 2003b; Tozzi et al. 2001; Mainieri et al. 2002), which can contain very heavily obscured AGN.

A more robust luminosity dependent evolutionary scheme (see Miyaji, Hasinger & Schmidt 2000) has emerged in recent measures of the X-ray luminosity function (XLF). With the inclusion of absorbed AGN from *Chandra*, *XMM-Newton* and *ASCA* surveys, lower luminosity AGN are clearly more prevalent at lower redshifts ($z < 1$) than those of high luminosity that peak at $z \sim 2.5$. This behavior has been well substantiated using hard (2-8 keV) X-ray selected surveys of all types of AGN (Cowie et al. 2003; Barger et al. 2003a; Ueda et al. 2003; Fiore et al. 2003; Silverman et al. 2005b; La Franca et al. 2005). Using a highly complete soft (0.5-2.0 keV) band selected sample of over 1000 type 1 AGN, Hasinger, Miyaji & Schmidt (2005) show that this LDDE model accurately fits the data and shows a gradual shift of the peak in the comoving space density to lower redshifts with declining luminosity. In contrast to an evolution model in which SMBHs at low redshifts have sub-Eddington accretion rates, this behavior may be evidence for the growth of lower mass black holes emerging in an 'anti-hierarchical' or "cosmic downsizing" fashion while accreting near their Eddington limit (e.g. Merloni et al. 2004; Marconi et al. 2004).

Even though this model is quite convincing, there are remaining uncertainties in our current measure of the XLF. (1) A significant number of X-ray sources in the recent surveys with *Chandra* and *XMM-Newton* are not identified. (2) Barger et al. (2005) demonstrate that the XLF can be fit equally well by a PLE model at $z < 1.2$. These models only begin to substantially differ at low luminosities (i.e. below the break) and higher redshifts where statistics are quite low with most being provided by the CDF-N and CDF-S observations. New moderate depth surveys such as the Extended Chandra Deep Field South (E-CDF-S; Lehmer et al. 2005) and the Groth strip (Nandra et al. 2005) will provide additional AGN at these luminosities and redshifts but await optical followup. (3) Behavior of the AGN population at redshifts above the peak is still not accurately constrained. We have presented preliminary evidence (Silverman et al. 2005b) for a similar evolution of luminous X-ray selected QSOs to those found in the optical surveys with a decline in the comoving space density at $z > 3$ but these AGN are mainly

unobscured (type 1). In consideration of similar findings from radio selected surveys (Wall et al. 2005) that are sensitive to obscured QSOs, our current understanding of the evolution of high redshift AGN may endure.

In this proceeding, we present some results from the ChaMP that extend our knowledge of the X-ray luminosity function at high redshift. We also present some preliminary results from our effort to measure the X-ray luminosity function in the hard (intrinsic 2-8 keV) band. These new results will be further elaborated and expanded to include model fits using a maximum likelihood method in a near future ChaMP paper (Silverman et al. in preparation). To date, the limited numbers of X-ray selected AGN at $z > 3$ have constrained current measures (Ueda et al. 2003; Barger et al. 2005) to lower redshifts. Due to the rarity of luminous high redshift AGN, such an endeavor requires a survey that covers a wide enough area to sufficient depths. The *Chandra* Multiwavelength Project (ChaMP) is carrying out such a survey. To improve the dynamic range ($L_X - z$ coverage) of our sample, we include those AGN found in the CLASXS (Yang et al. 2004; Steffen et al. 2004), the deep surveys with *Chandra* (i.e. CDFN, CDFS) and *XMM-Newton* Lockman Hole (Hasinger et al. 2001) that have published catalogs with a fair sample of low luminosity ($42 < \log L_X < 44$) AGN out to $z \sim 5$.

Throughout this work, we assume $H_0 = 70 \text{ km s}^{-1} \text{ Mpc}^{-1}$, $\Omega_\Lambda = 0.7$, and $\Omega_M = 0.3$.

2. CHANDRA MULTIWAVELENGTH PROJECT (CHAMP)

The ChaMP (Kim et al. 2004a,b; Green et al. 2004) is carrying out an extragalactic X-ray survey encompassing 10 deg^2 using serendipitous detections in archival *Chandra* fields. We have chosen 27 of the 135 ChaMP fields (2.0 deg^2) for which we have acquired extensive followup optical imaging and spectroscopy. The deepest observations have exposure times that are sensitive to sources with $f_{0.5-2.0\text{keV}} > 5 \times 10^{-16} \text{ erg cm}^{-2} \text{ s}^{-1}$. A full description of the ChaMP image reduction and analysis pipeline XPIPE can be found in Kim et al. 2004a. With our 4m MOSAIC optical imaging, we are able to identify counterparts to the *Chandra* sources down to $r' \sim 25$ (Green et al. 2004). We acquire optical imaging in three (g' , r' , and i') Sloan Digital Sky Survey (SDSS) filters. Optical colors provide preliminary source classification and crude photometric redshifts. Optical spectroscopic followup currently focuses on identifying counterparts with $r' < 23.0$ for which spectra can be acquired on a 4-6m (i.e. MMT, Magellan, WIYN, CTIO Blanco) class telescope. To date, we have spectroscopically classified a sample of ~ 450 AGN.

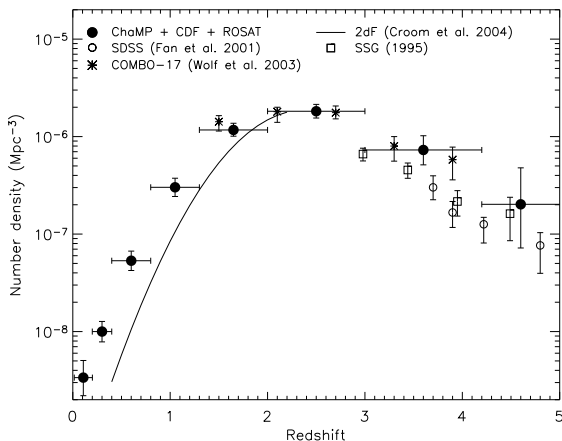


Figure 1. Co-moving space density of 217 Chandra + ROSAT AGN selected in the soft (0.5–2.0 keV) band with $\log L_X > 44.5$ compared to the optical surveys. The optical space densities have been scaled to match the X-ray points at $z = 2.5$ for ease of comparison.

3. CO-MOVING SPACE DENSITY OF LUMINOUS AGN

Using AGN from the ChaMP and those from additional surveys (CDF-N, CDF-S, *ROSAT*), we have measured the co-moving space density type 1, highly luminous ($\log L_X > 44.5$) AGN. In Figure 1, the space density rises from the present epoch to a peak at $z \sim 2.5$ and then declines at $z > 3$ (Silverman et al. 2005b). This behavior is similar to that of optically selected samples (Fan et al. 2001; Schmidt, Schneider & Gunn 1995; Wolf et al. 2003). These results are further substantiated by the recent space densities of soft X-ray selected AGN reported by Hasinger, Miyaji & Schmidt (2005) and radio selected QSOs (Wall et al. 2005). These results all support the scenario that SMBHs are rapidly growing at the early epochs possibly related to enhanced galaxy formation.

4. HARD X-RAY LUMINOSITY FUNCTION

We are also generating a X-ray luminosity function in the 2–8 keV band to minimize the effect of intrinsic absorption. Similar to Barger et al. (2005), we use the observed soft X-ray band for AGN selection above a specific redshift, in our case this is $z = 3$ where we measure the rest frame energies above 2 keV. The hard band (2–8 keV) detections are used to construct a low redshift ($z < 3$) sample of AGN. This enables our selection to be less affected by absorbing columns up to $N_H \sim 10^{23} \text{ cm}^{-2}$. The use of the soft (0.5–2.0 keV) band allows us to take advantage of Chandra’s high collecting area at low energies to detect faint, high redshift AGN. We compile both a sample of AGN from 896 hard and 1232 soft selected X-ray sources found in 27 ChaMP fields. These fields were

chosen to have a limiting flux ($f_{0.5-2.0 \text{ keV}} \sim 10^{-15} \text{ erg s}^{-1} \text{ cm}^{-2}$) capable of detecting high redshift AGN, quality optical imaging in the r' band for the low redshift ($z < 3$) sample, i' for the higher redshift sample, and a substantial amount of optical spectroscopic followup. We further restrict our hard band catalog to those with $r' < 22.5$ and the soft band sources to $i' < 23.5$ since our spectroscopic followup campaign has provided a significant number of spectroscopic redshifts brighter than these magnitude limits. To construct a pure AGN sample, we require the rest frame 2.0–8.0 keV luminosity (uncorrected for intrinsic absorption) to exceed $10^{42} \text{ erg s}^{-1}$. These selection criteria yield a sample of 360 AGN (Figure 2) from the ChaMP with 18 at $z > 3$ that represents half of the known X-ray selected AGN at high redshift.

4.1. Covering the luminosity-redshift plane

We supplement the ChaMP AGN with those from the following hard X-ray surveys to measure the XLF over the wide range of luminosity and redshift spanned by AGN: *Chandra* Deep Field North (CDF-N; Alexander et al. 2003, Barger et al. 2003b), *Chandra* Deep Field South (CDF-S; Giacconi et al. 2002; Szokoly et al. 2004; Zheng et al. 2004), *Chandra* Large Area Synoptic X-ray Survey (CLASXS; Yang et al. 2004, Steffen et al. 2004), *XMM-Newton* Lockman Hole (Brunner et al. in preparation), ASCA Medium Sensitivity Survey (AMSSn; Akiyama et al. 2003). Both a hard and soft X-ray catalog are constructed as implemented for the ChaMP sample. Multi-band optical imaging in these fields allows us to convert optical magnitudes to the SDSS filter system (r', i') used by the ChaMP. The distribution in luminosity and redshift of the full AGN sample is shown in Figure 2. As evident, the deep surveys (i.e. CDF-N and CDF-S) are instrumental to detect low luminosity ($\log L_X < 44$) AGN above a redshift of 1.5. In contrast, the ChaMP supplies the more luminous $\log L_X > 44$ AGN underrepresented in the deep fields.

4.2. Method

We measure the differential X-ray luminosity function ($d\Phi/d\log L$) expressed in Equation 1 where N is the number of AGN per unit comoving volume (V) per $\log L_x$ as a function of luminosity L_x and redshift z .

$$\frac{d\Phi(L_x, z)}{d\log L_x} = \frac{d^2 N}{dV d\log L_x}(L_x, z) \quad (1)$$

This function is assumed to be continuous over the range in luminosity and redshift for which our survey is sensitive. The differential luminosity ($d\log L$) is expressed as a logarithm (base 10) due to the 4 orders of magnitude spanned by our sample.

Here, we estimate the XLF in fixed luminosity and redshift bins using the $1/V_a$ method (Schmidt 1968; Avni &

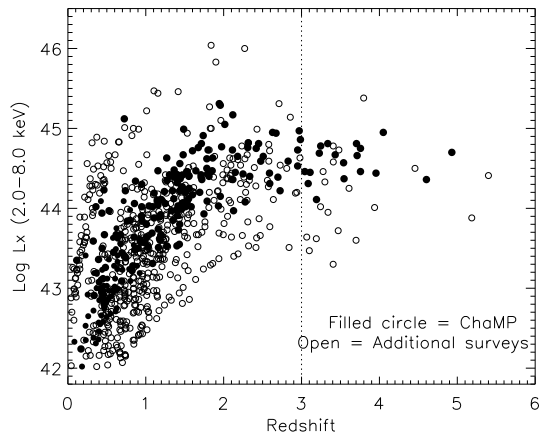


Figure 2. Luminosity-redshift distribution of AGN from the ChaMP (filled circles) and those from the CDF-N, CDF-S, XMM/Lockman Hole, AMSSn and CLASXS (open circles).

Bahcall 1980). For each $L - z$ bin, the value of the XLF is a sum (Equation 2) of the contribution from each AGN falling within this specific bin.

$$\frac{d\Phi(L_X, z)}{d\log L_X} = \frac{1}{\Delta\log L_X} \sum_{i=1}^N C_i \frac{1}{V_{a,i}} \quad (2)$$

We must apply a correction factor (C_i) for each AGN to account for the incompleteness in our optical spectroscopic identifications. This factor is reciprocal of the fraction of identified sources (f_{ID}) at X-ray fluxes and optical magnitudes comparable to each source. The accessible volume V_a is a function of both X-ray and optical limiting fluxes. Further details on our measure of both V_a and f_{ID} are given in Silverman et al. (2005b). We estimate 1σ errors based on a Poisson distribution due to the small number of objects per redshift bin.

Since we have a sample selected in two different energy bands, the survey area over which we are sensitive to an individual AGN depends on the observed flux. The sky coverage for AGN at $z < 3$ depends on their hard flux while higher redshift AGN depend on their soft flux.

4.3. Preliminary results

In Figure 3, we plot the binned XLF in three redshift intervals to highlight the strong evolutionary trends. The luminosity function over the full redshift interval $0 < z < 5.5$ will be presented as mentioned in an upcoming paper (Silverman et al., in preparation). The XLF at $z < 2.0$ is well approximated by the familiar double powerlaw where we have sufficient statistics to cover the full luminosity range. There is a strong increase in characteristic luminosity for the entire sample to $z = 2$. To eval-

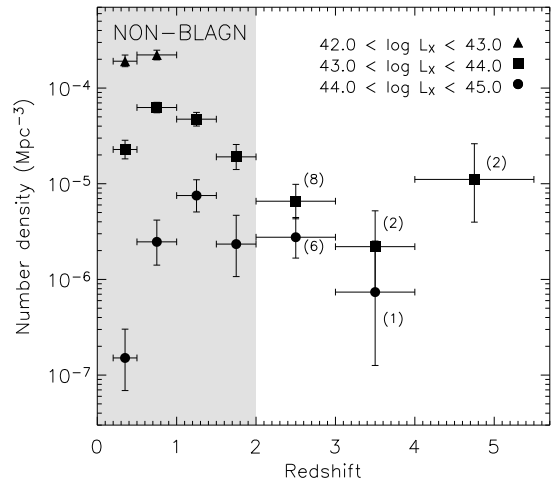


Figure 4. Comoving space density of AGN without broad optical emission lines in their optical spectra. The white area highlights the redshift range where samples are quite limited with the number given in parenthesis.

uate our XLF, we have plotted the best fit pure luminosity evolution (PLE) model from Barger et al. (2005) and luminosity-dependent density evolution (LDDE) model of Ueda et al. (2003). Due to the similarity of both these models at $z < 1.5$, it is difficult to determine which one better matches our data. There may be some evidence of a flattening of the slope at the faint end ($\log L_X < 44$) for $1.5 < z < 2.0$ that may agree with a LDDE model but any solid evidence of this requires a more sophisticated analysis.

We find that the Ueda model provides a good fit to our data for $z < 3$. At higher redshifts ($3 < z < 4$), we see a decline in the overall numbers of AGN at all luminosities, similar to the decline present in the soft selected samples (Figure 1). With this new sample, we are able to further constrain the slope and normalization of the XLF at these high redshifts.

With knowledge of the optical spectral properties of these AGN, we can investigate the evolution of those with a hidden broad emission line region. With the exception of those at low luminosity, these AGN are usually obscured and many can be optically classified as type 2 in compliance with unification models. In Figure 4, we plot their comoving space density in three luminosity classes. First, it is quite evident from the error bars in Figure 4 that the sample is much smaller. Even with this limited sample, it appears qualitatively that more luminous AGN peak at earlier epochs ($z \sim 2$) than those of lower luminosity ($z < 1$) similar to the behavior of the type 1 AGN population (Hasinger, Miyaji & Schmidt 2005). This may imply that type 1 and type 2 AGN evolve in a similar manner and an obscured epoch of AGN formation is not evident. Larger samples are clearly needed to substantiate any such claims.

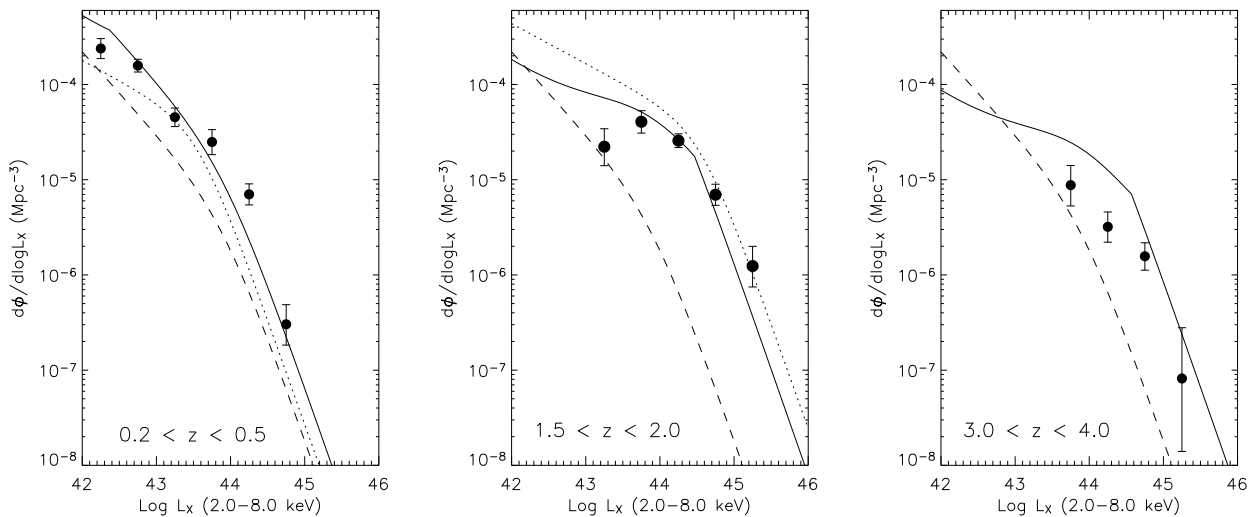


Figure 3. Binned XLF ($1/V_a$ method) in three redshift intervals. The LDDE model with best fit parameters from Ueda et al. (2003) are plotted at the median redshift (solid line) and $z = 0$ (dashed line). We extrapolate the model to $z > 3$ to illustrate the significance of the decrease in normalization of the XLF at high redshift. The pure luminosity evolution model of Barger et al. (2005) is shown by the dotted line and extrapolated up to $z = 2$.

5. CONCLUSION

Even with a further understanding of the evolution of X-ray selected AGN at high redshift, we are continuing to identify a larger sample of ChaMP sources through deep optical spectroscopy. We must reduce the number of unidentified sources at faint optical magnitudes ($r' > 22.5$). We expect that this optically faint population will include a significant number of the luminous ($\log L_X > 44$) type 2 QSOs that have not been detected in large numbers in the ChaMP. With ~ 20 $z > 4$ candidates based on optical colors, we may be able to significantly improve the statistics at these redshifts for which ChaMP has already found four to date.

REFERENCES

- Akiyama, M., Ueda, T., Ohta, K., Takahashi, T., Yamada, T. 2003, ApJS, 148, 275
- Alexander, D. M., et al. 2003, AJ, 126, 539
- Avni, Y., Bahcall, J. N. 1980, ApJ, 235, 694
- Barger, A.J. et al. 2003a, ApJ, 584L, 61
- Barger, A.J. et al. 2003b, AJ, 126, 632
- Barger, A. J., Cowie, L. L., Mushotzky, R. F., Yang, Y., Wang, W.-H., Steffen, A. T., Capak, P. 2005, AJ, 129, 578
- Boyle, B. J., Shanks, T., Peterson, B. A. 1988 MNRAS, 235, 935
- Brandt, W. N., Hasinger, G. 2005, ARA&A, 43, 827
- Cavaliere, A. & Vittorini, V. 2000, ApJ, 543, 599
- Cowie, L. L., Barger, A. J., Bautz, M. W., Brandt, W. N., & Garmire, G. P. 2003, ApJ, 584L, 57
- Croom, S. M., Smith, R. J., Boyle, B. J., Shanks, T., Miller, L., Outram, P. J., & Loaring, N. S. 2004, MNRAS, 349, 1397
- Croton, D.J. et al. 2005, astro-ph/0508046
- Di Matteo, T., Springel, V., Hernquist, L. 2005, Nature, 620, 604
- Fabian, A. C. 1999, MNRAS, 308, 39
- Fan, X. et al. 2001, AJ, 121, 54
- Fiore, F. et al. 2003, A&A, 409, 79
- Giacconi, R., et al. 2002, ApJS, 139, 369
- Green et al. 2004, ApJS, 150, 43
- Hasinger, G. et al. 2001, A&A, 365, 45

- Hasinger, G., Takamitsu, M., Schmidt, M. 2005, A&A, 441, 417
- Hao, L. et al. 2005, ApJ, 129, 1783
- Kim, D.-W. et al. 2004a, ApJS, 150, 19
- Kim, D.-W. et al. 2004b, AJ, 600, 59
- La Franca et al. 2005, astro-ph/0509081
- Lehmer, B. D. et al. 2005, ApJS, 161, 21
- Mainieri, V., Bergeron, J., Hasinger, G., Lehmann, I., Rosati, P., Schmidt, M., Szokoly, G., Della Ceca, R. 2002, A&A, 393, 425
- Marconi, A., Risaliti, G., Gilli, R., Hunt, L. K., Maiolino, R., Salvato, M. 2004, MNRAS, 351, 169
- Merloni, A. 2004, MNRAS, 353, 1035
- Miyaji, T., Hasinger, G., & Schmidt, M. 2000, A&A, 353, 25
- Moretti, A., Campana, S., Lazzati, D., & Tagliaferri, G. 2003, ApJ, 588, 696
- Nandra, K. et al. 2005, MNRAS, 356, 568
- Richards, G. T., et al. 2005, astro-ph/0504300
- Rosati, P. et al. 2002, ApJ, 566, 667
- Schmidt, M. 1968, ApJ, 151, 393
- Schmidt, M., Schneider, D. P., & Gunn, J. E. 1995, AJ, 110, 68
- Silverman, J. D. et al. 2005a, ApJ, 618, 123
- Silverman, J. D. et al. 2005b, ApJ, 624, 630
- Steffen, A. T., Barger, A. J., Capak, P., Cowie, L. L., Mushotzky, R. F., Yang, Y. 2004, AJ, 128, 1483
- Szokoly, G. P., et al. 2004, ApJS, 155, 271
- Tozzi, P. et al. 2001, ApJ, 562, 42
- Ueda, Y., Akiyama, M., Ohta, K., & Takamitsu, M. 2003, ApJ, 598, 886
- Wall, J. V., Jackson, C. A., Shaver, P. A., Hook, I. M., Kellermann, K. I. 2005, A&A, 434, 133
- Warren, S. J., Hewett, P. C., & Osmer, P. S. 1994, ApJ, 421, 412
- Wolf, C., Wisotzki, L., Borch, A., Dye, S., Kleinheinrich, M., & Meisenheimer, K. 2003, A&A, 408, 499
- Yang, Y., Mushotzky, R. F., Steffen, A. T., Barger, A. J., Cowie, L. L. 2004, AJ, 128, 1501
- Zheng, W. et al. 2004, ApJS, 155, 73

XMM-NEWTON OBSERVATIONS OF THE *LOCKMAN HOLE*: SPECTRA AND TIME VARIABILITY OF THE BRIGHTEST AGN

Mateos S.^{1,2}, Barcons X.², Carrera F.J.², Ceballos M.T.², Hasinger G.³, Lehmann I.³, Streblyanska A.³, and Fabian A.⁴

¹Department of Physics and Astronomy, Leicester University, Leicester LE1 7RH, UK

²Instituto de Física de Cantabria (CSIC-UC), 39005 Santander, Spain

³Max-Planck-Institut für Extraterrestrische Physik, Giessenbachstrasse, Garching D-85748, Germany.

⁴Institute of Astronomy, University of Cambridge, Madingley Road, Cambridge CB3 0HA, UK.

ABSTRACT

We discuss here the main results of a study of the X-ray spectral and variability properties of the 123 brightest objects detected with *XMM-Newton* in the *Lockman Hole* field. This is the deepest observation carried out so far with *XMM-Newton*, with more than 600 ksec of EPIC pn data. Thanks to the good signal to noise of the data (all spectra have more than 500 background subtracted counts) we have been able to put strong constraints on the properties of the X-ray emission of faint Active Galactic Nuclei and on their dependence on luminosity and redshift. To complement the X-ray spectral analysis we carried out a study of the X-ray variability of the same sample of objects on long time scales ranging from days to years.

Key words: X-rays: general, X-ray surveys, galaxies: active.

1. INTRODUCTION

Recent *Chandra* and *XMM-Newton* deep surveys have proven that the Cosmic X-ray background (XRB) at energies above ~ 0.2 keV is made up of the integrated emission of point sources, most being faint Active Galactic Nuclei (AGN). In order to gain insight into the nature and cosmic evolution of the population of AGN, spectral analyses of large samples of objects detected in medium and deep X-ray surveys are being conducted. However the majority of the sources detected in these observations are too faint to provide good spectral information and in many cases some assumptions need to be made prior to the analysis (frequently on the slope of the broad band continuum shape).

With the aim of constrain better the X-ray spectral and variability properties of faint AGN and their dependence

on luminosity and redshift we have carried out a detailed study of the X-ray emission properties of the brightest sources detected with *XMM-Newton* in the *Lockman Hole* field.

Throughout this paper we have adopted the *WMAP* derived cosmology with $H_0 = 70 \text{ km s}^{-1} \text{ Mpc}^{-1}$, $\Omega_M = 0.3$ and $\Omega_\Lambda = 0.7$.

2. THE X-RAY DATA

The *XMM-Newton* deep survey of the *Lockman Hole* is composed of 17 observations carried out from 2000 to 2002. In total we have more than 600 ksec of clean¹ pn data and more than 800 ksec of MOS1 and MOS2 data. A detailed description of how the source list of the total observation was built can be found in Mateos (2005). A total of 268 sources were detected by *XMM-Newton* in the *Lockman Hole*. From this sample we selected the 123 brightest objects (all spectra have more than 500 background subtracted counts) for our analysis. As we are primarily interested in studying the properties of AGN we excluded from the sample sources already identified as clusters of galaxies or stars. At the time of this analysis we had optical spectroscopic identifications available for 74 ($\sim 60\%$) objects, 46 being identified as type-1 AGN and 28 as type-2 AGN.

3. SPECTRAL ANALYSIS

We extracted spectral products, source and background spectra and the corresponding calibration matrices, for each individual observation. The data was then combined to obtain a MOS and pn time averaged spectrum for each

¹After removal of the time intervals affected by high flaring background.

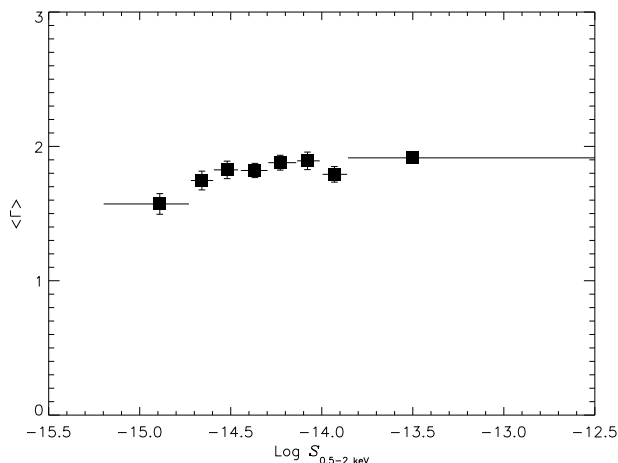


Figure 1. Dependence of $\langle\Gamma\rangle$ on 0.5-2 keV flux. For each source we used the values of Γ from its best fit model.

object. Due to the different instrumental responses of the detectors we did not combined MOS and pn data. Spectra were extracted in the energy interval from 0.2 to 12 keV where the *XMM-Newton* instruments are best calibrated. In order to use χ^2 minimisation to find the best fit model for each object we grouped the spectra with a minimum of 30 counts per bin.

We have obtained the best fit model for each source individually using the *xspec* 11.3.0 package. MOS and pn spectra were fitted simultaneously with the same model and spectral parameters. We used the F-test to measure the significance of detection of each individual component. We selected a confidence level threshold of 95% to accept an additional spectral component as being real. We started the spectral fitting using a model consisting of an absorbed power law, with an absorption component fixed to the Galactic column density in the direction of the *Lockman Hole*, $N_{\text{H}} = 5.7 \times 10^{19} \text{ cm}^{-2}$, and a second absorption component that was left free to vary. For sources with detected soft excess emission we fitted this component with a black body model. In some cases the black body model was not able to reproduce the spectral signatures of the soft excess emission. For these sources acceptable fits were obtained using a partial covering model. Signatures of $\text{FeK}\alpha$ emission were detected in eight sources. In all cases a Gaussian model provided an acceptable fit to the data.

In this proceeding we will show the properties of the broad band continuum shape and X-ray absorption of our sources. A more detailed description of the results of our spectral analysis can be found in Mateos (2005).

3.1. Broad band continuum shape

The mean spectral slope of our sources was found to be $\langle\Gamma\rangle = 1.87 \pm 0.02$. Using the values of Γ from the best fit model of each object we did not see any clear dependence of $\langle\Gamma\rangle$ on the 0.5-2 keV flux as it is shown in Figure 1. We

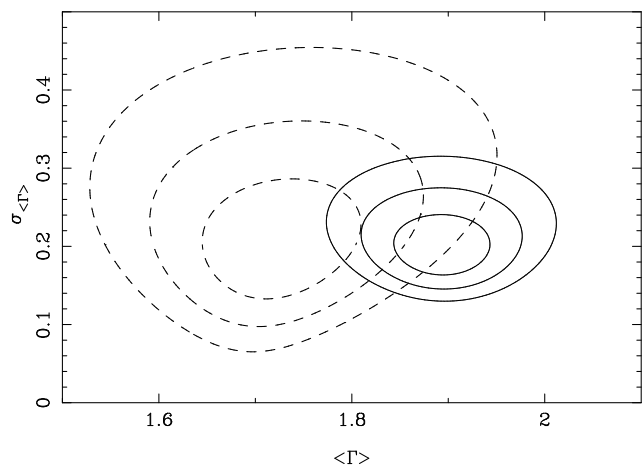


Figure 2. Confidence intervals for the mean spectral slope $\langle\Gamma\rangle$ and intrinsic dispersion $\sigma_{\langle\Gamma\rangle}$ for our samples of type-1 (solid lines) and type-2 (dashed lines) AGN from the maximum likelihood analysis. The three contours correspond to 1, 2 and 3σ for two interesting parameters (i.e. $\Delta\chi^2=2.3, 6.17$ and 11.8).

found the mean continuum shape to be $\langle\Gamma\rangle = 1.89 \pm 0.03$ for type-1 AGN and $\langle\Gamma\rangle = 1.71 \pm 0.03$ for type-2 AGN, although with a significant dispersion in the individual values in both samples of objects. Assuming a Gaussian distribution of spectral slopes we used the maximum likelihood method of Maccacaro (1988) to calculate the mean continuum shape and its intrinsic dispersion. The results of this analysis are shown in Table 1. In Figure 2 we show the maximum likelihood confidence intervals of $\langle\Gamma\rangle$ and $\sigma_{\langle\Gamma\rangle}$ for type-1 and type-2 AGN. Although our results suggest that type-2 AGN tend to have on average flatter spectral slopes than type-1 AGN we found the significance of this effect to be only of 1.62σ .

Table 1. Mean spectral photon index obtained with the Maximum Likelihood analysis and with the standard weighted mean. The spectral slopes from the sources' best fit model were used.

Sample	Maximum Likelihood		Weighted Mean
	$\langle\Gamma\rangle$	$\sigma_{\langle\Gamma\rangle}$	
Whole sample	$1.92^{0.03}_{0.18}$	$0.28^{0.04}_{0.13}$	1.87 ± 0.02
type - 1 AGN	$1.89^{0.06}_{0.05}$	$0.20^{0.04}_{0.04}$	1.89 ± 0.03
type - 2 AGN	$1.72^{0.10}_{0.08}$	$0.20^{0.10}_{0.07}$	1.71 ± 0.03

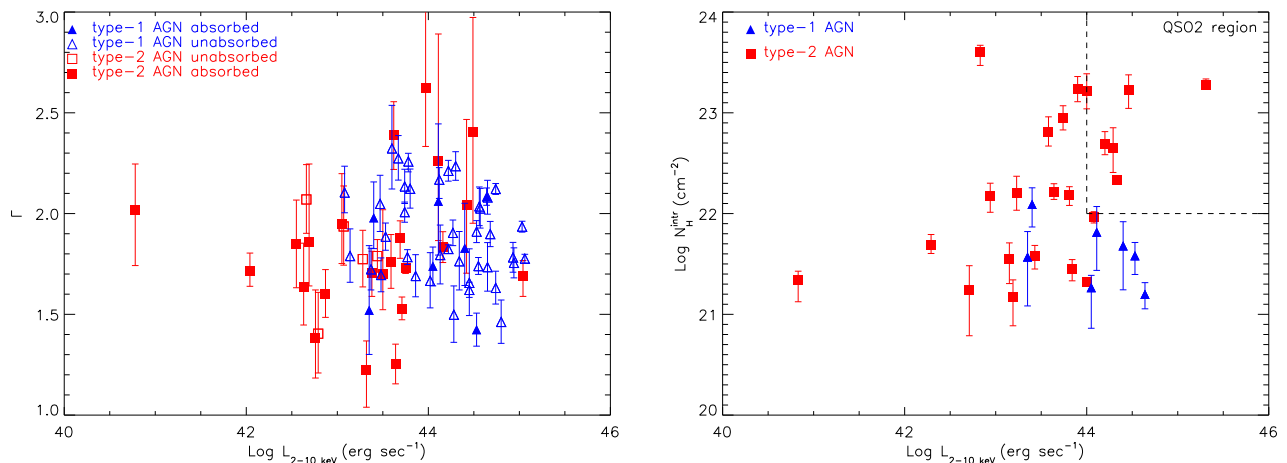


Figure 4. Dependence of Γ (left) and $N_{\text{H}}^{\text{intr}}$ (right) on 2-10 keV (rest-frame) luminosity. Error bars correspond to 90% confidence.

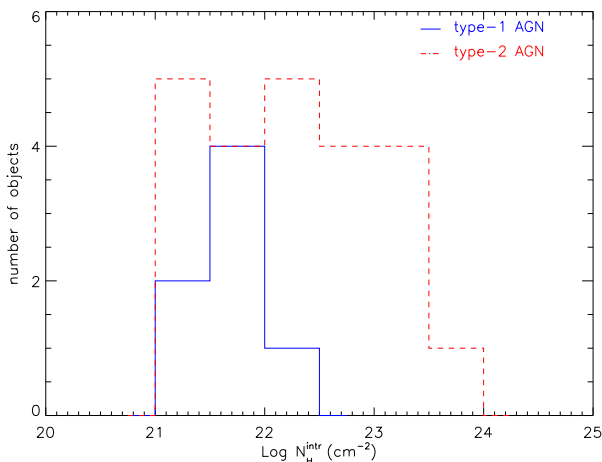


Figure 3. Distributions of intrinsic (rest-frame) absorbing column densities for type-1 and type-2 AGN.

3.2. X-ray absorption

We detected X-ray absorption (F-test $\geq 95\%$) in $\sim 38\%$ of our sources, including $\sim 10\%$ of type-1 AGN and $\sim 77\%$ of type-2 AGN². We found the fractions of absorbed sources among type-1 and type-2 AGN to be different with a significance of $\geq 99.99\%$. The distributions of measured intrinsic (rest-frame) column densities for absorbed type-1 and type-2 AGN are shown in Figure 3. The absorbing column densities for type-1 AGN were found to be in a narrow range from $10^{21} - 10^{22} \text{ cm}^{-2}$. The distribution of $N_{\text{H}}^{\text{intr}}$ for type-2 AGN covers a much broad range of values with a significant number of sources having $N_{\text{H}}^{\text{intr}} \geq 10^{23} \text{ cm}^{-2}$.

²The values for the fractions of absorbed sources have been corrected for the expected spurious detections.

3.3. Dependence of AGN X-ray properties on luminosity and redshift

In Figures 4 and 5 we show the dependence of the photon index and intrinsic absorption on 2-10 keV (rest-frame) luminosity and redshift for our samples of type-1 and type-2 AGN. We did not find a clear dependence of the X-ray spectral properties of our AGN on X-ray luminosity. A basic Spearman Rank correlation test of Γ and $N_{\text{H}}^{\text{intr}}$ versus redshift for type-1 AGN implies that there is not correlation between these parameters. This lack of correlation of Γ -redshift was also found for type-2 AGN. The observed deficit of high redshift AGN with low $N_{\text{H}}^{\text{intr}}$ is probably due to a selection effect, since it is easier to detect highly absorbed sources at high redshifts.

4. VARIABILITY ANALYSIS

The previous results were obtained by the analysis of the time averaged spectrum of each individual source. However we know AGN are strongly variable sources, showing their fastest variability in X-rays. X-ray variability studies are a good complement to spectral analyses as they can provide valuable information about the nature and structure of the innermost regions in AGN where the X-rays are emitted.

4.1. Flux variability

To study X-ray flux variability we built light curves for our sources using the 0.2-12 keV count rates detected on each individual observation. An example of a typical light curve is shown in Figure 6. For this analysis we have used only pn data because in general pn count rates are better constraint than MOS count rates. We have pn light curves available (with at least two points) for 120

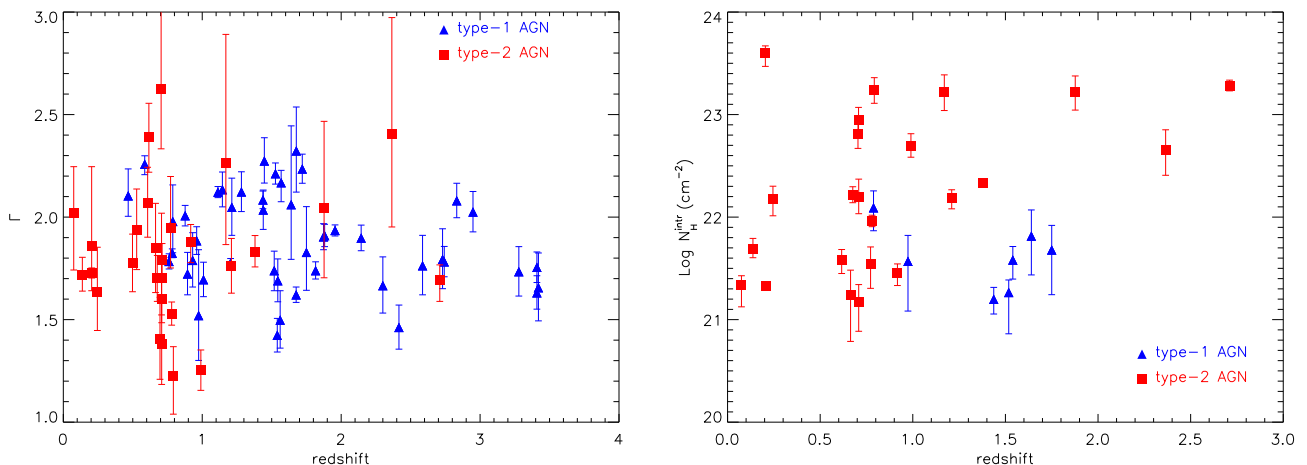


Figure 5. Dependence of Γ (left) and $N_{\text{H}}^{\text{intr}}$ (right) on redshift. Error bars correspond to 90% confidence.

out of the 123 objects in our sample including 45 type-1 AGN and 27 type-2 AGN. To search for sources with flux variability we have used the χ^2 test³, where χ^2 is defined as

$$\chi^2 = \sum_i \frac{(x_i - \langle x \rangle)^2}{\sigma_i^2} \quad (1)$$

x_i are the 0.2-12 keV count rates from each individual observation, N is the number of points in the light curve, $\langle x \rangle$ is the mean count rate and σ_i are the errors in the count rates x_i . We selected a 3σ confidence threshold for detection of variability. The results of the χ^2 test are summarised in Table 2, where the fractions of sources with detected variability have been corrected for the expected spurious detections. Flux variability was detected in $\sim 50\%$ of the sources in our sample. We compared the fractions of sources with detected flux variability among type-1 and type-2 AGN and we found the significance of them of being different of only 75%. The fraction of sources variable in flux for unidentified objects is significantly lower than for AGN. Most unidentified objects are among the faintest sources in our sample, and therefore their light curves have lower S/N which makes for difficult the detection of variability.

To quantify the amplitude of flux variability in our sources we have used the *excess variance*, σ_Q , that we have calculated using the method developed by Almaini (2000). This method is the most appropriate in the regime of gaussian statistics and for light curves with points having different measurement errors. The *excess variance* gives us the fraction of the total flux that is variable and therefore we can compare the values obtained for sources with different count rates. The distribution of measured values of σ_Q in shown in Figure 7 for the whole sample of sources (solid histogram) and for the objects with detected flux variability from the χ^2 test (filled histogram).

³We checked that using the count rates from the 0.2-12 keV energy band all sources have more than 10 counts (background subtracted) on each point of their light curves and therefore we can assume gaussian statistics during the analysis.

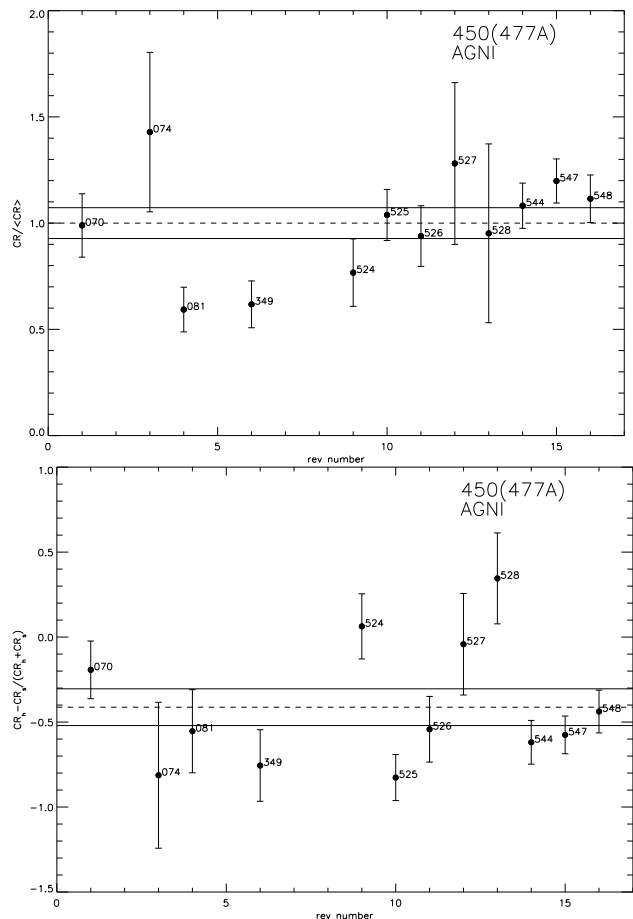


Figure 6. Typical light curves of a source with detected flux (top) and spectral variability (bottom). Each point represents the data from an individual observation and is labelled with the revolution number for that observation. The distribution of points is not uniform in time and can vary from days to years.

Table 2. Fractions of sources with detected flux and spectral variability from the χ^2 test.

Group (1)	N_{tot} (2)	n_{flux} (3)	$f_{\text{flux}}(\%)$ (4)	n_{sp} (5)	$f_{\text{sp}}(\%)$ (6)
All	120	62	51 ± 7	24	20 ± 6
type-1 AGN	45	31	68 ± 11	6	14 ± 8
type-2 AGN	27	13	48 ± 15	9	34 ± 14
Unidentified	48	18	37 ± 11	9	19 ± 9

Columns are as follows: (1) Group of sources; (2) Number of objects in the group; (3) Number of sources with detected flux variability (confidence $\geq 3\sigma$); (4) Fraction (corrected for spurious detections) of sources with detected flux variability; (5) Number of sources with detected spectral variability (confidence $\geq 3\sigma$); (6) Fraction (corrected for spurious detections) of sources with detected spectral variability; Errors are 90% intervals.

We have detect a broad range of flux variability amplitudes going from ~ 0.1 to ~ 0.65 . We see in Figure 7 that the efficiency of detection of flux variability depends strongly on the amplitude of the variability, specially for values of σ_Q lower than ~ 0.3 . The mean amplitude of flux variability (including objects with no detected variability from the χ^2 test) was found to be 0.22 for the whole sample of sources, 0.27 ± 0.02 for type-1 AGN and 0.21 ± 0.03 for type-2 AGN.

As it is shown in Figure 8 no dependence of the mean amplitude of flux variability on luminosity and redshift was seen for our identified sources.

4.2. Spectral variability

Most of the sources in our sample are too faint to conduct a detailed spectral analysis of their emission properties on each individual observation, as the uncertainties in the spectral parameters will be very large to detect small changes in the spectral shape. Therefore to search for spectral variability in our sources we have used a broad band hardness ratio HR, that we defined as

$$HR = \frac{CR_h - CR_s}{CR_h + CR_s} \quad (2)$$

where CR_h and CR_s are the 0.5-2 and 2-12 keV count rates of the sources from each observation. To search for sources with spectral variability we have compared the mean HR of each source to the ones measured for each individual observation using χ^2 test (as for flux variability). We detected spectral variability in $\sim 20\%$ of the objects in our sample including $\sim 14\%$ of type-1 AGN and $\sim 34\%$ of type-2 AGN. We found that the fractions of

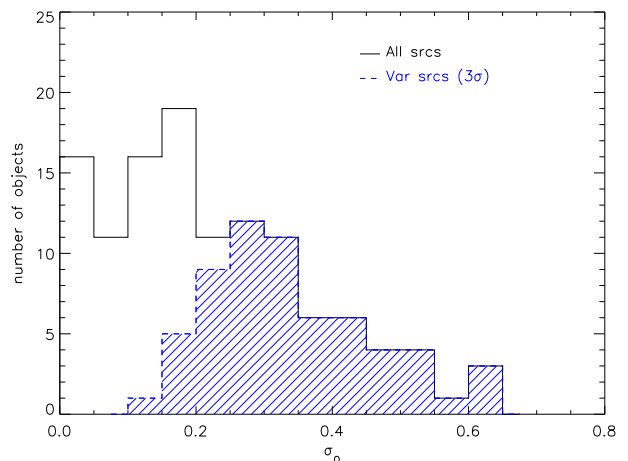


Figure 7. Distribution of measured amplitudes of flux variability for the whole sample of objects (solid histogram) and for the sources where we detected flux variability with the χ^2 test with a confidence level $\geq 3\sigma$.

objects with spectral variability among type-1 and type-2 AGN are different with a significance of 99%, i.e. spectral variability seems to be more common in type-2 AGN.

4.3. Fractions of variable sources

Our variability analysis has shown that $\sim 50\%$ of the sources in our sample are variable in flux and $\sim 20\%$ in spectral shape. We have studied whether the efficiency of detection of variability depends on the signal to noise of our data. In Figure 9 we show the fraction of sources with detected flux and spectral variability as a function of the mean 0.2-12 keV count rate (top) and as a function of the error in the mean HR (bottom). We see that the fractions of sources with detected spectral and flux variability strongly depend on the S/N of the data. Our results show that the fraction of sources in our sample with flux variability could be $\geq 80\%$ while the fraction of objects with spectral variability could be $\geq 50\%$.

5. DISCUSSION

We have investigated the X-ray spectral and variability properties of the 123 brightest sources detected with *XMM-Newton* in the *Lockman Hole* field. Using for each source the results from its best fit model we have been able to explain the observed hardening of the mean photon index with X-ray flux as an increase in X-ray absorption at faint fluxes. We found the mean 0.2-12 keV photon index to be ~ 1.9 for the whole sample of objects and for type-1 AGN, and ~ 1.7 for type-2 AGN. We found a scatter of best fit photon indices of ~ 0.28 for the whole sample of sources and of ~ 0.2 for the subsamples of type-1 and type-2 AGN. This scatter in Γ is intrinsic and not related to X-ray absorption. Significant X-ray absorption was detected in $\sim 37\%$ of the objects in our sample

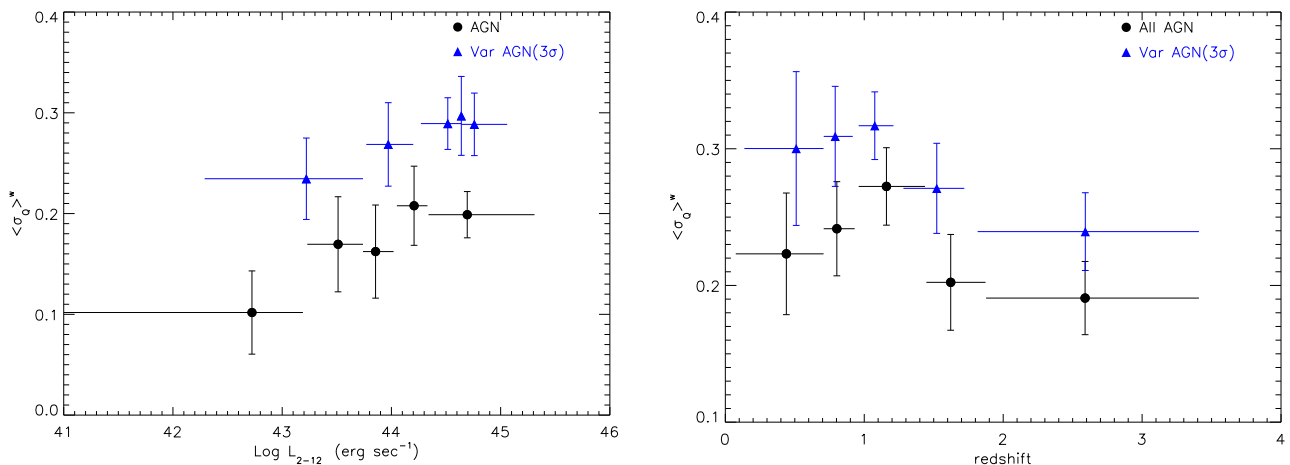


Figure 8. Dependence of the mean amplitude of flux variability (weighted mean) on 2-10 keV luminosity (left) and redshift (right) for all AGN and for the objects with detected flux variability from the χ^2 test.

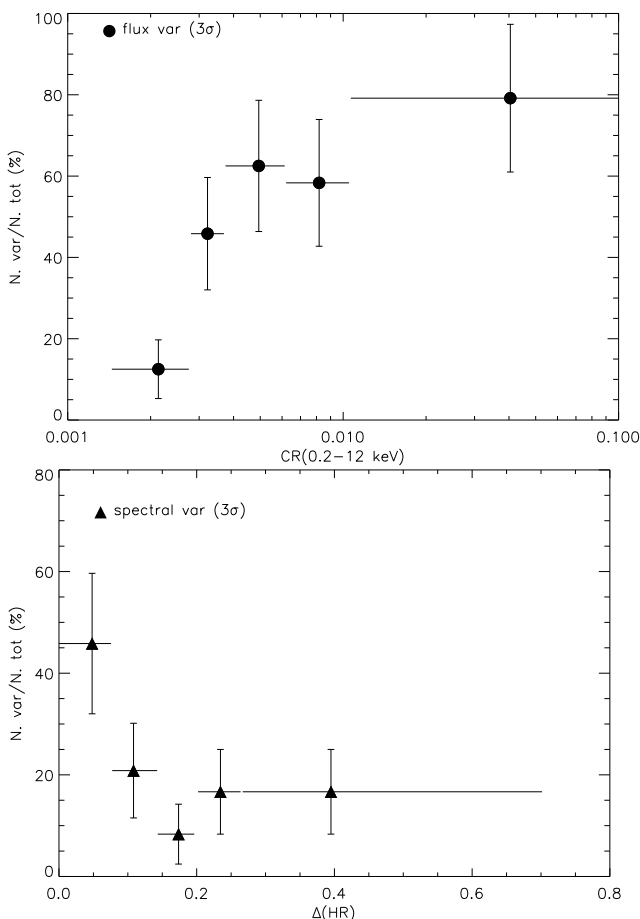


Figure 9. Top: Fraction of sources with detected flux variability as a function of the mean 0.2-12 keV count rate. Bottom: Fraction of sources with detected spectral variability as a function of the error in the mean HR.

including $\sim 10\%$ of type-1 AGN and $\sim 77\%$ of type-2 AGN. In terms of the standard unified model of AGN X-ray absorption and optical obscuration should be correlated. The results of our analysis show that this does not hold for a significant fraction of type-1 and type-2 AGN in our sample. We did not find evidences of spectral dependence of the AGN in our sample on X-ray luminosity and redshift.

A fraction of $\sim 50\%$ of the sources in our sample were found to vary with flux on long time scales. However using only the data with best signal to noise this fraction increases up to 80%, implying that flux variability is a common property of AGN. The mean amplitude of flux variability was found to be ~ 0.22 . The number of sources with detected spectral variability is $\sim 20\%$ but using only the data with best signal to noise the fraction increases up to $\sim 50\%$. Spectral variability seems to be less common than flux variability in our sources, however we need to note that spectral variability is more difficult to detect than flux variability. The fractions of sources with detected flux variability do not differ significantly among type-1 and type-2 AGN, however we found spectral variability to be more common in type-2 AGN with a significance of 99%. We did not find the variability properties of the AGN in our sample to depend on the luminosity or redshift of the objects.

REFERENCES

- Maccaro, T., Gioia, I. M., Wolter, A., et al. 1988, ApJ, 326, 680
- Almaini, O., Lawrence, A., Shanks, T., et al. 2000, MNRAS, 315, 325
- Mateos, S., Barcons, X., Carrera, F. J., et al. 2005, A&A accepted (astro-ph/0506718)

THE MOST OBSCURED AGN IN THE CHANDRA/SWIRE SURVEY IN THE LOCKMAN HOLE¹

M. Polletta¹, B.J. Wilkes², B. Siana³, C.J. Lonsdale^{1,4}, R. Kilgard², D.L. Shupe³, J. Surace³, H.E. Smith¹, and F. Owen⁵

¹Center for Astrophysics & Space Sciences, University of California, San Diego, La Jolla, CA 92093–0424, USA

²Harvard-Smithsonian Center for Astrophysics, 60 Garden Street, Cambridge, MA 02138, USA

³*Spitzer* Science Center, California Institute of Technology, 100-22, Pasadena, CA 91125, USA

⁴Infrared Processing & Analysis Center, California Institute of Technology, 100-22, Pasadena, CA 91125, USA

⁵National Radio Astronomy Observatory, P.O. Box O, Socorro, NM 87801, USA

ABSTRACT

The high sensitivity and spatial resolution of the *Spitzer* Space Telescope and of the *Chandra* X-ray Observatory are combined in the wide area (0.6 square degrees) *Chandra*/SWIRE survey in the Lockman Hole (10h45m, +59d) to investigate the properties of Active Galactic Nuclei (AGN). The X-ray and infrared data are used independently to select two samples of heavily obscured (Compton-thick) AGN candidates. The two selected samples contain 1) 5 X-ray sources with hard X-ray spectra and column densities $\geq 10^{24} \text{ cm}^{-2}$, and 2) 100 infrared sources with red and AGN-dominated infrared spectral energy distributions (SEDs). We estimate a surface density of at least 25 Compton-thick AGN per deg² detected in the IR in the *Chandra*/SWIRE field of which $\sim 40\%$ show distinct AGN signatures in their optical/near-infrared SEDs, the remaining sources being dominated by the host-galaxy emission. Only $\sim 33\%$ of all Compton-thick AGN are detected in the X-rays at our depth ($F(0.3\text{--}8 \text{ keV}) > 10^{-15} \text{ ergs cm}^{-2} \text{ s}^{-1}$). We report the discovery of the most luminous Compton-thick AGN at high- z currently known, SWIRE_J104409.95+585224.8 ($z=2.54$, $L_{\text{bol}} \simeq 10^{44} L_{\odot}$). The properties of this source are discussed in detail with an analysis of its spectrum, SED, luminosity and black-hole mass.

Key words: galaxies: active; quasars: individual (SWIRE_J104409.95+585224.8); infrared: galaxies; X-rays: galaxies.

¹Some of the data presented herein were obtained at the W.M. Keck Observatory, which is operated as a scientific partnership among the California Institute of Technology, the University of California and the National Aeronautics and Space Administration. The Observatory was made possible by the generous financial support of the W.M. Keck Foundation. Based on observations at the Kitt Peak National Observatory, National Optical Astronomy Observatory, which is operated by the Association of Universities for Research in Astronomy, Inc. under cooperative agreement with the National Science Foundation.

1. INTRODUCTION

The ubiquity of super-massive black-holes (SMBH) in galaxies, the correlation between their masses and the galaxy stellar mass (Ferrarese & Merrit, 2000) and the similarity between their space density (La Franca et al., 2005; Wolf, 2005) and the star-formation history of galaxies (Hartwick, 2004) strongly suggest that galaxy and AGN evolution are connected. Several current models attribute the link between the two processes to a merger event of large galaxies (Silk & Rees, 1998; Granato et al., 2004; Springel et al., 2005; Hopkins et al., 2005; Di Matteo et al., 2005; Cattaneo et al., 2005). During the merger, the SMBH and the host galaxy spheroid grow throughout vigorous star-formation episodes (Fabian, 1999). The merging system contains large amounts of gas and dust and the nucleus appears as heavily obscured. Both AGN and host-galaxy will experience major changes during this obscured phase in stellar mass, star-formation rate, and AGN luminosity. Many physical processes of this scenario remain to be explained and many predictions lack observational testing, especially for AGN in obscured phases which are hard to detect and identify.

The existence of a large population of obscured AGN is not only a model prediction, but it is also suggested by indirect observations like the shape of the X-ray background which is still largely unresolved at energies above 8 keV (Worsley et al., 2005) or the high fraction of obscured versus unobscured AGN (4:1) at low- z (Risaliti et al., 1999; Maiolino & Rieke, 1995; Piconcelli et al., 2003). Although these observations strongly suggest that obscured AGN are numerous and might even outnumber unobscured AGN, large and complete samples of obscured AGN are still missing.

In this work, we present a selection of the most obscured AGN, the so-called Compton-thick ($N_{\text{H}} \geq 10^{24} \text{ cm}^{-2}$) AGN and provide statistical constraints on their surface density. Our analysis is based on observations performed with the *Spitzer* Space Telescope as part

of the *Spitzer* Wide-Area Infrared Extragalactic Survey (SWIRE) (Lonsdale et al., 2003, 2004) and with the *Chandra* X-ray Observatory in a wide area (0.6 deg^2) in the Lockman Hole, the *Chandra*/SWIRE field.

2. OBSERVATIONS

The *Chandra*/SWIRE survey was performed in the northern part of the Lockman Hole which is the largest field (11 deg^2 centered at $10^{\text{h}}45^{\text{m}}, +58^\circ$) of the five observed by the SWIRE Project. The *Chandra*/SWIRE field (0.6 deg^2 centered at $10^{\text{h}}45^{\text{m}}, +59^\circ$) has been selected for deep multi-wavelength observations. The *Spitzer* data include images obtained with the Infrared Array Camera (IRAC) (Fazio et al., 2004) and the Multiband Imaging Photometer (MIPS) (Rieke et al., 2004). The 5σ limits of the *Spitzer* data are 5, 9, 43, 40 and $230 \mu\text{Jy}$ at 3.6, 4.5, 5.8, 8.0 and $24 \mu\text{m}$, respectively (Surace et al., 2005). The infrared (IR) catalog contains 41,262 sources. Optical imaging in U , g' , r' , and i' was obtained with the Mosaic Camera at the Kitt Peak National Observatory (KPNO) Mayall 4-mt Telescope. The 5σ limiting Vega magnitudes are 24.8 (U), 25.9 (g'), 25.2 (r'), and 24.4 (i'). The optical catalog contains 77,355 sources and $31'106$ sources are also detected in the IR. Thanks to the lack of nearby moderate brightness radio sources in the *Chandra*/SWIRE field, an extremely deep radio survey at 20 cm was also performed (Owen et al., in prep.). A 1.4 GHz radio map covering $40' \times 40'$ in the *Chandra*/SWIRE field, was obtained at the Very Large Array (VLA) with a root-mean-squared (rms) noise in the center of the radio image of $2.7 \mu\text{Jy}$. There are 2052 radio sources in the entire field and 2000 are also detected in the IR with IRAC. *Chandra* Advanced CCD Imaging Spectrometer (ACIS-I) (Weisskopf, O'dell, & van Speybroeck, 1996) observations were performed in a 3×3 raster for a total area of 0.6 deg^2 centered at $10^{\text{h}}46^{\text{m}}, +59^\circ 01'$. The exposure time for each pointing was ~ 70 ksecs, reaching a broad-band ($0.3\text{--}8 \text{ keV}$) flux limit of $\sim 10^{-15} \text{ ergs cm}^{-2} \text{ s}^{-1}$. A total of 792 sources were detected. An IR counterpart is matched to 774 (98%) sources, 640 (81%) of which are also detected in the optical images. The fraction of X-ray sources that are radio detected is 50% within $10'$ from the center of the radio field and 27% in the whole field.

3. COMPTON-THICK AGN SELECTION

In the following sections, we present two methods for selecting AGN with extreme column densities ($N_{\text{H}} \geq 10^{24} \text{ cm}^{-2}$), the so called Compton-thick AGN, one is based on the X-ray properties and the other on the optical-IR properties. Since the methods require redshifts, and spectroscopic redshifts are available for only a small fraction of sources, we supplement the spectroscopic redshifts with photometric redshifts. Photometric redshifts were derived using the code HYPERZ (Bolzonella et al.,

2000). We use a library 24 galaxy templates which includes 9 normal galaxy, 3 starburst, and 12 AGN templates and cover the wavelength range from 1000\AA to $500 \mu\text{m}$ (Polletta et al., in preparation).

3.1. X-ray selected obscured AGN

Obscured AGN were selected among the X-ray sources based on the estimated column density. This selection is biased against Compton-thick AGN in which the primary radiation is completely obscured at the observed energies ($< 8 \text{ keV}$) and only the warm scattered component is observed. This bias is less important for high- z sources where the observed radiation is emitted at higher energies in the source rest-frame. In order to derive the

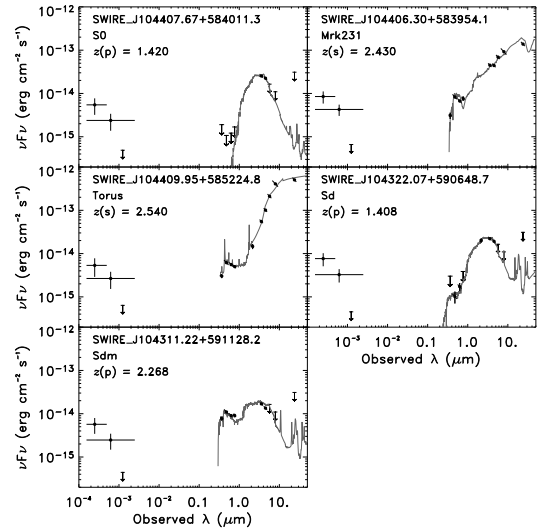


Figure 1. SED in $\nu F\nu$ of 5 X-ray selected Compton-thick AGN (full circles). The source names are reported on the upper-left corner of each panel. Downward arrows indicate upper limits at the completeness limit in the optical and at 5σ in the IR. The broad-, hard-, and soft-X-ray fluxes are shown as full circles. The X-ray fluxes are derived assuming an absorbed power-law model with photon index, Γ , equal to 1.7 and Galactic absorption, $N_{\text{H}}=6 \times 10^{19} \text{ cm}^{-2}$. A downward arrow at 1σ limit is used in the X-rays when the counts are less than 1σ . The best-fit template for each object is shown as a grey curve and the template name is reported in each panel. The spectroscopic (z_s) or photometric (z_p) redshift of each object is also reported.

amount of absorption, spectral files were created, for each source, using Sherpa (Freeman et al., 2001) simulations. In the simulations, we assumed an absorbed power-law model with a fixed photon-index $\Gamma = 1.7$, corresponding to the observed mean for AGN (Nandra & Pounds, 1994), and a range of column densities from $N_{\text{H}}=10^{19} \text{ cm}^{-2}$ to $10^{24.5} \text{ cm}^{-2}$. Each spectrum and the estimated local background as derived applying the Bayesian method (van Dyk et al., 2004), were used as

Table 1. Properties of X-ray selected Compton-thick AGN.

Source Name	F(24 μ m) (mJy)	F _{0.3–8keV} ^a	HR	z	N _H ^{obs,b}	N _H ^{rest,c}	Log(L) ^d
SWIREJ104407.67+584011.3	<0.23	24±10	1.00 ^{+0.0} _{-0.13}	1.42	20 ^{+∞} ₋₁₁	200 ^{+∞} ₋₁₀₉	45.5
SWIREJ104406.30+583954.1	1.099	43±12	0.61 ^{+0.21} _{-0.23}	2.43 ^e	4 ⁺³ ₋₁	99 ⁺⁷⁴ ₋₂₅	45.7
SWIREJ104409.95+585224.8	4.011	27±11	0.85 ^{+0.06} _{-0.39}	2.54 ^e	8 ⁺² ₋₅	214 ⁺⁵⁴ ₋₁₃₄	46.1
SWIREJ104322.07+590648.7	<0.23	33±11	1.00 ^{+0.0} _{-0.04}	1.41	30 ^{+∞} ₋₁₀	312 ^{+∞} ₋₁₀₄	45.6
SWIREJ104311.22+591128.2	<0.23	25±10	1.00 ^{+0.0} _{-0.15}	2.27	30 ⁺⁴⁰ ₋₂₃	863 ⁺¹¹⁵¹ ₋₆₆₂	45.9

^a X-ray flux in 10⁻¹⁶ ergs cm⁻² s⁻¹ derived assuming an absorbed power-law model with $\Gamma=1.7$ and Galactic absorption ($N_{\text{H}}=6\times 10^{19}$ cm⁻²). Uncertainties reflect only the statistical errors from the observed counts and do not include uncertainties in the spectral model. ^b N_{H} in the observer rest-frame in 10²² cm⁻². ^c Effective N_{H} in 10²² cm⁻². ^d Absorption-corrected rest-frame 0.3-8 keV luminosity in ergs s⁻¹. ^e Spectroscopic z .

input to MARX¹ to create a simulated data set. Hardness ratios (HR²) were calculated from the simulations of each source for all column densities. The column density, $N_{\text{H}}^{\text{obs}}$, of each source was determined by comparing the observed HR with the values derived from the simulation. The effective hydrogen column densities, $N_{\text{H}}^{\text{rest}}$, were then derived after correcting for the redshift of the sources as $N_{\text{H}}^{\text{rest}}=N_{\text{H}}^{\text{obs}} \times (1+z)^{2.6}$ (Longair, 1992). We found 5 X-ray sources with an intrinsic $N_{\text{H}}^{\text{rest}} \geq 10^{24}$ cm⁻². Source names, coordinates and X-ray properties (broad-band X-ray flux, HR, column density and absorption corrected broad band luminosity) are listed in Table 1, and their spectral energy distributions (SEDs) are shown in Fig. 1. Two sources show a distinct AGN signature in their optical/near-IR SED, while the other three sources are dominated by starlight in the optical and near-IR. The estimated column densities and absorption-corrected X-ray (0.3-8 keV) luminosities imply that these are all Compton-thick quasars.

3.2. IR-selected obscured AGN

In order to estimate the number of Compton-thick AGN detected in the IR, but missed in the X-rays at our limits, we developed a selection method for obscured AGN candidates that can be applied to the entire IR sample independently of the availability of X-ray data. The method is based on identifying sources with red and almost featureless near- and mid-IR SED which are evidence for thermal emission from high temperature dust heated by an AGN. Objects with this type of IR SEDs can be identified using the IRAC (3.6, 4.5, 5.8, and 8.0 μ m) colors (Lacy et al., 2004; Stern et al., 2004; Hatziminaoglou et al., 2005). Therefore, in order to select AGN among the IR population, we first selected all of the IR sources detected in at least 3 IR bands over the wavelength range 3.6-24 μ m. This selection reduced the IR sample from 41,262 to 4493 sources. Then we selected sources with a monotonically rising IR (2–24 μ m) SED, a spectral slope α_{IR} (defined as $F_{\nu} \propto \lambda^{\alpha_{\text{IR}}}$) larger than 1.0 and $\chi_{\nu}^2 < 13.3(\alpha_{\text{IR}} - 1) \leq$

20. This selection reduces the sample from 4493 to 248 sources. In order to remove likely unobscured AGN, we then selected all of the sources with optical-IR colors redder than those typical of unobscured quasars, specifically $F(3.6\mu\text{m})/F([g', r', i']) > [15, 13, 10]$. This final criterion is satisfied by 152 sources. The SEDs of these sources were fitted using HYPERZ. Only the sources that could not be fitted with a normal galaxy template at any redshift were kept for a final sample of 100 sources. The final sample of 100 objects was divided in five categories, from I to V. Four categories (I–IV) were defined based on their SED shapes and one category (V) was defined based on the low number (3) of detections in the IR. Category I (12 sources) is characterized by very red IR SEDs with a convex shape. Category II (46 sources) shows power-law like optical-IR SEDs, similar to Mrk 231 or slightly redder ($A_{\text{V}} < 1$). Similarly, category III (8 sources) is characterized by power-law like optical-IR SEDs, but not as red as Mrk231; a reddened QSO template ($A_{\text{V}} = 0.3\text{--}0.6$) provides a better fit. Category IV (21 sources) shows also signatures from an energy source other than the AGN. The SEDs are consistent with templates of composite sources with contributions from both star-formation processes and an AGN component. The SEDs of four sources representatives of categories I to IV are shown in Fig. 2. Category V (13 sources) contains objects with SEDs that are similar to those of the other categories, but they are fainter. A large fraction (44% in total and 91% within 12' from the center of the radio field) of the selected sources are also detected in the radio. This high radio detection rate supports the hypothesis that these sources are AGN. A small fraction, 32 sources, of the IR-selected obscured AGN candidates are also X-ray detected. Their X-ray spectra show a wide range of hardness ratios, from -0.87 to 0.85 , with a median value of -0.27 . Since we can not quantify the amount of obscuration in the non X-ray detected sources, we assume that the distribution of absorption in the entire IR-selected sample is similar to that observed in the X-ray detected sub-sample. Only two of these sources (2 out of 32 or 6%) are also present in the X-ray selected sample of Compton-thick AGN ($N_{\text{H}} > 10^{24}$ cm⁻²), SWIRE_J104409.95+585224.8 (SW104409 hereafter) and SWIRE_J104406.30+583954.1 and their Compton-thick nature is confirmed by their spectroscopic redshifts.

¹<http://space.mit.edu/CXC/MARX>

²HR=(H-S)/(H+S); where H represents the hard (2.5-8 keV) counts and S the soft (0.3-2.5 keV) counts.

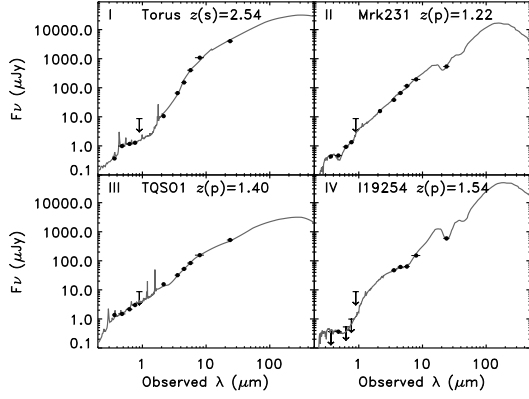


Figure 2. SEDs of 4 IR-selected obscured AGN candidates representing 4 different SED categories (I, II, III, IV) as noted on the upper-left corner (see text). Symbols as in Fig. 1.

With this assumption we estimate that 6 out of 100 IR-selected obscured AGN candidates are Compton-thick AGN. One of these two confirmed Compton-thick AGN is analyzed in detail in next section.

4. THE MOST LUMINOUS COMPTON-THICK QSO AT $z \geq 2$

Spectroscopic observations for SW104409 were obtained with the Low Resolution Imaging Spectrometer (LIRS) (Oke et al., 1995) on the Keck I telescope. The optical spectrum, shown in Fig. 3, is characterized by a blue continuum and narrow emission lines ($\text{FWHM} < 1400 \text{ km s}^{-1}$). A broad, but faint, blue-shifted component is observed in the CIV $\lambda 1549$ and NV $\lambda 1240$ emission lines. The estimated mean redshift is 2.54 ± 0.02 . The SED of SW104409, shown in Fig. 4, is characterized by a rapid rise at longer wavelengths with an observed $r' - K_s = 4.13$ (Vega), fitting the conventional definition of extremely red object (ERO) (Elston et al., 1988). The blue optical continuum and broad line components observed in the optical and the red near-IR SED can be explained by a scenario in which the AGN emission is reddened by dust in the near-IR and completely suppressed at the observed optical wavelengths (ultraviolet in the rest-frame) and the emerging optical emission is due to scattered light. This scenario is represented in Fig. 4 where the SED of SW104409 is compared to the SED of an unobscured QSO template in three cases: 1) normalized at the observed $24 \mu\text{m}$ flux of SW104409 to represent the intrinsic, before absorption, emission of SW104409 (dotted-dashed curve); 2) scaled to match the observed optical data, to represent the scattered component (dashed curve), which corresponds to 0.6% of the intrinsic emission, and 3) reddened by an extinction $A_V = 4 \text{ mag}$ ($E(B-V) \simeq 1$) (dotted curve). The luminosity as a function of wavelength of SW104409 is shown in Fig. 5. The luminosity distribution of an unob-

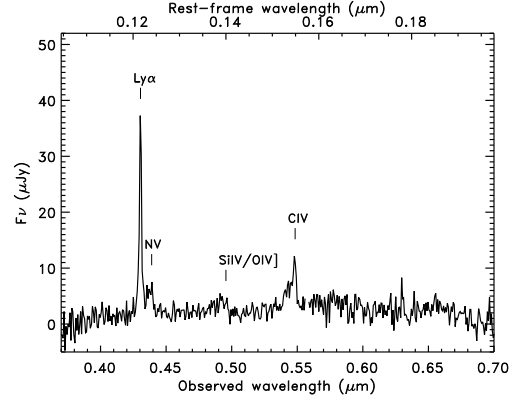


Figure 3. Optical spectrum of SW104409 obtained with the Keck I telescope. Detected emission lines are labeled.

scured QSO template (Elvis et al., 1994) normalized to the mid-IR flux of SW104409 is also shown for comparison. The template is also shown after applying enough extinction A_V to reproduce the red SEDs of SW104409. The integrated optical-IR (0.03–1000 μm) luminosity of SW104409 is $3.6 \times 10^{47} \text{ ergs s}^{-1}$ ($= 9.5 \times 10^{13} L_\odot$) as derived assuming the model shown in Fig. 4. SW104409 is a hyper-luminous IR galaxy (HYLIRG) (Sanders et al., 1996). The bolometric luminosity, derived by adding the absorption-corrected X-ray luminosity (see Table 1), the radio luminosity ($7.9 \times 10^{40} \text{ ergs s}^{-1}$) and the optical-IR luminosity is $3.7 \times 10^{47} \text{ ergs s}^{-1}$. Assuming that the AGN is accreting at the Eddington limit ($L_{bol} = L_{Edd}$), the estimated black-hole mass for SW104409 is $\simeq 2.8 \times 10^9 M_\odot$, very similar to the highest measured values in the local Universe, i.e. M87 (Ford et al., 1994) and Cyg A (Tadhunter et al., 2003) ($M_{BH} \simeq 3 \times 10^9 M_\odot$). Note that if the source was accreting below the Eddington limit, the implied black hole mass would be higher.

4.1. Comparison with Compton-thick AGN at $z \geq 2$

Very few high redshift Compton-thick AGN are currently known, including 4 sub-millimeter-selected X-ray sources at $z=2-2.5$ (Alexander et al., 2005a,b) and 3 X-ray-selected type 2 quasars, CXO-52 ($z=3.288$) (Stern et al., 2002), CDFS-202 ($z=3.700$) (Norman et al., 2001), and CDFS-263 ($z=3.660$) (Mainieri et al., 2005), the latter also being detected in the sub-mm. The sub-mm detected sources show starburst emission in their optical spectra and IR SEDs (Chapman et al., 2005; Borys et al., 2005). The AGN bolometric luminosities, usually only a small fraction of the bolometric luminosity in the sub-set of sub-mm selected AGN, range from 8.4 to $200 \times 10^{44} \text{ erg s}^{-1}$, and the derived black-hole masses range from 0.6 to $11 \times 10^7 M_\odot$. The highest luminosity and SMBH mass values belong to the X-ray-selected objects CDFS-202 and CXO-52 which are also optical narrow-line objects, as SW104409. This handful of high- z Compton thick AGN suggests that they represent an

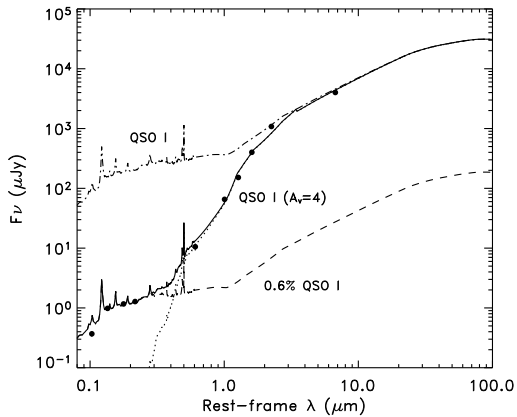


Figure 4. Observed SED of SW104409 (black circles) compared to an unobscured QSO template: 1) normalized to the mid-IR flux of SW104409 (dashed-dotted curve), 2) scaled to match the optical flux of SW104409 (dashed line), and 3) extinguished by $A_V=4$ to fit the IR data points (dotted curve). The solid curve corresponds to the sum of the extinguished (3) and the scattered components (2).

heterogeneous class with a broad range in luminosity and SMBH masses. The observed differences could be due to a different history or environment, to different evolutionary stages during the AGN obscured phase or to orientation effects.

5. SURFACE DENSITY OF COMPTON-THICK AGN

The two selection methods described in Section 3 were defined to select two samples of obscured AGN based on their X-ray and optical-IR properties, respectively. The X-ray selected sample is biased against Compton-thick AGN whose primary X-ray radiation is completely absorbed in the observed energy range, i.e. sources at low- z or with column densities $\geq 10^{25} \text{ cm}^{-2}$, and against sources that are fainter than $10^{-15} \text{ ergs cm}^{-2} \text{ s}^{-1}$ at 0.3–8 keV. The IR-selected sample is biased against AGN that are too faint to be detected in 3 IR bands at our sensitivity limits or whose host galaxy is brighter than the AGN in the optical-IR wavelength range. Since our selection is far from complete, we can only estimate a lower limit to the number of Compton-thick AGN IR detected in the *Chandra*/SWIRE field.

In Section 3.2, we estimate that about 6 sources (6% of 100 sources) among the IR-selected obscured AGN candidates are Compton-thick AGN. Since only two out of five X-ray selected Compton-thick AGN are also selected by the IR-selected criteria, we assume that our IR selection identifies only 40% (2 out of 5) of all Compton-thick AGN in the field. Thus, the estimated total number of Compton-thick AGN in the field is about 15 ($\approx 6/0.4$) sources or 25 per deg^2 . The estimated number of sources should be considered a lower limit to the total number of

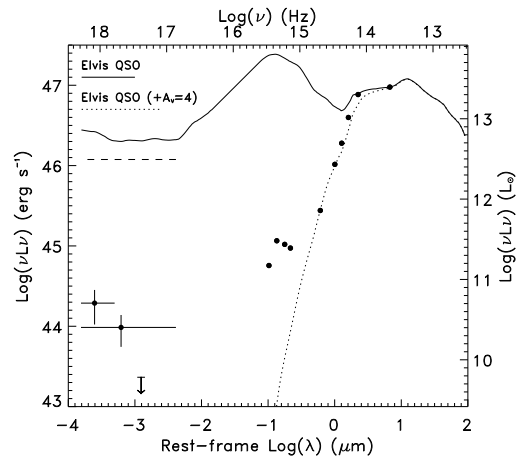


Figure 5. SED in νL_ν of SW104409 (black full circles) compared to an unobscured QSO template (Elvis et al., 1994) normalized at $24\mu\text{m}$ in two cases: 1) with no additional extinction (red solid curve) and 2) with 4.0 mag additional extinction (blue dotted curve). The dashed line corresponds to the absorption-corrected broad band X-ray luminosity.

Compton-thick AGN detected in the IR at our sensitivity limits in the *Chandra*/SWIRE field. Due to the lack of X-ray data for most of the sources, the identification of these 15 Compton-thick AGN is not possible because of lack of constraints on their column densities. The only exceptions are the 5 X-ray selected Compton-thick AGN presented in Section 3.1. The fraction of Compton-thick AGN identified in the X-ray at our depth ($F(0.3\text{--}8 \text{ keV}) \geq 10^{-15} \text{ ergs cm}^{-2} \text{ s}^{-1}$) is 33% (5 out of 15). This fraction is consistent with the 30% value estimated by Treister et al. (2004) of all Compton-thick AGN detected at the X-ray limit of the *Chandra* deep surveys.

6. SUMMARY

Using the optical/IR/X-ray dataset in the *Chandra*/SWIRE field (0.6 deg^2 in the Lockman Hole), we conducted a search for Compton-thick AGN. Two samples of Compton-thick AGN candidates were independently selected based on their X-ray spectral properties and optical-IR SED. By comparing the properties of the two samples and the fraction of sources selected in both samples, we derive a lower limit to the surface density of Compton-thick AGN detected in the IR to our survey limit of 25 deg^{-2} . We estimate that only 40% of this population shows distinct AGN signatures in their optical-IR SEDs, the rest being dominated by the host-galaxy emission and only 33% of them are identified in the X-ray down to $10^{-15} \text{ ergs cm}^{-2} \text{ s}^{-1}$ broad-band flux limit.

Optical spectroscopy of one candidate, SW104409, confirmed that it is the most luminous Compton-thick QSO at $z > 2$ currently known. The source is characterized by extreme properties, a very red optical-IR spectrum

and $\sim 10^{14} L_{\odot}$ bolometric luminosity. Such a rare object could be found thanks to the large volumes and the depth of the observations in the SWIRE/*Chandra* field ($\sim 0.6 \text{ deg}^2$).

ACKNOWLEDGMENTS

This work is based on observations made with the *Spitzer Space Telescope*, which is operated by the Jet Propulsion Laboratory, California Institute of Technology under NASA contract 1407. Support for this work, part of the *Spitzer Space Telescope* Legacy Science Program, was provided by NASA through an award issued by the Jet Propulsion Laboratory, California Institute of Technology under NASA contract 1407. MP, BS, BW and RK are grateful for the financial support of NASA grant G04-5158A (*Chandra*). BW is grateful for the financial support of NASA contract NAS8-39073 (*Chandra* X-ray Center). Based on observations obtained at the Hale Telescope, Palomar Observatory as part of a continuing collaboration between the California Institute of Technology, NASA/JPL, and Cornell University.

REFERENCES

- Alexander, D. M., Bauer, F. E., Chapman et al. 2005a, *ApJ*, 632, 736
- Alexander, D. M., Smail, I., Bauer, F. E. et al. 2005b, *Nature*, 434, 738
- Bolzonella M., Miralles J.-M. & Pelló R. 2000, *A&A*, 363, 476
- Borys, C., Smail, I., Chapman, S. C. et al. 2005, *ApJ* accepted (astro-ph/0507610)
- Cattaneo, A., Blaizot, J., Devriendt, J. & Guiderdoni, B. 2005, *MNRAS*, 359, 1237
- Chapman, S. C., Blain, A. W., Smail, I., & Ivison, R. J. 2005, *ApJ*, 622, 772
- Di Matteo, T., Springel, V., & Hernquist, L. 2005, *Nature*, 433, 604
- Elston, R., Rieke, G. H. and Rieke, M. J. 1988, *ApJ*, 331, 77
- Elvis, M., Wilkes, B. J., McDowell, J. C. et al. 1994, *ApJS*, 95, 1
- Fabian, A. C. 1999, *MNRAS*, 308, L39
- Fazio, G. G., et al. 2004, *ApJS*, 154, 10
- Ferrarese, L., & Merrit, D. 2000, *ApJ*, 539, L9
- Ford, H.C. et al. 2004, 1994, *ApJ*, 435, L27
- Freeman, P. E., Doe, S., Siemiginowska, A. 2001, *SPIE Proceedings*, 4477, 76
- Granato, G., De Zotti, G., Silva, L. et al. 2004, *ApJ*, 600, 580
- Hartwick, F.D.A. 2004, *ApJ*, 603, 108
- Hatziminaoglou, E., Perez-Fournon, I., Polletta M. et al. 2005, *AJ*, 129, 1198
- Hopkins, P. F., Hernquist, L., Martini, P. et al. 2005, *ApJ*, 625, 71
- La Franca, F. et al. 2005, *ApJ*, 635
- Lacy, M. et al. 2004, *ApJS*, 154, 166
- Leighly, K.M. & Moore, J.R. 2004, *ApJ*, 611, 107
- Longair, M.S. 1992, *High Energy Astrophysics*, Cambridge, UK: Cambridge University Press
- Lonsdale, C. J. et al. 2003, *PASP*, 115, 897
- Lonsdale, C. J., Polletta, M., Surace, J.D. et al. 2004, *ApJS*, 154, 54
- Mainieri, V. et al. 2005, *MNRAS*, 356, 1571
- Maiolino, R., Rieke, G. H., 1995, *ApJ*, 454, 95
- Morrison, R., & McCammon, D. 1983, *ApJ*, 270, 119
- Nandra, K., & Pounds, K. A. 1994, *MNRAS*, 268, 405
- Norman, C. et al. 2002, *ApJ*, 571, 218
- Oke, J. B., Cohen, J. G., Carr, M. et al. 1995, *PASP*, 107, 375
- Piconcelli, E., Cappi, M., et al., 2003, *A&A*, 412, 689
- Rieke, G. et al. 2004, *ApJS*, 154,
- Risaliti, G., Maiolino, R., & Salvati, M. 1999, *ApJ*, 522, 157
- Sanders, D. B., & Mirabel, I. F. 1996, *ARA&A*, 34, 749
- Silk, J. & Rees, M. J. 1998, *A&A*, 224, L21
- Springel, V., Di Matteo, T., & Hernquist, L. 2005, *MNRAS*, 361, 776
- Stern, D. et al. 2002, *ApJ*, 568, 71
- Stern, D. et al. 2005, *ApJ*, 631, 163
- Surace, J. A. et al. 2005, SWIRE Data Delivery Document II, *Spitzer* Science Center, Caltech
- Tadhunter, C., Marconi, A., Axon, D. et al. 2003, *MNRAS*, 342, 861
- Treister, E., Urry, C.M., et al., 2004, *ApJ*, 616, 123
- van Dyk, D. A. et al. 2004, *HEAD*, 8, 1627
- Weisskopf, M. C., O'dell, S. L., & van Speybroeck, L. P. 1996, *SPIE*, 2805, 2
- Wolf, C. 2005, *MemSAI*, 76, 21
- Worsley, M. A., Fabian, A. C., Bauer, F. E. et al. 2005, *MNRAS*, 357, 1281

THE EVOLVING OBSCURED AGN POPULATION AND THE COSMIC X-RAY BACKGROUND

R. Gilli¹, A. Comastri¹, and G. Hasinger²

¹INAF - Osservatorio Astronomico di Bologna, via Ranzani 1, 40127, Bologna, Italy

²Max-Planck-Institut für extraterrestrische Physik, Postf. 1312, 85741 Garching, Germany

ABSTRACT

We present a new modeling of the cosmic X-ray background (XRB) based on the most up-to-date AGN X-ray luminosity functions (XLF) and evolution. The most recent results from the soft (0.5-2 keV) and hard (2-10 keV) X-ray surveys are used to constrain at best the contribution of Compton-thin AGN to the XRB. In particular, the ratio between moderately obscured AGN (Compton-thin) and unobscured AGN is estimated directly by comparing the soft and hard XLF. This comparison suggests that the fraction of obscured AGN decreases with intrinsic luminosity. The model is in agreement with the soft and hard AGN counts over about 6 dex in flux. A large population of heavily obscured -Compton thick- AGN is added to fit the XRB spectrum above 10 keV. Remarkably, the fraction of Compton thick AGN observed in the Chandra Deep Field South is in excellent agreement with that predicted by the model.

Key words: galaxies:active - X-rays:general.

1. INTRODUCTION

The deepest X-ray surveys in the Lockman Hole (Hasinger 2004), Chandra Deep Field South (Giacconi et al. 2002) and Chandra Deep Field North (Alexander et al. 2003) have shown that most of the cosmic X-ray background below 10 keV is resolved into discrete sources (e.g. Worsley et al. 2005), the vast majority of which have been identified as active galactic nuclei (e.g. Szokoly et al. 2003, Barger et al. 2003). The combination of deep with shallower surveys has allowed to construct the AGN X-ray luminosity function both in the soft 0.5-2 keV band (Hasinger et al. 2005) and in the hard 2-10 keV band (Ueda et al. 2003, La Franca et al. 2005) and map the evolution of X-ray selected AGN up to redshifts of $z \sim 5$. Although X-ray observations are less biased towards obscured AGN, sensitive imaging survey can be performed at present only at energies below 10 keV. Therefore, they are expected to severely undersample the population of extremely obscured AGN with col-

umn densities above $\log N_H = 24$ (i.e. Compton-thick sources) which, at least in the local Universe, are found to be as numerous as moderately obscured AGN (Risaliti et al. 1999; Guainazzi et al. 2005), and are expected to provide a significant contribution to the 30 keV peak in the XRB spectrum (Comastri et al. 1995; Gilli et al. 2001).

2. THE MODEL

In our modeling we tightly constrain the properties of Compton-thin AGN, for which a large body of observational data (e.g. source counts, luminosity functions and redshift distributions) are available. Once the population of Compton-thin AGN is fully characterized, we compute their contribution to the XRB spectrum and add as many Compton thick AGN as needed to fit the XRB spectrum above 10 keV, in particular the XRB bump at 30 keV. We remark that at $E < 10$ keV different instruments have measured different XRB intensities, with variations as large as 40% (the lower and higher value being measured by HEAO-1 and BeppoSAX, respectively), while in the energy range 10-300 keV the HEAO-1 measurement is still the only available one (see Gilli 2004 and Revnivtsev et al. 2005 for recent discussions). Since the discrepancies in the XRB measurements are not fully understood, we will not adopt the XRB below 10 keV as a primary constraint. Rather we rely on what we believe to be more robust observational data such as the 0.5-2 keV and 2-10 keV $\log N$ - $\log S$ and luminosity functions and verify *a posteriori* the resulting XRB spectrum.

More specifically the adopted strategy is as follows:

we assume that surveys in the 0.5-2 keV band are essentially tracing the population of unobscured ($\log N_H < 21$) AGN, while surveys in the 2-10 keV band are tracing the population of unobscured plus Compton thin ($\log N_H < 24$) AGN. Therefore the moderately obscured AGN population can be reasonably well estimated as the difference between the hard (total) and soft (unobscured) XLF.

It is well known (e.g. Comastri et al. 1995) that the

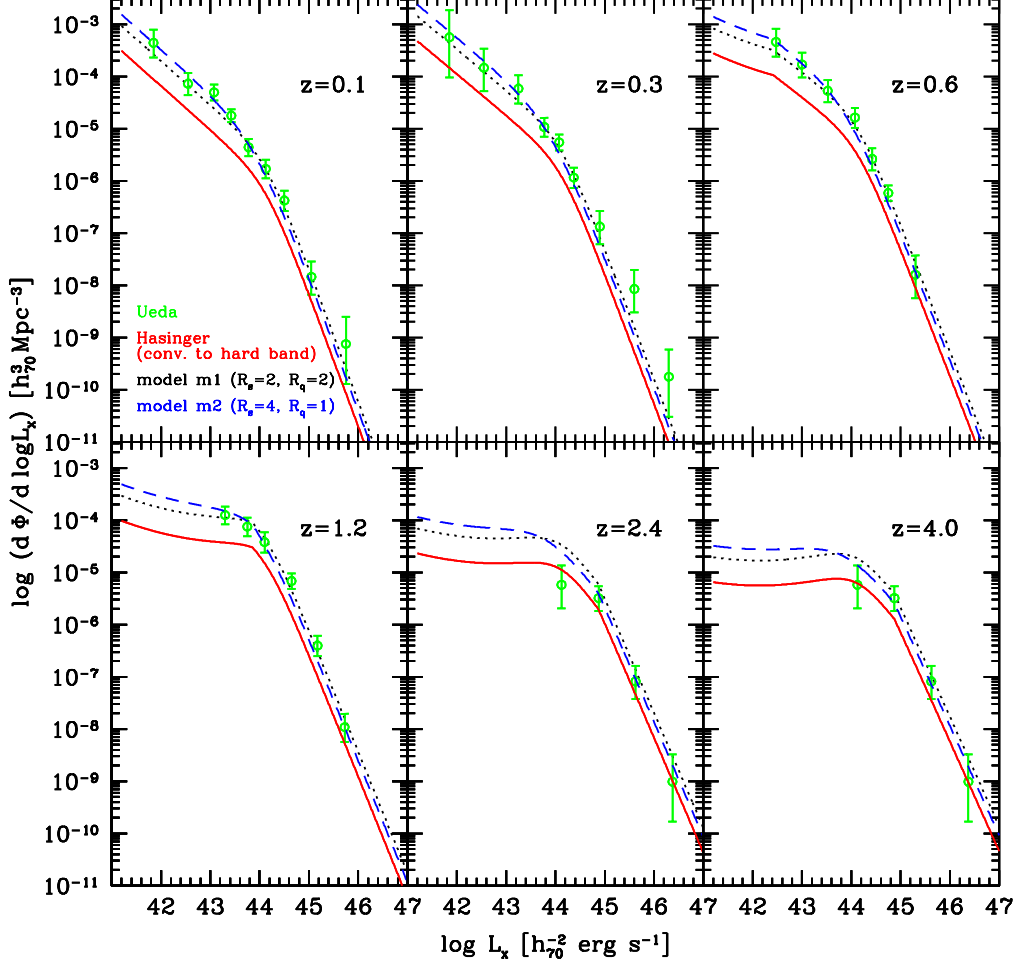


Figure 1. The Ueda et al. (2003) intrinsic hard XLF for the total Compton-thin AGN population (datapoints) compared with models m1 (dotted line) and m2 (dashed line). The soft XLF by Hasinger et al. (2005) converted to the hard band is also shown (solid line).

source counts in the hard X-ray band cannot be matched by simply converting the soft counts to the hard band assuming a standard unabsorbed AGN spectrum (e.g. a powerlaw with photon index $\Gamma = 1.9$). Similarly (Fig. 1), converting the soft XLF by Hasinger et al. (2005) to the hard band (assuming $\Gamma = 1.9$) is not sufficient to reproduce the total hard XLF, so obscured AGN have to be added.

We introduce the ratio R between obscured Compton-thin AGN and unobscured AGN (i.e. the number ratio between sources with $21 < \log N_H < 24$ and with $\log N_H < 21$) defined as follows:

$$R = R_S e^{-L/L_s} + R_Q (1 - e^{-L/L_s}), \quad (1)$$

where R_S is the ratio in the Seyfert (low-) luminosity regime and R_Q is the ratio in the QSO (high-) luminosity

regime, and L_s is the 0.5-2 keV characteristic luminosity dividing the two regimes (we fixed $\log L_s = 43.5$). The total AGN hard XLF is simply obtained by converting the soft (unobscured) XLF to the hard band and then multiplying it by $(1+R)$.

We considered two hypotheses: first (model m1) we assumed a ratio independent of luminosity where $R = R_Q = R_S = 2$; second (model m2), we assumed $R_S = 4$ and $R_Q = 1$ to account for a decline in the obscured AGN fraction with luminosity as suggested by several observational results (e.g. Ueda et al. 2003, La Franca et al. 2005).

As shown in Fig. 1, both models match the hard XLF by Ueda et al. (2003), however model m2 seems to provide a better description of the data than model m1. The recent hard XLF estimated by La Franca et al. (2005) lends further support to such a possibility (see Fig. 2). Therefore

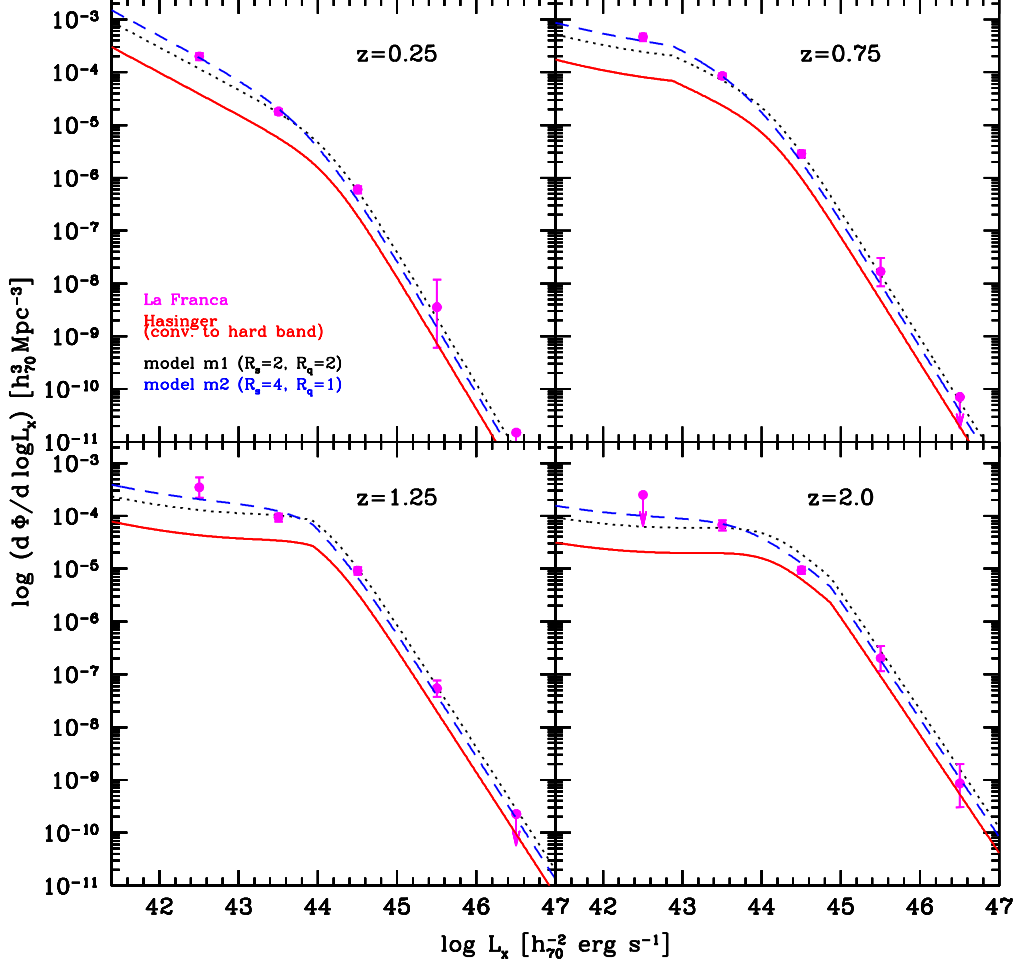


Figure 2. Same as the previous Figure but considering the hard XLF data of La Franca et al. (2005).

model m2 will be considered as our baseline model in the following.

It is worth noting that the comparison between the soft and hard XLF allows to constrain the total number of obscured Compton-thin AGN with no assumptions on their column density distribution. The latter is estimated by considering the soft and hard cumulative number counts as explained below. We divided Compton-thin sources into three absorption bins centered at $\log N_H = 21.5, 22.5, 23.5$. Following previous studies (Comastri et al. 1995, Risaliti et al. 1999, Gilli et al. 2001), the number of sources in each bin is chosen to increase with obscuration from $\log N_H = 21.5$ to $\log N_H = 23.5$ in order to reproduce the AGN counts in the soft and hard band over about 6 orders of magnitude in flux (Fig.3 and 4, respectively). A flat N_H distribution overpredicts the soft X-ray counts at faint fluxes and appears to be disfavored.

At this stage we believe that the population of moderately obscured sources is well constrained and their contribu-

tion to the XRB spectrum is computed (Fig. 5). A cut off powerlaw with photon index $\Gamma = 1.9$ and e-folding energy $E_c = 320 \text{ keV}$ is assumed as an input template for unabsorbed AGN. Absorption by different column densities is then introduced to model the spectra of obscured sources. A Compton reflection component is also added to the spectrum of AGN in the Seyfert luminosity regime, with a different normalization for obscured and unobscured sources (see Comastri et al. 1995).

The integrated emission of this population is found to explain most of the XRB below 10 keV as measured by HEAO-1 (see Fig. 5), but, as expected, fails to reproduce the 30 keV bump, calling for an additional population of Compton-thick sources. In our modeling these were divided into two, equally populated, absorption bins with $\log N_H = 24.5$ and $\log N_H > 25$, where distinct spectral templates have been considered according to the different physical scenarios: in the first case the direct, transmitted emission is still the main component above $\sim 10 \text{ keV}$, while at lower energies, where this is heavily absorbed,

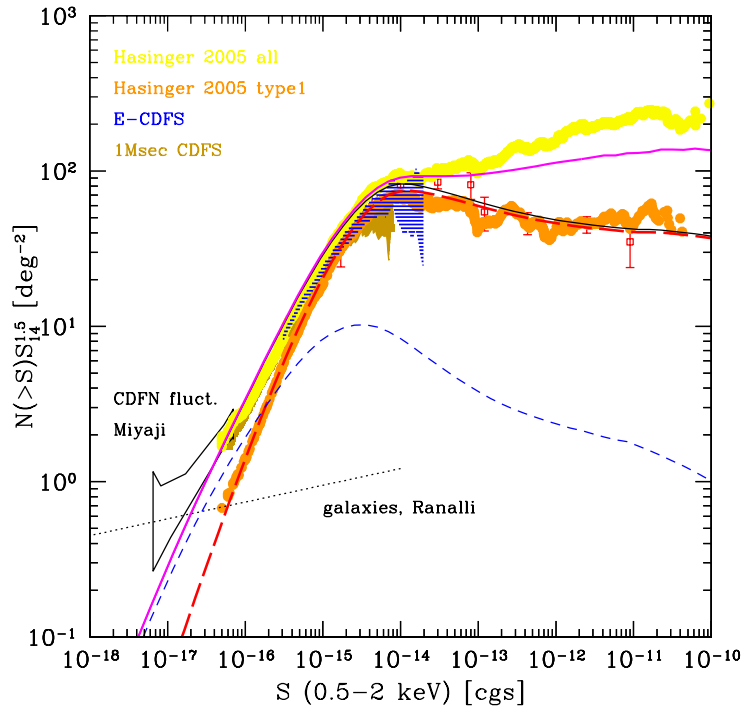


Figure 3. Cumulative soft AGN counts normalized to an Euclidean Universe. Datapoints are explained on the top left. The model curves for unabsorbed AGN, absorbed AGN, total AGN, and total AGN + clusters are shown respectively with the following line styles: red long-dashed, blue short-dashed, solid black, solid magenta. At bright fluxes the data are not cleaned by Galactic sources, thus producing an apparent discrepancy wrt the total model prediction.

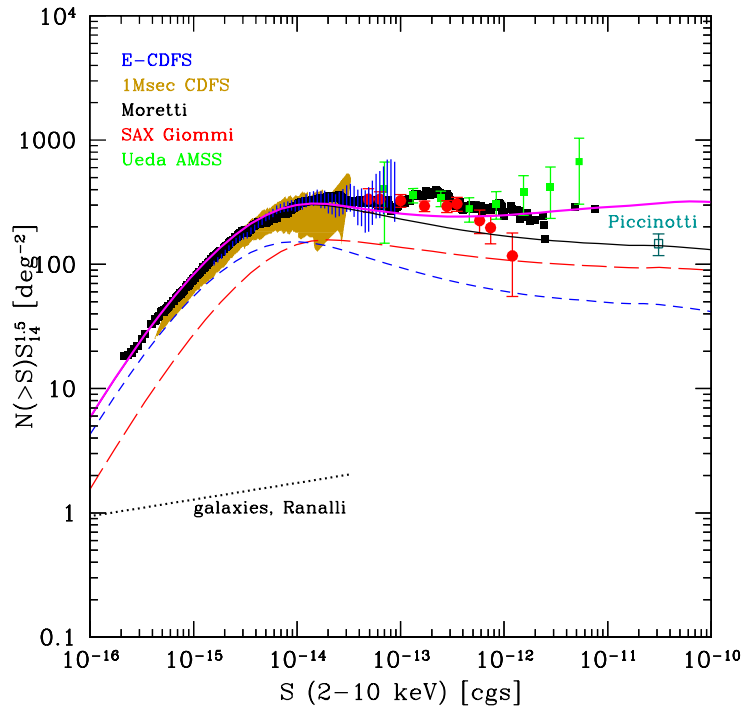


Figure 4. Cumulative hard AGN counts normalized to an Euclidean Universe. Datapoints are explained on the top left. The model curves and corresponding line styles are as in the previous Figure.

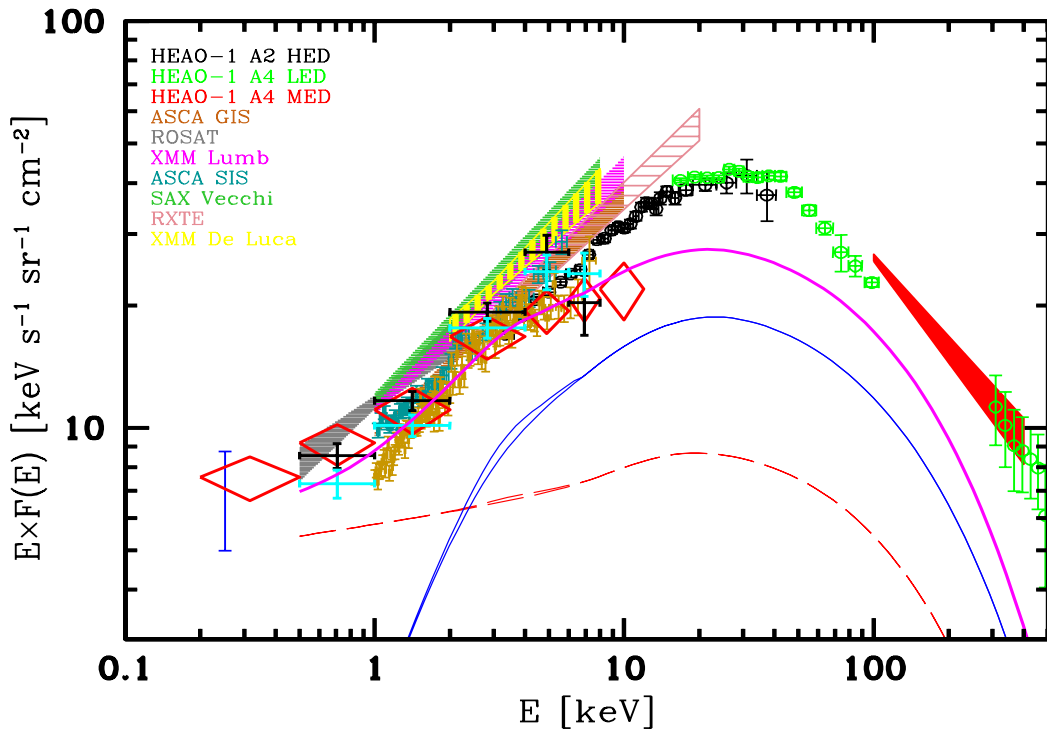


Figure 5. The cosmic XRB spectrum and predicted contribution from the population of Compton-thin AGN. The different XRB measurements are explained on the top left. Also shown are the resolved XRB fractions in different surveys by Worsley et al. (2005): Lockman Hole = red diamonds; CDFS = cyan crosses; CDFN = black crosses. Curves refer to model m2: unobscured AGN = red long-dashed line; obscured Compton thin AGN = blue short-dashed line; total (also including galaxy clusters) = magenta solid line.

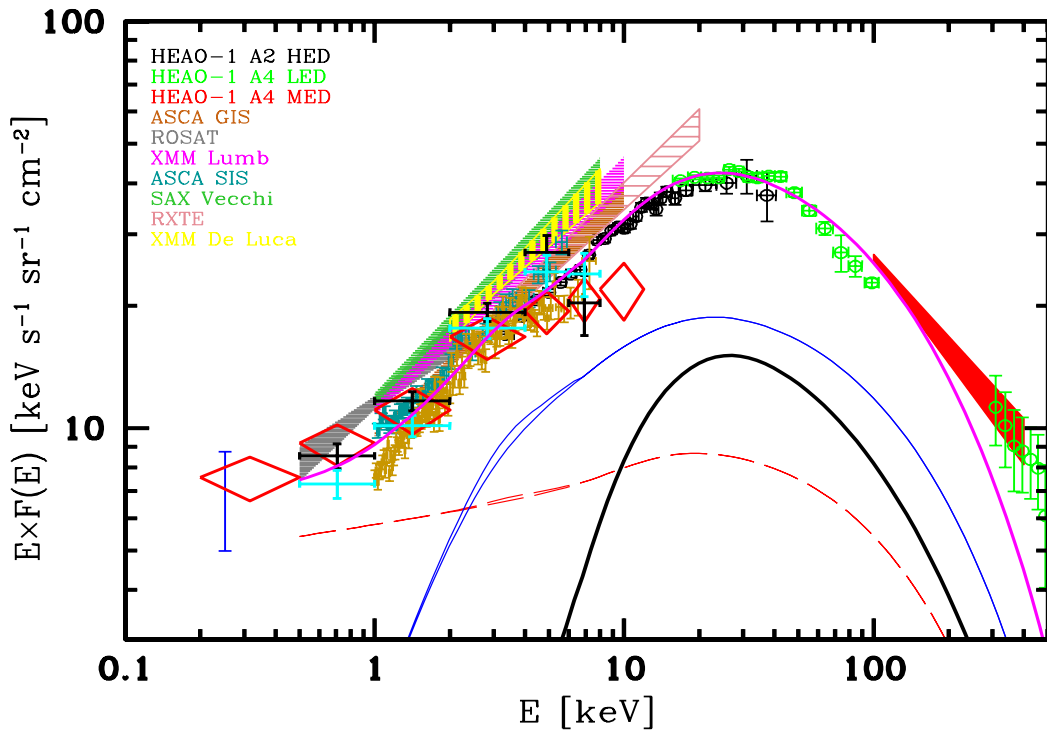


Figure 6. Same as in the previous Figure but with the additional contribution of Compton-thick sources (thick black line).

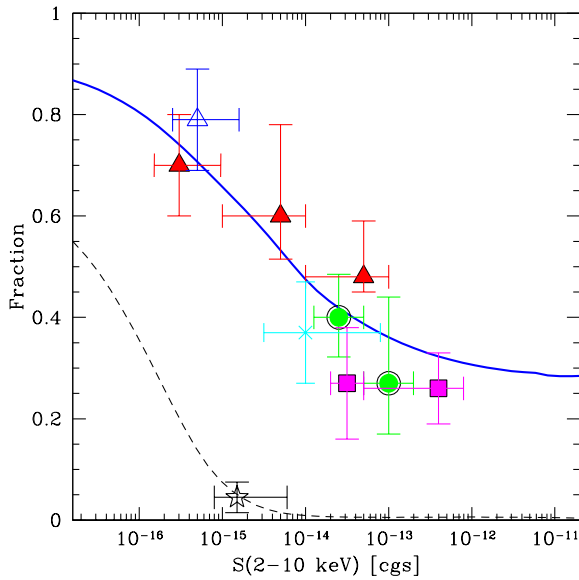


Figure 7. The fraction of obscured AGN as a function of the 2-10 keV limiting flux. Solid blue line: fraction of AGN with $\log N_H > 22$ expected by model m2. Colored points: fraction of AGN with $\log N_H > 22$ measured in different surveys (datapoints are described in Gilli et al. 2006 in prep). Black dashed line: fraction of AGN with $\log N_H > 24$ (i.e. Compton-thick) expected by model m2. Black star: fraction of Compton-thick AGN measured in the CDFS by Tozzi et al. (2005).

the reflected continuum (e.g. by the far inner side of the putative obscuring torus) provides a major contribution; in the second case absorption is extreme and no radiation is transmitted through the absorber, leaving a bare reflection continuum as the only visible component.

As shown in Fig. 6, the fit to the XRB spectrum measured by HEAO-1 in the range 10-300 keV requires a large number of Compton thick AGN (about twice as large as that of Compton-thin one). An even larger Compton-thick population would be required if the XRB flux were underestimated by HEAO-1.

The baseline model nicely reproduces the steep rising of the obscured AGN fraction as a function of hard limiting flux as estimated by several surveys (Fig. 7). Remarkably, the model predicted fraction of Compton-thick AGN closely matches the small ($\sim 5\%$) observed fraction of heavily obscured sources measured by Tozzi et al. (2005) in the Chandra Deep Field South (see again Fig. 7). Our results confirm that below 10 keV the large population of Compton thick sources is poorly sampled even by the deepest surveys.

ACKNOWLEDGMENTS

REFERENCES

- Alexander, D.M., Bauer, F.E., Brandt, W.N., et al. 2003, AJ, 126, 539
- Barger, A.J., Cowie, L.L., Capak, P., et al. 2003, AJ, 126, 632
- Comastri, A., Setti, G., Zamorani, G., & Hasinger, G. 1995, A&A, 296, 1
- Giacconi, R., Zirm, A., Wang, J., et al. 2002, ApJS, 139, 369
- Gilli, R., Salvati, M., & Hasinger, G. 2000, A&A, 366, 407
- Gilli, R. 2004, Ad. Sp. Res., 34, 2470
- Guainazzi, M., Matt, G., Perola, G.C. 2005, A&A, in press (astro-ph/0508265)
- Hasinger, G. 2004, Nuc. Phys. B Proc. Supp., 132, 86
- Hasinger, G., Miyaji, T., Schmidt, M. 2005, A&A, 441, 417
- La Franca, F., Fiore, F., Comastri, A., et al. 2005, ApJ, in press (astro-ph/0509081)
- Revnivtsev, M., et al. 2005, A&A, in press (astro-ph/0412304)
- Tozzi, P., Gilli, R., Mainieri, V., et al. 2005, A&A, in press
- Ueda, Y., Akiyama, M., Ohta, K., Miyaji, T. 2003, ApJ, 598, 886
- Worsley, M.A., Fabian, A.C., Bauer, F.E., et al. MNRAS, 2005, 357, 1281

THE XMM-LSS CLUSTER SAMPLE AND ITS COSMOLOGICAL APPLICATIONS

M. Pierre, F. Pacaud¹ and the XMM-LSS consortium²

¹DAPNIA/SAP CEA Saclay, 91191 Gif sur Yvette, France

²<http://vela.astro.ulg.ac.be/themes/spatial/xmm/LSS/cons.e.html>

ABSTRACT

We present the X-ray source detection procedure that we have developed for the purpose of assembling and characterizing controlled samples of cluster of galaxies for the XMM Large Scale Structure Survey. We describe how we model the selection function by means of simulations: this leads us to define source classes rather than flux limited samples. Focussing on the CFHTLS D1 area, our compilation suggests a cluster density higher than previously determined from the deep ROSAT surveys above a flux of $2 \times 10^{-14} \text{ erg cm}^{-2}\text{s}^{-1}$. We also present the L-T relation for the 9 brightest objects in the area. The slope is in good agreement with the local correlation. The relation shows luminosity enhancement for some of the $0.15 < z < 0.35$ objects having $1 < T < 2 \text{ keV}$, a population that the XMM-LSS is for the first time systematically unveiling.

Key words: Surveys, X-ray analysis, clusters of galaxies.

1. INTRODUCTION

The question of cosmic structure formation is substantially more complicated than the study of the spherical collapse of a pure dark matter perturbation in an expanding Universe. While it is theoretically possible to predict how the shape of the inflationary fluctuation spectrum evolves until recombination, we hardly understand the subsequent galaxy, AGN and cluster formation because of the problems of non-linear growth and the feedback from star formation. Consequently we cannot use the statistics of visible matter fluctuations to constrain the nature of the Dark Matter and Dark Energy without developing this understanding of non-gravitational processes. Clusters, the most massive entities of the Universe, are a crucial link in the chain of understanding. They lie at the nodes of the cosmic network, and have virialized cores, but are still growing by accretion along filaments. The rate at which clusters form, and the evolution of their space distribution, depends strongly on the shape and normalization of the initial power spectrum, as well as on the

Dark Energy equation of state (e.g. Rapetti et al. (2005)). Consequently, both a 3D mapping of the cluster distribution and an evolutionary model relating cluster observables to cluster masses and shapes (predicted by theory for the average cluster population) are needed to test the consistency of the ‘‘CMB WMAP concordance cosmology’’ with the properties of clusters in the low- z Universe. With its mosaic of 10 ks overlapping XMM pointings, the XMM Large Scale Structure survey (XMM-LSS) has been designed to detect a significant fraction of the galaxy cluster population out to a redshift of unity over an area of several tens of square degrees, so as to constitute a sample suitable to address the questions outlined above (Pierre et al. 2004). The trade-off in the survey design was depth versus coverage, keeping within reasonable total observing times.

This configuration allows investigation of the cluster population down to a depth of about $10^{-14} \text{ erg cm}^{-2}\text{s}^{-1}$ which is comparable to the deepest ROSAT serendipitous surveys (Rosati et al. 2002). However, observations are performed with a narrower PSF (FWHM $\sim 6''$ for XMM vs $\sim 20''$ for the ROSAT PSPC) and very different different instrumental characteristics such as background noise and focal plane configuration. This led us to develop a new X-ray pipeline which is presented in the next section, along with the principles of the computation of the survey selection function. Spectroscopically identified clusters undergo detailed measurements, which enabled us to track the evolution of the low-mass end of the cluster population (Sec. 3). Source statistics and the L-T relation for the CFHTLS D1 area are presented in Sec. 4. In the following, we assume a Λ CDM cosmology and give all fluxes in the [0.5-2] keV band.

2. XAMIN – A NEW X-RAY PIPELINE

2.1. Design

The two major requirements of the XMM-LSS X-ray processing were to reach the sensitivity limit of the data in a statistically tractable manner in terms of cluster detection efficiency, and hence to calculate the selection function

of the detected objects. The package that we have developed, `Xamin`, combines the sensitivity of the multi-resolution wavelet analysis for source detection with the rigour of a likelihood analysis for assessing the significance of the detected sources, handling the complex XMM instrumental characteristics. Both steps use Poisson statistics. The whole procedure has been validated by means of extensive simulations of point-like and extended sources (Pacaud et al. 2005).

2.2. Source classification

Simulations of the LogN-LogS X-ray point source population give for `Xamin` a 90% completeness level down to a flux of 4×10^{-15} erg cm $^{-2}$ s $^{-1}$ for 10 ks exposures. As a rule of thumb, the corresponding sensitivity for ‘typical’ cluster sources is 2-3 times higher. However, cluster detection efficiency depends not only on the object flux and size, and the instrumental PSF, but also very much on the background level and on the detector topology such as CCD gaps and vignetting, as well on the ability of the pipeline to separate close pairs of pointlike sources. We thus stress that the concept of sky coverage, i.e. the fraction of the survey area covered at a given flux limit, is strictly valid only for point-sources because, for faint extended objects, the detection efficiency is surface brightness limited (rather than flux limited). Moreover, since the faint end of the cluster luminosity function is poorly characterised at $z > 0$, it is not possible to estimate a posteriori what fraction of groups remain undetected, unless a cosmological model is assumed, along with a thorough modelling of the cluster population out to high redshift.

Consequently, with the goal of constructing deep controlled samples suitable for cosmology we define, rather than flux limits, two classes of extended sources corresponding to specific levels of contamination and completeness. The selection is performed in the `Xamin` output parameter space defined by `extent likelihood`, `extent`, `detection likelihood`. Selection criteria have been established by means of extensive simulations for cluster apparent core-radii (`extent`) ranging from 10” to 100”, and total number counts from 50 to 1000. The cluster surface brightness distribution was assumed to follow a β -model, with $\beta = 2/3$. The C1 class is defined to have “no contamination”. i.e. no point sources misclassified as extended. For the C2 class, selection criteria are relaxed such as to allow for 50% contamination by spurious extended sources. The classification has been in turned checked against some 60 spectroscopically XMM-LSS clusters confirmed to date. C1 clusters are high surface brightness extended objects; this selection inevitably retains a few nearby galaxies, but these are readily discarded from the sample by inspection of optical overlays. The C2 sample includes fainter clusters than C1, and also a number of nearby galaxies, saturated point sources and unresolved pairs, as well as cases badly effected by CCD gaps; the contamination is a posteriori removed by the visual inspection of the optical overlays as well as by the

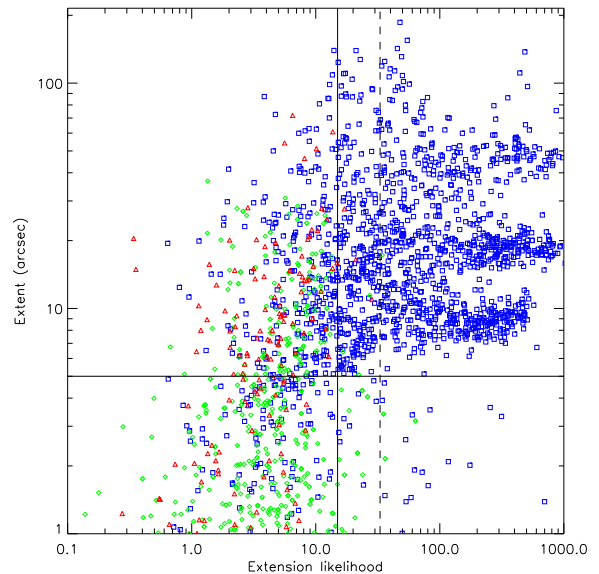


Figure 1. Cluster selection criteria in the `Xamin` parameter space populated by simulations. Point sources are represented by green diamonds, clusters by blue squares; red triangles indicate spurious sources. The horizontal and vertical solid lines delineate the C1+C2 class. The dotted vertical line indicates the restriction to the C1 class to which the detection likelihood > 32 condition was added, guaranteeing an uncontaminated sub-sample of clusters

outcome of the spectroscopic identification programme. The principle of the procedure is illustrated in Fig. 1.

2.3. The survey selection function

In parallel, simulations provide the necessary basis for the computation of the selection function. They allow us to derive detection probabilities as a function of source core-radius and countrate for any exposure time, background level and position on the detector (Fig. 2). As an example, we show the dn/dz prediction for the C1 cluster population, assuming the following model: Λ CDM cosmology (Bennett et al. 2003) + P(k) power spectrum with transfer function from Bardeen et al. (1986) and comoving halo number density from the Sheth & Tormen (1999) mass function, $M_{200} - T$ relation from Arnaud et al. (2005), $L - T$ relation from Arnaud & Evrard (1999) and a constant core radius of 180 kpc. The cluster/group population was simulated down to $T = 1$ keV (no evolution of the cluster M-T-L scaling laws was assumed, as it is currently unconstrained by observations for the $1 < T < 3$ keV range which constitute the bulk of our population). The predicted C1 dn/dz is shown in Fig. 3, along with the observed redshift distribution of the observed C1 population. The agreement is very satisfactory and the data suggest a deficit of clusters around a redshift of 0.5, probably induced by a cosmic void. Ob-

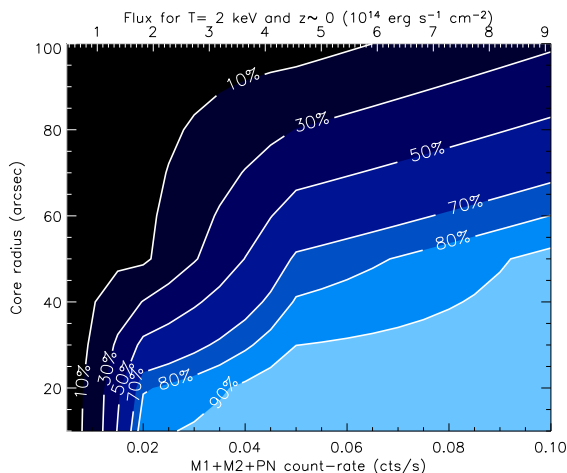


Figure 2. Detection probability for C1-type clusters as a function of count rate and core-radius, averaged for the 20 inner arcmin of the XMM field, and for an exposure time of 10 ks

served cluster numbers from the currently available 51 XMM-LSS pointings are $7/\text{deg}^2$ and $12/\text{deg}^2$ for the C1 and C2 class respectively. Finally, we have investigated for our simple cosmological model, to what extent the C1 and C2 classes are comparable to flux limited samples (Fig. 4). The main result is that the C1 sample approaches, in terms of number density, a flux limited sample of about $2 \times 10^{-14} \text{ erg cm}^{-2} \text{ s}^{-1}$. But (1) more high- z objects are detected, while nearby low-surface brightness groups are not retained, and (2) the C1 sample is strictly defined from X-ray criteria (and hence is not contaminated) while it would be necessary to examine a large number of sources to clean a putative flux limited sample at $2 \times 10^{-14} \text{ erg cm}^{-2} \text{ s}^{-1}$, with many of them not being unambiguously characterized as extended or point-like.

3. CLUSTER MEASUREMENTS

Each spectroscopically confirmed cluster undergoes detailed spectral and spatial fits in order to determine its temperature, flux and bolometric luminosity within R_{500} (standard overdensity radius). In particular, we have demonstrated that, under specific statistical model and binning conditions, we reach a 20% accuracy in temperature measurements with ~ 100 and ~ 300 photons for 1 and 2 keV groups respectively (Willis et al. 2005). It turns out that the C1 cluster sample is almost identical to the sample for which we can measure temperatures.

4. RESULTS FROM THE D1 CFHTLS AREA

The D1 CFHTLS area covers 1 deg^2 and constitutes the central part of the XMM-LSS (see Pierre et al. (2004) for a general layout of multi-wavelength coverage associated

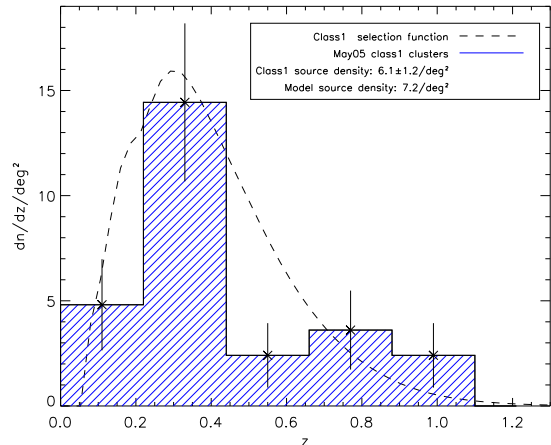


Figure 3. Redshift distribution of the C1 clusters for the current XMM-LSS area: 48 pointings covering 4.6 effective deg^2 (only the inner 20 arcmin are considered) – that is 29 objects. The dotted line corresponds to the predictions from a simple halo model in a Λ CDM cosmology (see text).

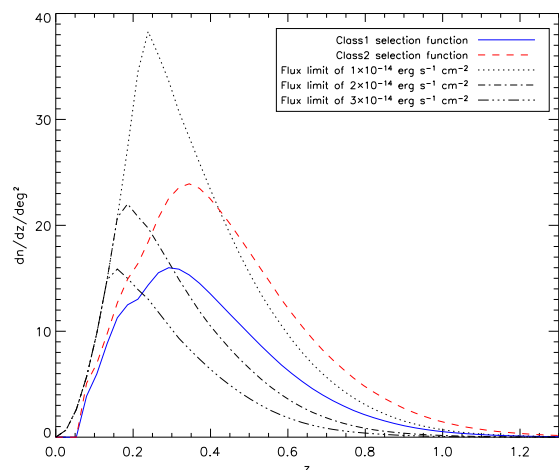


Figure 4. Comparison of the C1 and C1+C2 redshift distribution with various flux-limited samples, assuming the simple cosmological model described in the text

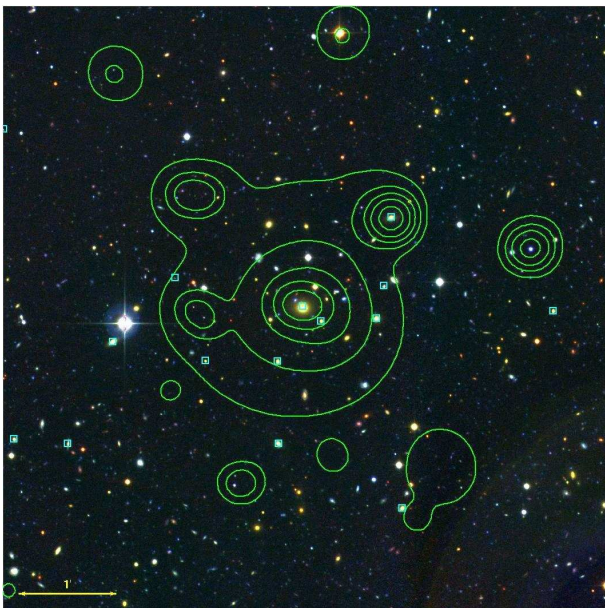


Figure 5. Example of a C1 cluster at $z = 0.26$ ($F \sim 8 \times 10^{-14} \text{ erg cm}^{-2}\text{s}^{-1}$). The cluster X-ray contours are overlaid on a u,r,z CFHTLS composite. They are drawn from the co-added $[0.5-2] \text{ keV}$ MOS1+MOS2+pn mosaic, filtered in the wavelet space using a significance threshold of 10^{-3} for Poisson statistics (not corrected for vignetting). The intensity scale is logarithmic (counts/pixel/second, not corrected for vignetting). Boxes indicate cluster members for which we obtained a redshift using LDSS at the Magellan telescope.

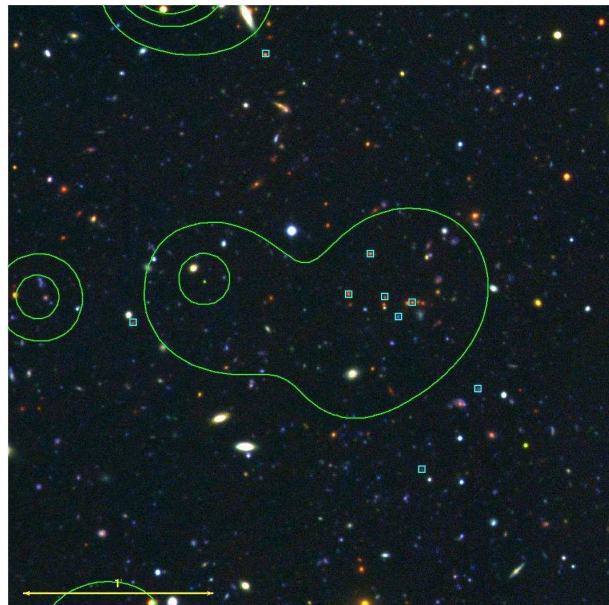


Figure 6. Example of a faint cluster at $z = 0.92$ at the detection limit ($F \sim 3 \times 10^{-15} \text{ erg cm}^{-2}\text{s}^{-1}$). The source was not spectroscopically followed-up. Redshift confirmation comes from the VVDS data alone. Same symbols and contours as in Fig. 5

with the XMM-LSS). It includes among others the Vimos VLT Deep Survey (VVDS, Bondi et al. (2003)). We present a summary of the properties of the cluster sample for this region¹. We have spectroscopically identified 13 clusters over the 0.8 deg^2 effective area. Out of these, 8 are C1 clusters, 1 is classified as C2, and 4 are clusters not entering the classification (very faint objects or clusters contaminated by a point source). The selection function for these 4 latter systems is unknown, but they are interesting objects indicative of our ultimate detection limit, i.e. $\sim 3 - 5 \times 10^{-15} \text{ erg cm}^{-2}\text{s}^{-1}$. Two examples are illustrated on Figs. 5 and 6. The C1+C2 clusters span the $0.05 < z < 1.05$ redshift range, with bolometric luminosities ranging from 0.1 to $4 \times 10^{44} \text{ erg s}^{-1}$.

7 clusters are found above a flux of $2 \times 10^{-14} \text{ erg cm}^{-2}\text{s}^{-1}$. This translates to about $8.5/\text{deg}^2$. We have investigated the L-T relation for the 9 clusters for which it was possible to measure a temperature. Results are displayed on Fig. 7 as a function of redshift. Malmquist bias is here obvious since a temperature was derived only for the apparently brightest clusters. The overall correlation appears to be quite tight and well summarizes the ability of rather shallow XMM survey-type observations to provide important new insights into the cluster population. This is particularly relevant for groups out to

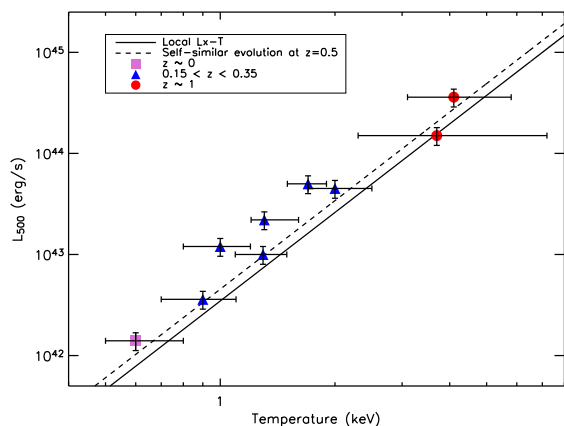


Figure 7. $L(R_{500})$ - T relation for the D1 area clusters for which a temperature was obtained. The solid lines gives the mean local L - T relation, while the dotted line is the expected luminosity enhancement from the self-similar model, at a mean redshift of 0.5. The various symbols show the 3 distinct redshift (and luminosity/mass) regimes of the measured clusters.

¹XMM exposure time is 20 ks over the region but we keep the same class definition as the S/N increase is only $\sqrt{2}$; the net effect being only a slight increase in C1/C2 number density ratio for this sub-region

$z \sim 0.4$ that the XMM-LSS is systematically unveiling for the first time. Our intermediate redshift subsample of groups (0.9-2 keV for $z_{med} = 0.25$) contains objects more luminous than predicted by the self similar evolution model. According to this hypothesis, the luminosity scales as the Hubble constant if it is integrated within a radius corresponding to a fixed ratio with respect to the critical density of the universe (Voit 2005). From the local universe, we know that low temperature groups show a larger dispersion in the L-T relation than massive clusters (Helsdon & Ponman 2003). This reflects their individual formation histories, since they are particularly affected by non-gravitational effects, as well as the possible contributions from their member galaxies. The apparent biasing toward more luminous objects and/or cooler system could come from the fact that we detect more easily objects having a central cusp, i.e. putative cool-core groups. This is under investigation using the full sample available from the current XMM-LSS area (Pacaud et al in preparation). Detailed presentation of the D1 catalogue and results are given by Pierre et al. (2005).

5. SUMMARY AND CONCLUSIONS

We have developed an X-ray pipeline enabling the construction, from shallow XMM pointings, of samples of galaxy clusters with controlled selection effects. In particular, “first class” clusters constitute a sample selected upon X-ray criteria alone (once nearby galaxies are removed). This approach offers the advantage of avoiding hypotheses about the faint end of the cluster LogN-LogS (currently not explored beyond the local universe) since this can become critical for faint samples said to be “flux limited”. The C1 class contains objects as faint as $\sim 10^{-14}$ erg cm $^{-2}$ s $^{-1}$ out to redshifts of unity. The final C1+C2 sample reaches a density of 12/deg 2 but the initial C2 selection has to be cleaned (by inspection of overlays and possibly optical spectroscopy) of a similar density of spurious cluster candidates (~ 5 /deg 2).

We systematically unveil the low end ($T < 2$ keV) of the cluster population out to a redshift of 0.4. For the D1 CFHTLS area, we find a cluster density of 8.5 clusters per deg 2 having a flux larger than 2×10^{-14} erg cm $^{-2}$ s $^{-1}$. This is higher than the 4-5 clusters /deg 2 given by the RDCS LogN-LogS (Rosati et al. 1998) and the shallow XMM/2dF survey (Gaga et al. 2005), which finds 7/2.3 = 3 /deg 2 for the same flux limit. Given the size of the studied area, our results are certainly subject to cosmic variance which may also affect the 2.3 deg 2 XMM/2df survey and, to a lesser extent, the RDCS, which covers 5 deg 2 at 2×10^{-14} erg cm $^{-2}$ s $^{-1}$ (Rosati et al. 2002). For comparison, our simple cosmological model predicts some 7.5 clusters /deg 2 having $T > 1$ keV above a flux of 2×10^{-14} erg cm $^{-2}$ s $^{-1}$ (Pacaud et al. 2005).

We present the first L-T relation from XMM survey-type observations over a contiguous area. The relation contains 9 clusters out to a redshift of unity over only ~ 1 deg 2 and so, opens remarkable perspectives for the study the evolution of the scaling laws for the cluster/group population with moderate XMM exposure

times. On-going work aims at characterizing the evolution of the L-T relation for the $T < 2$ keV population over the currently available 7 deg 2 of the XMM-LSS (including the Subaru Deep Survey). In parallel, extensive simulations of XMM images enable us to investigate the effect of the cluster scaling laws (M-L-T-R), and of their evolution, on the survey selection function. These will be further constrained by the APEX and AMiBA Sunyaev-Zel’dovich surveys of the region to be performed in 2006. It will then be possible to model in a self-consistent way the cluster population in parallel with constraining cosmological parameters.

ACKNOWLEDGMENTS

This work is based on data obtained with XMM, VLT/FORS2, VLT/VIMOS, NTT/EMMI, Magellan/LDSS, and imaging campaigns performed at CTIO and CFHT 2 .

REFERENCES

- Arnaud, M. & Evrard, A. E. 1999, MNRAS, 305, 631
- Arnaud, M., Pointecouteau, E., & Pratt, G. W. 2005, A&A, 441, 893
- Bardeen, J. M., Bond, J. R., Kaiser, N., & Szalay, A. S. 1986, ApJ, 304, 15
- Bennett, C. L., Halpern, M., Hinshaw, G., et al. 2003, ApJS, 148, 1
- Bondi, M., Ciliegi, P., Zamorani, G., et al. 2003, A&A, 403, 857
- Gaga, T., Plionis, M., Basilakos, S., Georgantopoulos, I., & Georgakakis, A. 2005, MNRAS, 870
- Helsdon, S. F. & Ponman, T. J. 2003, MNRAS, 340, 485
- Pacaud, F., Pierre, M., & et al. 2005, MNRAS, submitted
- Pierre, M., Pacaud, F., & et al. 2005, MNRAS, submitted
- Pierre, M., Valtchanov, I., Altieri, B., et al. 2004, Journal of Cosmology and Astro-Particle Physics, 9, 11

²The cluster optical images were obtained with MegaPrime/MegaCam, a joint project of CFHT and CEA/DAPNIA, at the Canada-France-Hawaii Telescope (CFHT) which is operated by the National Research Council (NRC) of Canada, the Institut National des Sciences de l’Univers of the Centre National de la Recherche Scientifique (CNRS) of France, and the University of Hawaii. This work is based in part on data products produced at TERAPIX and the Canadian Astronomy Data Centre as part of the Canada-France-Hawaii Telescope Legacy Survey, a collaborative project of NRC and CNRS

Rapetti, D., Allen, S. W., & Weller, J. 2005, MNRAS, 360, 555

Rosati, P., Borgani, S., & Norman, C. 2002, ARA&A, 40, 539

Rosati, P., della Ceca, R., Norman, C., & Giacconi, R. 1998, ApJ, 492, L21+

Sheth, R. K. & Tormen, G. 1999, MNRAS, 308, 119

Voit, M. 2005, Rev. Mod. Phys. (in press)

Willis, J. P., Pacaud, F., Valtchanov, I., et al. 2005, MNRAS, 363, 675

UNVEILING THE DISTRIBUTION OF ABSORPTION IN THE AGN POPULATION

T. Dwelly and M.J. Page

Mullard Space Science Laboratory, UCL, Holmbury St. Mary, Dorking, Surrey, UK

ABSTRACT

We use the very deep *XMM-Newton* observations in the CDF-S to measure the distribution of absorption in the AGN population. We describe the Monte Carlo method used to unveil the intrinsic properties of the AGN using their multi-band X-ray colours. The measured distribution of AGN in z , L_X and N_H space is compared with the distributions predicted by a number of XLFs and absorption models. In contrast to other studies, we do not find any evidence that the absorption distribution is dependent on redshift or intrinsic luminosity.

1. INTRODUCTION

A large population of absorbed AGN are required to explain the hard spectrum of the extragalactic X-ray background. However, even though absorbed AGN outnumber their unabsorbed brethren by a factor of four in the local Universe (e.g. Risaliti et al., 1999, ApJ, 522, 157), the demographics of the population at higher redshifts are still poorly understood. The simple “unified” model of AGN attributes this absorption to a 1–100pc scale dusty torus surrounding the central black hole and accretion disk, where the degree of absorption seen by an observer is determined primarily by the angle at which an AGN is viewed. By measuring the distribution of absorption in the AGN population we can place constraints on the typical geometry of such a torus. In addition, we can test for the existence of a correlation between absorption and redshift and/or luminosity. Therefore, we have examined a sample of X-ray sources detected in the deep *XMM-Newton* observations of the *Chandra* Deep Field-South (CDF-S).

2. OBSERVATIONS AND SAMPLE SELECTION

The *XMM-Newton* data in the CDF-S consist of 500ks of observations, of which around 350ks is unaffected by background flares. This is the 2nd deepest *XMM-Newton* survey to date. We subdivide the full energy range of the EPIC cameras into four bands: 0.2–0.5, 0.5–2, 2–5, and 5–10 keV. We detect 299 reliable X-ray sources to a limiting flux of $\sim 10^{-16}$ erg cm $^{-2}$ s $^{-1}$ in the 0.5–2 keV band. The entire field is covered by deep *Chandra*

imaging (Extended-CDF-S project; Lehmer et al., 2005, AJ, 129, 1), and the central region is covered by very deep (1Ms) *Chandra* observations (Giacconi et al., 2002, ApJS, 139, 639). For unambiguous optical identification, we adopt the high accuracy *Chandra* positions where possible. Extensive spectroscopic identification programs have been carried out in the CDF-S especially for optical counterparts of the *Chandra* sources, (e.g. Szokoly et al., 2004, ApJS, 155, 271; Zheng et al., ApJS, 155, 73Z). Almost the entire *XMM-Newton* field is also covered by the COMBO-17 survey (Wolf et al., 2004, A&A, 421, 913), which provides good photo- z estimates for galaxies to $R=24$. We find that 86% (258/299) of the *XMM-Newton* detections have identified optical counterparts. Of these, 16 sources are stars, and 5 suffer from source confusion; these sources are removed from the sample.

3. DATA ANALYSIS AND RESULTS

We have used detailed simulations in order to understand the selection function and any biases inherent to the *XMM-Newton* observations (and the source searching algorithm). We couple X-ray luminosity functions with an empirical absorption distribution model to generate a random synthetic population of “input” AGN. The multi-band count-rates expected for each simulated AGN are then calculated according to an absorbed power-law plus reflection spectral model, taking into account the EPIC response. Simulated multi-band images are generated using the EPIC PSF together with the exposure maps and unresolved background of the real observations. We apply the source searching routine that is used on the real data in order to find “output” sources in these images. Each “output” source is matched to the appropriate “input” counterpart, allowing its output parameters (i.e. multi-band count rates), to be related to input parameters (i.e. z , L_X , and N_H). The simulation process is repeated for the equivalent of 2000 fields in order to populate densely z, L_X, N_H space. See Loaring et al. (2005, MNRAS, 362, 137), and Dwelly et al. (2005, MNRAS, 360, 1426), for a detailed description of this process. We use this library of simulated sources to find the most likely N_H of the AGN in our CDF-S sample. For each AGN, we select all those simulated sources having similar multi-band hardness ratios (HRs), redshifts and full band count rates. The best estimate for the N_H of

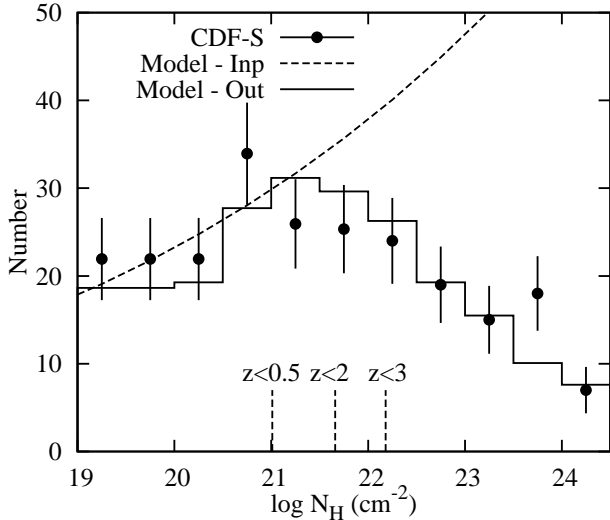


Figure 1. The distribution of absorption in the XMM-Newton CDF-S sample, compared to the prediction from the best fitting N_H distribution model (the $\beta = 5$ absorption distribution, see text). We show the input model N_H distribution (before selection effects) as well as the recovered distribution in the simulated output population. Vertical dashed lines show the lowest value at which we can determine the absorbing column at a given redshift. All those sources which are determined to have a column lower than the limit for their redshift are divided equally between the bins lower than this N_H limit.

the real AGN is taken to be the modal “input” N_H of this subset of simulated sources. We have checked the fidelity of this method by using it to recover the known N_H of simulated sources. We find that for simulated sources at $z < 2$, and with $N_H > 10^{21.5} \text{ cm}^{-2}$, we are able to recover the input absorption reliably. At higher redshifts, absorption is shifted out of band, and so we are only able to place upper limits for moderately absorbed AGN. We use a similar method to deduce the “de-absorbed” intrinsic rest frame 2–10 keV luminosities of the sample. As before, we select all simulated sources having similar HRs , redshift, and full band count rate to the real AGN. The weighted median luminosity of these simulated objects is taken to be the best estimate of the intrinsic luminosity of the AGN. The scatter of the recovered values about the input values is typically less than 0.2dex. We compare the z, N_H, L_X distribution of the CDF-S sample with those predicted by a number of model N_H functions, coupled with the model XLF of Ueda et al. (2003, ApJ, 598, 886). We have compared the predictions of a range of absorption distributions including those of Ueda et al. (2003), Treister et al. (2004, ApJ, 616, 123), and Gilli et al. (2001, A&A, 366, 407), as well as a simple parameterisation where $dN/d\log N_H \propto (\log N_H)^\beta$, $\beta = 2, 5, \text{ or } 8$. We fold these model populations through our Monte Carlo process, and then estimate the output N_H and L_X of the simulated sources in the same way as for the AGN in the CDF-S sample. The N_H and L_X distributions found in the CDF-S sample are compared to the predictions made by the best matching model ($\beta = 5$) in figures 1 and 2.

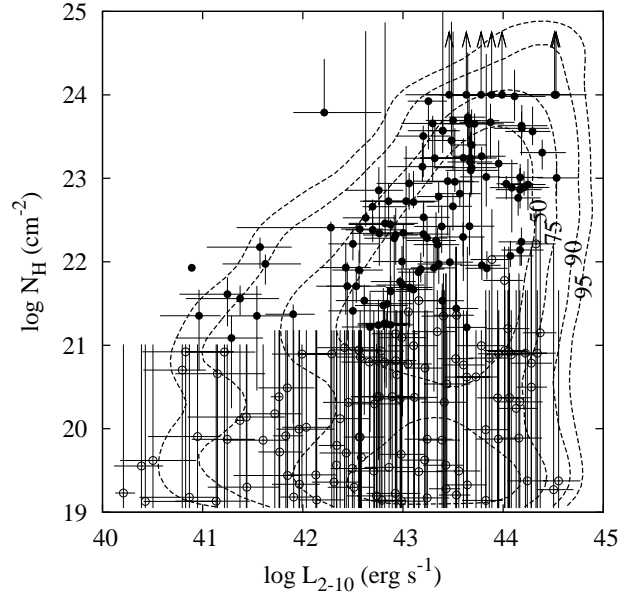


Figure 2. The 2–10 keV L_X vs N_H distribution of the CDF-S sample (points). Sources for which we can only determine upper limits on N_H are shown with open symbols. Contours show the distribution predicted by the $\beta = 5$ model (contour levels are set to include 50%, 75%, 90% and 95% of the model sources).

4. DISCUSSION

We have demonstrated a Monte Carlo method for accurately estimating the X-ray absorption and intrinsic luminosity in a sample of optically identified AGN observed with XMM-Newton. Our CDF-S sample reaches to high redshifts ($z < 4$), and spans the knee of the luminosity function ($L^* \sim 10^{44} \text{ erg s}^{-1}$). We find that $\sim 35\%$ of the identified sources are heavily absorbed AGN ($\log N_H > 22$). Our N_H estimation method finds evidence for moderate absorption ($21 < \log N_H < 22$) in ~ 70 AGN; Obscuration models where AGN are surrounded by uniformly dense tori do not predict large numbers of these intermediately absorbed objects. The model which best reproduces the N_H distribution of the CDF-S sample is a simple parametrisation, where the number of AGN having absorption per unit $\log N_H$ is proportional to $(\log N_H)^\beta$ (the $\beta = 5$ model). After allowing for selection effects in the sample, we see no strong dependence of the N_H distribution on either redshift or luminosity in the ranges probed by this sample. When compared to the three dimensional z, L_X, N_H distribution of the sample, the best matching N_H distribution was again the $\beta = 5$ model, which matched with 3-D KS probability $P_{3D-KS} = 0.01$. The main source of the disparity is the redshift distributions: the sample is strongly peaked at $z \sim 0.7$ (e.g. Gilli et al. 2003, ApJ, 592, 721), a feature not reproduced by the model XLF. This work highlights the importance of high quality, broad-band X-ray spectral information in determining the N_H distribution of faint sources, and the need to account rigorously for selection effects.

THE FLUX AND ANGULAR DISTRIBUTION OF AXIS SOURCES

J. Ebrero¹ and F. J. Carrera¹

¹Instituto de Física de Cantabria (CSIC-UC), Av. de los Castros, 39005 Santander, Spain

ABSTRACT

We present here the XMM-Newton International Survey (AXIS) sample which is the largest homogeneous calibrated serendipitous medium-deep XMM-Newton X-ray source sample that currently exists, comprising a total of 1444 sources in 36 XMM-Newton fields, with a sky coverage of almost 5 square degrees. We have constructed samples in four different bands: Soft (0.5 - 2 keV), Hard (2 - 10 keV), XID (0.5 - 4.5 keV) and UltraHard (4.5 - 7.5 keV), which is hardly explored so far, reaching fluxes of a few 10^{-15} cgs in the Soft and XID bands, and $\sim 10^{-14}$ cgs in the Hard and UltraHard bands.

We have combined our sample with other shallower and deeper XMM-Newton and Chandra samples to construct logN-logS distributions over very wide flux ranges. The log $N - \log S$ were well fitted with broken power law models in all bands, except for the ultrahard band, in which there is no break down to our faintest fluxes.

We have also studied the large scale distribution of the medium flux X-ray sky, using the field-to-field cosmic variance in the number of sources, and the angular correlation function of the sources, finding evidence for large scale inhomogeneities.

In an accompanying presentation we discuss the optical identification status and results of a subsample, called XMS (XMM-Newton Medium Sample)

Key words: X-ray sources; logN-logS; angular distribution.

1. INTRODUCTION

The AXIS (An XMM-Newton International Survey: <http://venus.ifca.unican.es/~xray/AXIS/>) survey is the largest homogeneous calibrated sample of X-ray serendipitous sources at medium fluxes (Barcons et al., 2002). In this work we present some results on the flux and angular distributions of AXIS sources: the

log $N - \log S$ relationships and the two-point angular correlation function of the sources, respectively.

The AXIS sample comprises a total of 1444 different sources in 36 XMM-Newton fields. The overall sky coverage is almost 5 square degrees. We have constructed samples in 4 different bands: Soft (0.5-2 keV), Hard (2-10 keV), XID (0.5-4.5 keV) and UltraHard (4.5-7.5 keV). The UltraHard band is quite unexplored so far but it is starting to show some promising results. We reach fluxes of a few 10^{-15} cgs in the Soft and XID bands and $\sim 10^{-14}$ cgs in the Hard and UltraHard bands.

The overall shape of the X-ray spectra of the AXIS sources has been fitted by a simple power law model corrected by local absorption.

2. THE LOG $N - \log S$ RELATIONSHIPS

To carry out our log $N - \log S$ analysis we have added to our sample sources from other surveys in order to cover a wider flux range and therefore obtain more accurate results. In the Soft and Hard bands we have added sources from the CDF North & South (Bauer et al., 2004) at the faint end of our flux distribution while in the XID and UltraHard bands we have added sources from BSS and HBSS surveys respectively (Della Ceca et al., 2004), which are brighter than ours, in order to broaden our flux coverage.

Fits were carried out using a Maximum Likelihood algorithm that was performed over the individual sources (no binning was applied to the sources when fitting). Our log $N - \log S$ distributions confirm the existence of a break at fluxes around 10^{-14} cgs in Soft, Hard and XID bands so a broken power law model was therefore used to perform the fits. In the UltraHard band, however, no break has been observed yet and a simple power law was applied to this case.

The slopes obtained are in good agreement with other fits previously done (Moretti et al., 2003; Baldi et al., 2002), fixing the uncertainties that Baldi et al. had at faint fluxes in the soft band when calculating the log $N - \log S$ for

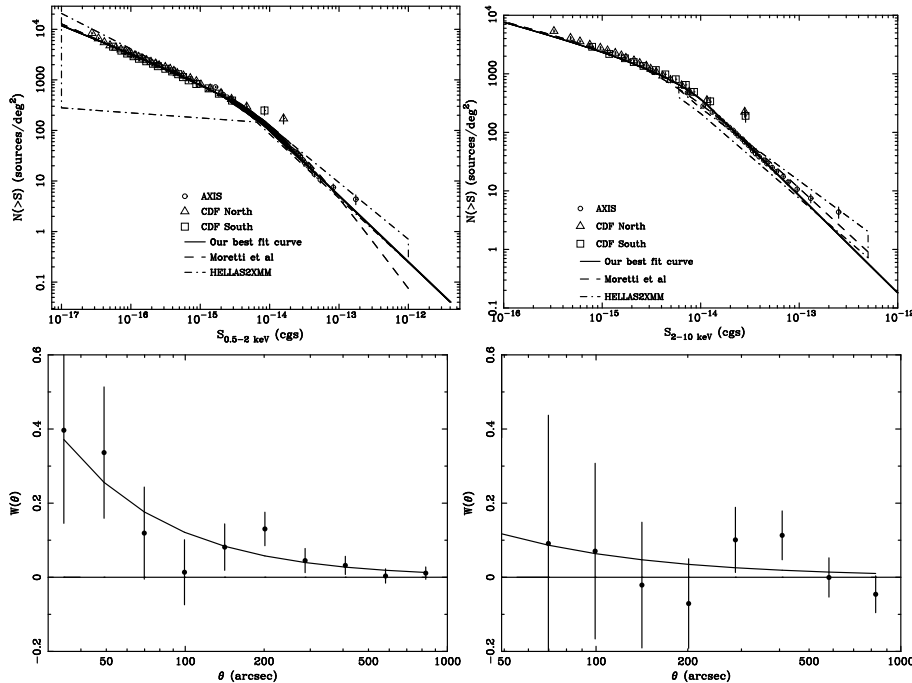


Figure 1. **Upper panels:** $\log N - \log S$ plot for AXIS+CDF Soft (left) and Hard (right) sources. The solid line is our best fit curve. Dashed line is the fit from Moretti et al. (2003). Dot-dashed line are the results from Baldi et al. (2002) with the HELLAS2XMM survey. **Lower panels:** The two-point angular correlation function for Soft (left) and Hard (right) sources. $w(\theta) = 0$ is the no correlation line. Our fits assume a power law model.

the HELLAS2XMM survey. (Fig. 1, upper panels) (for further details see Carrera et al., 2006, in preparation).

3. THE ANGULAR CORRELATION FUNCTION

We have also calculated the two-point angular correlation function (ACF) of the AXIS sources seeking out for large-scale inhomogeneities. The ACF $w(\theta)$ is the joint probability of finding sources separated by an angular distance θ . Our estimator is the same used by Efstathiou et al., (1991) and by Basilakos et al., (2005). Hence, this function measures the excess of sources compared with that of a random distribution. In the absence of correlation $w(\theta) = 0$.

We have drawn a random sample of sources from our own source list taking into account the variations in sensitivity with the position in a given field. A source with a count rate above the sensitivity map in its position is kept in our random sample; otherwise, it is discarded and a new source is randomly drawn from the whole dataset. This way we have generated random catalogues with up to 1 million sources in each energy band.

Angular distances between all Data-Data (DD) and Data-Random (DR) pairs are calculated for each field. The number of DD pairs compared with the DR ones within a bin $\theta \pm d\theta$ (normalized by the total number of detected real and random sources) provides a measure of the ACF.

Our preliminary analysis show that evidences of clustering are found in Soft and XID bands with a significance of $\sim 3\sigma$ whereas in the Hard and UltraHard bands no significant detections are seen although some works (e.g. Basilakos et al., 2005) point in a different direction. (Fig. 1, lower panels).

Fitting the angular correlation function assuming a single power law model yields to slope values consistent with the canonical value of $\gamma = -0.8$ (Basilakos et al., 2005; Akylas et al., 2000; Maller et al., 2005) within the errors though a bit steeper (for further details see Carrera et al., 2006, in preparation).

REFERENCES

- [1] Akylas, A. et al., 2000, MNRAS, 318, 1036
- [2] Baldi, A. et al., 2002, ApJ, 564, 190
- [3] Barcons, X. et al., 2002, A&A, 382, 522
- [4] Basilakos, S. et al., 2005, MNRAS, 356, 183
- [5] Bauer, F. E. et al., 2004, AJ, 128, 2048
- [6] Della Ceca, R. et al., 2004, A&A, 428, 383
- [7] Efstathiou, G. et al., 1991, ApJ, 380, 47
- [8] Maller, A. H. et al., 2005, ApJ, 619, 147
- [9] Moretti, A. et al., 2003, ApJ, 588, 696

GALAXIES BEYOND THE LIMITS OF CURRENT DEEP X-RAY SURVEYS: RESULTS OF STACKING

Richard E. Griffiths, Takamitsu Miyaji & Adam Knudson

Physics Dept., Carnegie Mellon University, Pittsburgh 15213, USA

ABSTRACT

The great sensitivities of the Chandra X-ray Observatory and XMM-Newton are allowing us to explore the X-ray emission from galaxies at moderate to high redshift. By using the stacking method with CXO data, we can detect the ensemble emission from normal elliptical, spiral and irregular galaxies out to redshifts approaching one. The average X-ray luminosity can then be compared with the results of models of the evolution in the numbers of X-ray binaries and can possibly be used to constrain models of star formation. In order to account for the increasing luminosity of spiral galaxies from low to moderate redshift, AGN components may need to be invoked.

Key words: \LaTeX ; X-ray background; X-ray number counts; galaxies; spirals; ellipticals; irregulars; active galactic nuclei.

1. INTRODUCTION

Deep surveys in X-ray astronomy had the initial goal of solving the problem of the origin of the extragalactic X-ray background, and these surveys have now shown that the XRB is largely comprised of the evolving populations of AGN, some heavily absorbed (Hasinger et al. 2005). But the deep surveys with the Chandra X-ray Observatory (CXO) have shown that normal galaxies are also detected. The initial 1Ms survey of the Hubble Deep Field (HDF) North demonstrated that, at flux levels approaching 10^{-16} cgs (0.5 - 2.0 keV), about a third of the X-ray sources were identified with galaxies (Hornschemeier et al. 2002, 2003). The extension of this survey to 2Ms. has confirmed and expanded these findings.

We can thus begin to explore the evolution of extragalactic source populations in addition to the AGN, LINERs and clusters of galaxies which dominated the number counts in the flux ranges explored by the *Einstein*, *ROSAT* and *ASCA* observatories in the previous two decades. It has long been recognised that normal galaxy populations would eventually be observed in deep X-ray surveys

given enough sensitivity. It was not clear that this would happen with the Chandra X-ray Observatory.

2. DEEP SURVEYS AND SOURCE COUNTS

The number counts in the HDF-N have been measured by Miyaji & Griffiths (2002), and extended to fluxes below 10^{-17} ergs cm^{-2} s^{-1} in the soft band (0.5 - 2 keV) and to 10^{-16} ergs cm^{-2} s^{-1} in the hard band (2 - 10 keV) by analysis of the fluctuations which remain after removal of the individual discrete source detections. Below this limit, the fluctuation analysis shows that the number counts continue to rise, as shown in Fig. 1, with a slope consistent with that between 10^{-15} and 10^{-16} ergs cm^{-2} s^{-1} .

At X-ray fluxes between 10^{-15} and 10^{-16} ergs cm^{-2} s^{-1} in the HDF-N, Hornschemeier et al. (2002, 2003) showed that about a third of sources were identified with galaxies. The extension of this survey to 2Ms. has confirmed and expanded these findings. We infer that the number counts in the region explored with fluctuations (the boxed area in Fig. 1) are unlikely to be due to AGN. Furthermore, the current best models for the AGN contributions to the number counts fall well below the fluctuations. The fluctuations analysis shows that the number counts are approximately 20,000 - 40,000 per sq. deg. at X-ray fluxes of 10^{-17} ergs cm^{-2} s^{-1} . Such number counts match those of the optical counts of galaxies at $B = 24$. We therefore explore the possibility of X-ray detection of faint galaxies in the HDF-N by using the stacking method.

3. SELECTION OF GALAXIES BY MORPHOLOGICAL TYPE AND LUMINOSITY

During the execution of the Medium Deep Survey using the Hubble Space Telescope, software was developed for the automated classification of galaxies into spirals (exponential disks), ellipticals ('de Vaucouleurs' profiles) and irregular galaxies which exhibited large residual images after the removal of disk or bulge profiles

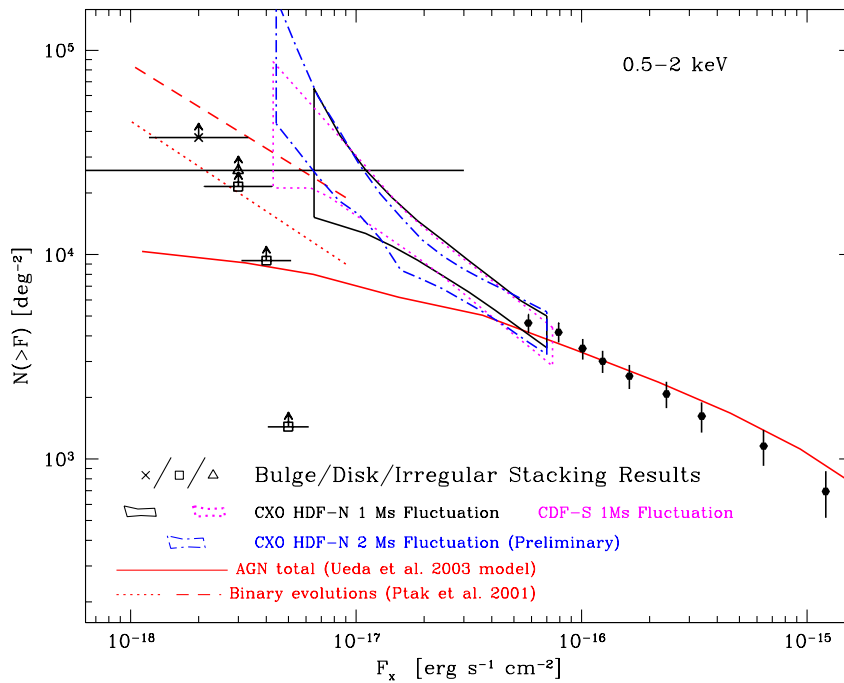


Figure 1. X-ray Number Counts from the Hubble/Chandra Deep Field North. The 1 Ms “fish-tail” fluctuation limits are from Miyaji & Griffiths (2002), and similar results were found from the HDF-S. Fluctuation limits from the 2Ms CDF-N are preliminary and possibly contaminated by cosmic-ray background events. Points showing stacked galaxies of different morphological types are all lower limits - stacking was done on optical galaxies in the HDF-N and the data points represent the average fluxes of the stacked galaxies. For any given morphological type, it is unlikely, however, that the number counts due to them are much higher than those shown here, unless contaminated by AGN. The prediction of AGN number counts is from Ueda et al. (2003). An estimate of the number counts from X-ray binary populations in normal galaxies was made by Ptak et al. (2001)

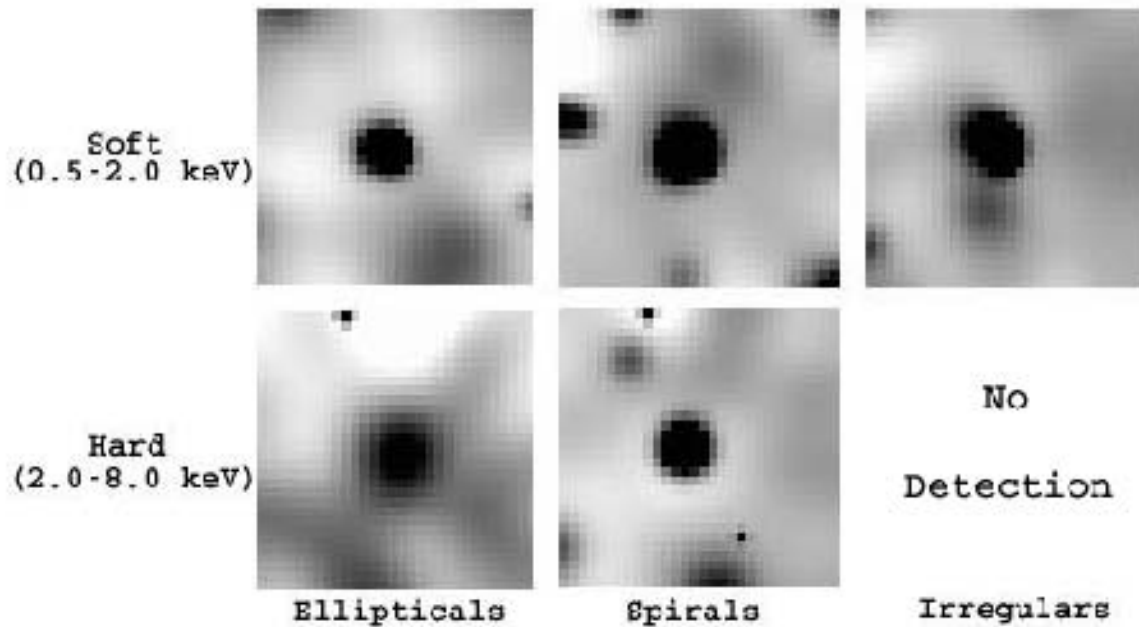


Figure 2. Stacked X-ray images of ensembles of galaxies

(Ratnatunga, Griffiths & Ostrander 1999). This survey showed, for example, that the fraction of irregulars rises from 12% locally to 30% at a redshift of 0.5.

We have applied this MDS software and analysis to the HST images of the HDF-N and other deep HST surveys. In those fields where we have deep CXO observations, we can then examine the X-ray images for the presence of X-rays from the galaxies of differing broad morphological type.

4. RESULTS OF ‘STACKING’

Although the fluctuations analysis gives us an indication of the number counts of X-ray sources at the faintest flux levels currently accessible, they do not give us any indication of the nature of the sources contributing to the fluctuations. How do we find out the possible nature of these sources? One method is that of ‘stacking’, i.e. the summation of sub-images centered on objects selected at another wavelength. Brandt et al. (2001) and Hornschemeier et al. (2002) have used this method on early CXO data of the HDF-N. In the HDF, we have the advantage of being able to use the HST images themselves to select various types of galaxies for the stacking process, using the software developed as part of the HST Medium Deep Survey (Ratnatunga, Griffiths and Ostrander 1999). We have now done this for elliptical, spiral and irregular galaxies, and some of the results are shown in figure 2.

As the figure shows, the spiral and elliptical galaxies are detected at high confidence in both the soft and hard energy bands, but the irregular galaxies are detected in the soft band only. The median redshifts are 0.87 for the 27 ellipticals, 0.49 for the 54 spirals and 1.55 for the 57 irregulars in these stacked images. Monte Carlo simulations have been used to verify the statistical confidence in these results.

The median X-ray luminosities are $x \times 10^{-17}$ ergs cm^{-2} s^{-1} for the ellipticals, $x \times 10^{-17}$ ergs cm^{-2} s^{-1} for the spirals and $x \times 10^{-17}$ ergs cm^{-2} s^{-1} for the irregulars, consistent with their B-band luminosities and the average values for L_X/L_B for the galaxy types.

5. X-RAY EVOLUTION OF GALAXIES

The observed X-ray evolution of spiral galaxies out to $z = 0.7$ is observed to be in excess of the expected value based on the evolution of binary X-ray populations. The observed evolution is better matched with a population of AGN such that the AGN luminosity is 0.1 of the galaxy luminosity in 30% of the galaxies at $z = 0.7$.

There are several problems which need to be solved or investigated in support of the interpretation of these results: (i) the evolution of low-mass X-ray binaries (LMXRB), (ii) the evolution of high-mass X-ray binaries (HMXRB),

(iii) the evolution in the number of ultraluminous X-ray (ULX) objects and (iv) SNR and hot gas components.

6. CONCLUSIONS

Results from the stacking analysis of normal galaxy populations applied to the CXO deep survey of the HDF-N show that normal galaxy populations are observable in these stacks out to redshifts of ~ 1 . The average X-ray fluxes observed in these stacks are consistent with the numbers and fluxes inferred from the fluctuation analysis of the CXO data. We conclude that the fluctuations are therefore caused primarily by normal galaxy populations and that such deep X-ray surveys will eventually allow us to constrain the evolution of the binary source populations within these galaxies, using the relationship between HMXB numbers and the SFR of nearby galaxies. We have tentative evidence for the presence of AGN in some fraction of normal spiral galaxies at moderate redshift.

7. ACKNOWLEDGEMENTS

We acknowledge support from NASA grants NAG5-9902, NAG5-10875 and subcontract 2247-CMU-NASA-1128 from PSU (under NAS8-00128).

REFERENCES

- Brandt, W. N., Hornschemeier, A. E., Schneider, D. P., Alexander, D. M., Bauer, F. E., Garmire, G. and Vignali, C. 2001, *Astrophys. J.* **558**, L5
- K. Ghosh, & N. White 2001, *Astrophys. J.* **559**, L97
- G. Hasinger et al. 2005, *Astron. & Astrophys. in press*
- A. E. Hornschemeier, Brandt, W. N., Alexander, D. M., Bauer, F. E., Garmire, G. P., Schneider, D. P., Bautz, M. W. and Chartas, G. 2002, *Astrophys. J.* **568**, 82
- A. E. Hornschemeier, and the CDF-N team 2003, *X-rays at Sharp Focus: ASP Conf. Series, eds. S. Vrtilek, E. M. Schlegel, L. Kuhl*
- T. Miyaji and R.E. Griffiths 2002, *Astrophys. J.* **564**, L5
- C. Norman et al. 2004, *Astrophys. J.* **607** 721
- A. Ptak and R. E. Griffiths 2001, *Astrophys. J.* **559**, L91
- K. Ratnatunga, R. E. Griffiths & E. J. Ostrander 1999, *Astron. J.* **118**, 86
- Ueda, Y., Akiyama, M., Ohta, K. & Miyaji, T. 2003, *Astrophys. J.* **598**, 886

ASTROPHYSICS WITH LOBSTER

R. Hudec¹, V. Šimon¹, L. Švéda², L. Pina², and A. Inneman³

¹Astronomical Institute, Academy of Sciences of the Czech Republic, CZ-251 65 Ondřejov, Czech Republic

²Czech Technical University, Faculty of Nuclear Physics, Prague, Czech Republic

³Center for Advanced X-ray Technologies, Reflex sro, Prague, Czech Republic

ABSTRACT

The paper deals with astrophysical aspects of wide-field X-ray telescopes with high sensitivity which prototypes have been designed, developed, and tested recently. They are expected to contribute essentially to study of various astrophysical objects such as AGN, SNe, Gamma-ray bursts (GRBs), X-ray flashes (XRFs), galactic binary sources, stars, cataclysmic variables, X-ray novae, various transient sources, etc.

Key words: X-ray telescopes, X-ray optics, All-Sky Monitor.

1. INTRODUCTION

The X-ray sky is highly variable, rich in variable and transient sources of both galactic as well as extragalactic origin. However, since many of these transient events cannot be predicted, and are relatively rare, very wide-field instruments are required. They must achieve high sensitivities and provide precise localizations in order to effectively study the objects. Wide field X-ray telescopes with imaging optics are expected to represent an important tool in future space astronomy projects in general, especially those for deep monitoring and surveys in X-rays over a wide energy range (Hudec et al. 2000, 2003, 2004a, 2004b). The Lobster-Eye wide field X-ray optics has been suggested in 70ies by Schmidt (Schmidt 1975, orthogonal stacks of reflectors) and by Angel (Angel 1979, array of square cells). Up to 180 deg field of view (FOV) may be achieved. This novel X-ray optics offers an excellent opportunity to achieve very wide FOV (1000 square degrees and more) while the widely used classical Wolter grazing incidence mirrors are limited to roughly 1 deg FOV (Priedhorsky et al. 1996, Inneman et al. 2000).

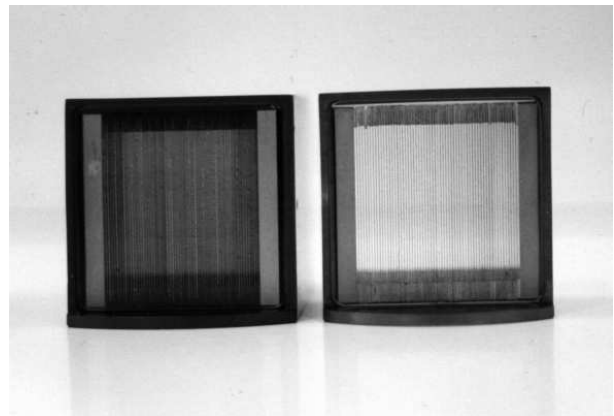


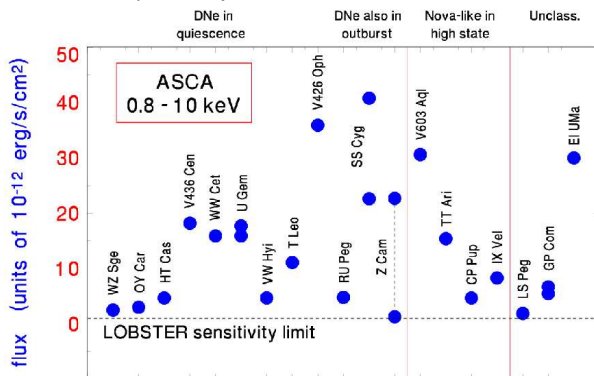
Figure 1. The Lobster Eye X-ray telescope prototypes (23 x 23 mm plates, 100 microns thick gold-coated glass foils, Schmidt arrangement) in front view.

SCIENCE WITH LOBSTER

Deep (limiting flux of 10^{-12} erg cm⁻²s⁻¹) can be easily achieved for daily scanning observation) X-ray sky monitoring with large FOVs (e.g. FOV of 6×180 deg can be easily assembled on the space station ISS, e.g. Sveda et al. 2004) is expected to contribute significantly to various fields of modern astrophysics. A few most important examples are listed below.

(1) Gamma Ray Bursts (GRBs). Detection rates of nearly 20 GRBs/year can be obtained for the prompt X-ray emission of GRBs, taking into account the expected GRB rate 300/year. (2) X-ray flashes. Detection rates of nearly 8 X-ray flashes/year are expected, assuming XRF rate of 100/year. (3) X-ray binaries. Because of their high variability in X-rays they will be one of major targets in LE observations. LE will be able to observe their short-time outbursts by long-term extended monitoring. Almost all galactic XRB are expected to be within the detection limits. (4) Stars. Because of the low X-ray luminosity of ordinary stars, only nearby stars are expected to be observable. We estimate the lower limit of ordinary stars ob-

Figure 2. Various types of cataclysmic variables within the sensitivity limit of LOBSTER ASM



servable by the LE telescope as 600. The sampling rate of LE observations will be sufficient enough to observe sudden X-ray flux increases during flares while still having the capability of monitoring the variability on time scales of years. (5) Supernovae. The LE telescope should be able to detect the theoretically predicted thermal flash lasting for ~ 1000 sec for the first time. Together with the optical SNe detection rate and estimates of the LE FOV we estimate the total number of SNe thermal flashes observed by the LE experiment to ~ 10 /year. (6) AGNs. Active Galactic Nuclei will surely be one of the key targets of the LE experiment. LE will be able to monitor the behavior of the large (~ 1000) sample of AGNs providing long-term observational data with good time sampling (hours). (7) X-ray transients. The LE experiment will be ideal to observe X-ray transients of various nature due to its ability to observe the whole sky several times a day for a long time with a limiting flux of about 10^{-12} erg cm $^{-2}$ s $^{-1}$. More and fainter X-ray transients are expected to be detected by the LE sky monitor enabling the detailed study of these phenomena. (8) Cataclysmic Variables. Cataclysmic Variables (CVs) are very active galactic objects, often showing violent long-term activity in both the optical and X-ray passband (outbursts, high/low state transitions, nova explosions) as well as rapid transitions between the states of activity. Search for the relation of the optical and X-ray activity is very important – monitoring of a large number of CVs is necessary to catch them in various states of activity. Most up to now X-ray observations of CVs: (i) Snapshots catching selected CVs in a particular state of activity, (ii) In most cases the transitions between the states are not covered, and (iii) Poor statistics of phenomena and objects (deeper studies available for only a few CVs). Important classes of CVs for LOBSTER are Non-magnetic dwarf novae (DNe), Super-soft X-ray sources (SSXSs), Classical novae (CNe), and Polars with soft X-ray excess.

CONCLUSIONS

Analysis and simulations of Lobster-eye X-ray telescopes have been carried out. They have indicated that

these innovative devices will be able to monitor the X-ray sky at an unprecedented level of sensitivity, an order of magnitude better than any previous X-ray all-sky monitor. Limits as faint as 10^{-12} erg cm $^{-2}$ s $^{-1}$ for daily scanning observation as well as the angular resolution < 4 arcmin in soft X-ray range are expected to be achieved allowing monitoring of all classes of X-ray sources, not only X-ray binaries, but also fainter classes such as AGNs, coronal sources, cataclysmic variables, as well as fast X-ray transients including gamma-ray bursts and the nearby type II supernovae. The various prototypes of both Schmidt as well as Angel arrangements have been produced and tested successfully, demonstrating the possibility to construct these lenses by innovative but feasible technologies. Both very small Schmidt lenses (3×3 mm) as well as large lenses (300×300 mm) have been developed, constructed, and tested. This makes the proposals for space projects with very wide field lobster eye optics possible for the first time.

ACKNOWLEDGMENTS

We acknowledge the support provided by the Ministry of Industry and Trade of the Czech Republic, FD-K3/052, and partly by the Grant Agency of the Academy of Sciences of the Czech Republic (A3003206) and Grant Agency of the Czech Republic (205/05/2167).

REFERENCES

- Angel J. R. P. 1979, *Astroph. J.*, 364, 233.
- Inneman A. et al. 2000, *Proc. SPIE*, 4138, 94.
- Hudec R. et al. 2000, *SPIE Proc.* 4012, 432.
- Hudec R. et al. 2003, *SPIE Proc.* 4851, 578.
- Hudec R. et al. 2004a, *SPIE Proc.* 5488, 449.
- Hudec R. et al. 2004b, *Nucl. Phys. B Proc. Suppl.* 132, 320.
- Priedhorsky, W. C. et al. 1996, *MNRAS* 279, 733.
- Schmidt, W. K. H. 1975, *NuclIM*, 127, 285.
- Sveda, L. et al. 2004, *SPIE Proc.* 5168, 393.

OPTICAL IDENTIFICATION IN THE XMM-NEWTON MARANO FIELD SURVEY

M. Krumpe¹, G. Lamer¹, A.D. Schwobe¹, S. Wagner², G. Zamorani³, M. Mignoli³, and R. Staubert⁴

¹Astrophysikalisches Institut Potsdam, An der Sternwarte 16, 14482 Potsdam, Germany

²Landessternwarte Heidelberg-Königsstuhl, 69117 Heidelberg, Germany

³Dipartimento Astronomia Bologna, Università di Bologna, Bologna, Italy

⁴Universität Tübingen, Institut für Astronomie und Astrophysik, 72076 Tübingen, Germany

ABSTRACT

We present optical follow-up observations of an overlapping raster of XMM-Newton observations with a total of 120 ksec good observation time in the Marano Field. The Marano Field was originally an 0.7 deg² optical quasar survey field. Among almost 700 X-ray sources we detected most of the optically selected quasars. We obtained VLT FORS1 and FORS2 multi-object spectroscopy and identified 99 new X-ray counterparts. Almost half of the new XMM-Newton sources are heavily absorbed sources which were typically identified with narrow line objects (type II AGNs) or optically normal galaxies. The X-ray identification completeness ratio of the area covered by VLT FORS1 and FORS2 data reaches 50%. Type I AGNs extend over a wide range of redshift ($0.4 < z < 2.8$) with a maximum at $z \sim 0.9 - 1.4$. Type I and type II AGNs are comparable in number up to $z = 1$. Type I AGNs are the dominant population at $z > 1$. However, we found 5 type II AGNs with significant cosmological redshifts of up to $z \sim 2.8$. All the X-ray emitting optically normal galaxies with high X-ray luminosities show hard X-ray spectra.

Key words: surveys; X-rays; galaxies: active; quasars.

1. INTRODUCTION

The Marano Field was named by an early optical quasar survey up to a limiting magnitude of $m_{B,J} = 22.0$ mag by Marano et al. (1988). Based on different selection techniques, they discovered 23 broad emission line quasars and defined a list of quasar candidates. Zitelli et al. (1992) completed this work by presenting a spectroscopically complete sample of quasars with $m_{B,J} \leq 22.0$ mag.

2. OPTICAL IDENTIFICATION OF THE X-RAY SOURCES

In the central Marano Field (0.28 deg²) we detected 525 X-ray sources out of which 475 are new detections ($f_X \geq 2 \times 10^{-15}$ erg cm⁻² s⁻¹), the remaining 50 have been already detected by ROSAT (56 ksec, $f_X \geq 3.7 \times 10^{-15}$ erg cm⁻² s⁻¹) Zamorani et al. (1999). Based on the literature 56 X-ray sources have been already identified with optical counterparts (La Franca et al., 2002; Gruppioni et al., 1999, 1997; Teplitz et al., 2003). In order to complete our sample we obtained VLT FORS1 and FORS2 multi-object spectroscopy for newly detected X-ray sources. We were able to identify a total of 83 new X-ray sources with optical counterparts ($m_R \leq 24.0$ mag) in the central region of the Marano Field. The breakdown of the identifications according to object classes is shown in Tab. 1.

object class	total number	percentage
type I AGNs	83	59.7 %
type II AGNs	38	27.3 %
galaxies (G)	9	6.5 %
stars (S)	9	6.5 %

Table 1. X-ray counterpart distribution of the central Marano Field

3. DISCUSSION

We identified different object classes as counterparts for the X-ray sources in the central Marano Field. Over 80% of the X-ray sources are AGNs. Fig. 1 shows the redshift distribution of different object classes. Type I AGN extend over a wide range of redshift with a maximum at $z \sim 0.9 - 1.4$. Type II AGN are detected at lower number density at low redshifts and peak at $z \sim 0.3$ and $z \sim 0.8 - 1.0$. We also classified five high redshifted type II AGN. The lack of type II AGNs between $z = 1.5 - 2.2$

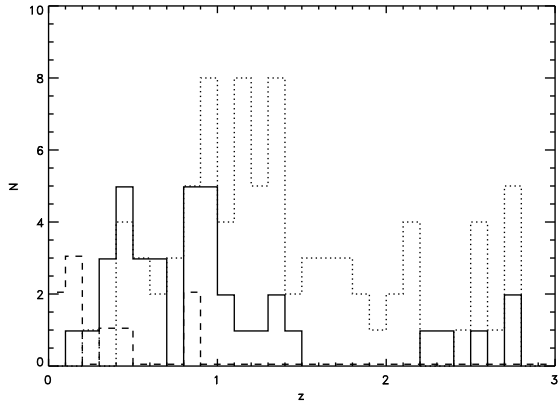


Figure 1. Redshift distribution of different object classes. Labels: dotted line - type I AGNs, solid line - type II AGNs, dashed line - galaxies.

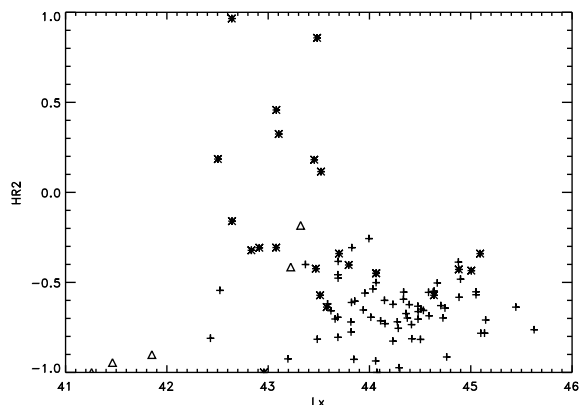


Figure 2. Hardness-ratio (0.5-2.0 keV & 2.0-4.5 keV) vs. X-ray luminosity (as observed). Plotted are objects with errors in hardness-ratio ≤ 0.3 . Labels: cross - type I AGNs, asterisks - type II AGNs, Triangle - galaxies.

is probably due to missing emission lines in the optical window. Taking this into account the redshifts are consistent with a flat distribution of type II AGN at $z > 1.0$. X-ray emitting galaxies are only found at low redshifts ($z < 0.9$).

In addition to classifying the optical counterparts we furthermore studied the properties of the different object classes that could be identified with X-ray sources.

All type I AGN in Fig. 2 show high X-ray luminosities and soft X-ray spectra. The unabsorbed type I AGNs vary just over a small range in hardness-ratio. In contrast, type II AGN and X-ray emitting galaxies show lower X-ray luminosities and very hard X-ray spectra. However, their hardness-ratio differs from extremely obscured objects to almost unobscured objects (see Fig. 2). Nevertheless, the majority of type II AGNs and X-ray emitting galaxies show only narrow line emissions from outside the central region. Type II AGN are optically fainter and redder than type I AGN (see Fig.3). The optical spectrum of X-ray

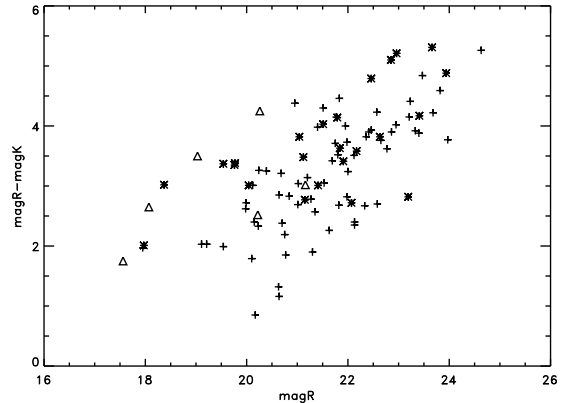


Figure 3. Colour magnitude diagram of identified X-ray sources. Labels: cross - type I AGNs, asterisks - type II AGNs, Triangle - galaxies.

bright optically normal galaxies, so called "XBONGS", indicates nothing that points towards an AGN. The AGN inside this galaxy is so heavily absorbed that all optical line emissions are completely obscured. This is also indicated by the hard spectra of XBONGS. Interestingly, XBONGS do not stick out as a separated object class in a hardness-ratio–X-ray luminosity diagram. They share most of the X-ray properties of type II AGNs.

4. ACKNOWLEDGEMENTS

Mirko Krumpke is supported by the Deutsches Zentrum für Luft- und Raumfahrt (DLR) GmbH under contract No. FKZ 50 OR 0404.

REFERENCES

- La Franca, F., Fiore, F., Vignali, C. et al. 2002, ApJ, 570, 100
- Gruppioni, C., Mignoli, M., Zamorani, G. 1999, MNRAS, 304, 199
- Gruppioni, C., Zamorani, G., de Ruiter, H.R. et al. 1997, MNRAS, 286, 470
- Marano, B., Zamorani, G., Zitelli, V. 1988, MNRAS, 232, 111
- Teplitz, H.I. Collins, N.R., Gardner, J.P. et al. 2003 ApJS, 146, 209
- Zamorani, G., Mignoli, M. Hasinger, G. et al. 1999 A&A, 346, 731
- Zitelli, V., Mignoli, M. Zamorani, G. et al. 1992, MNRAS, 256, 349

GASEOUS ABUNDANCES IN M82

P. Ranalli¹, L. Origlia², A. Comastri², R. Maiolino³, and K. Makishima^{1,4}

¹RIKEN, Cosmic Ray Laboratory, 2-1 Hirosawa, Wakoshi, Saitama, 351-0106 Japan; JSPS fellow

²INAF, Osservatorio Astronomico di Bologna, via Ranzani 1, 40127 Bologna, Italy

³INAF, Osservatorio Astrofisico di Arcetri, L.go E. Fermi 5, 50125 Firenze, Italy

⁴Department of Physics, The University of Tokyo, 7-3-1 Hongo, Bunkyo-ku, Tokyo 113-0033

1. INTRODUCTION

The signature of the star formation (SF) history of a galaxy is imprinted in the abundance patterns of its stars and gas. Determining the abundance of key elements released in the interstellar medium (ISM) by stars with different mass progenitors and hence on different time scales, will thus have a strong astrophysical impact in drawing the global picture of galaxy formation and evolution (McWilliam, 1997, ARA&A, 35, 503). It also offers the unique chance of directly witnessing the enrichment of the ISM (Maeder & Conti, 1994, ARA&A, 32, 227). Metals locked into stars give a picture of the enrichment just prior to the last burst of SF, while the hot gas heated by SNe II explosions and emitting in the X-rays should trace the enrichment by the new generation of stars.

We have started a project to measure the metallicity enhancement in a sample of starburst galaxies, for which we obtained high resolution infrared (J and H band) spectra with the 3.6 m Italian Telescopio Nazionale Galileo (TNG) and with the ESO VLT, and both proprietary and archival data from the XMM-Newton and Chandra missions. Our sample comprises M82, NGC253, NGC4449, NGC3256 and the *Antennae*, sampling two orders of magnitude in star formation, as it ranges from the 0.3 M_{\odot}/yr of NGC4449 to the $\sim 30M_{\odot}/\text{yr}$ of the *Antennae* and NGC3256.

Preliminary results for M82 were achieved with the available XMM-Newton archival data, and hinted for a confirmation of the expected scenario in which the gaseous component has a higher content of α -elements than the stellar one, and a similar content of Fe (Origlia et al., 2004, ApJ 606, 862). However, some new issues were posed, since we found a very low abundance of O and Ne with respect to other α -elements (e.g., O/Mg ~ 0.2 , Ne/Mg ~ 0.3) in the hot gas present in the central ($< \sim 1$ kpc) regions of M82, which could not be satisfactorily explained. Thus we were granted a deeper observation of M82, whose preliminary results are presented in the following.

2. MAPPING THE CHEMICAL ELEMENTS THROUGH NARROW-BAND IMAGING

The MOS and PN cameras onboard XMM-Newton have a moderate energy resolution (FWHM $\sim 70 - 80$ eV at 1 keV), which allows the use of narrow-band imaging to infer the distribution of chemical elements throughout the galaxy. Among the most prominent spectral lines lying around ~ 1 keV, we consider here the Ne X line at 10 \AA because this element, together with O, posed the main problems in our previous work. Unfortunately, it is not possible to consider lines from O, since the MOS resolution is rapidly degraded at energies $< \sim 0.6$ keV, and the enlargement of the band needed to take account of the instrumental effects would make an image in the O band seriously contaminated by continuum emission.

In order to extract information about abundances, the line-band images should be normalized by accounting for the continuum emission. We perform this correction by dividing each line-band image by a smoothed 0.5–2.0 keV band image. Results from spatially-resolved spectroscopy confirmed that once this correction is applied, the line-band images do trace the chemical abundances.

Fig. 1 (left panel) shows the Ne abundance distribution map with superimposed contours from 0.5–2.0 keV emission. Ne is clearly concentrated in two separated regions, north and south of the galaxy center.

3. SPATIALLY RESOLVED SPECTROSCOPY

We present here the preliminary analysis conducted on the southern outflow, making use of EPIC data. We divided the southern outflow in five regions, in order to study the different properties of the hot gas as it flows and/or is heated from the central starburst towards the intergalactic space. The regions are numbered from S1 to S5 with increasing height above the galactic plane, and are shown in Fig. 1 (right panel). The spectra were extracted from the

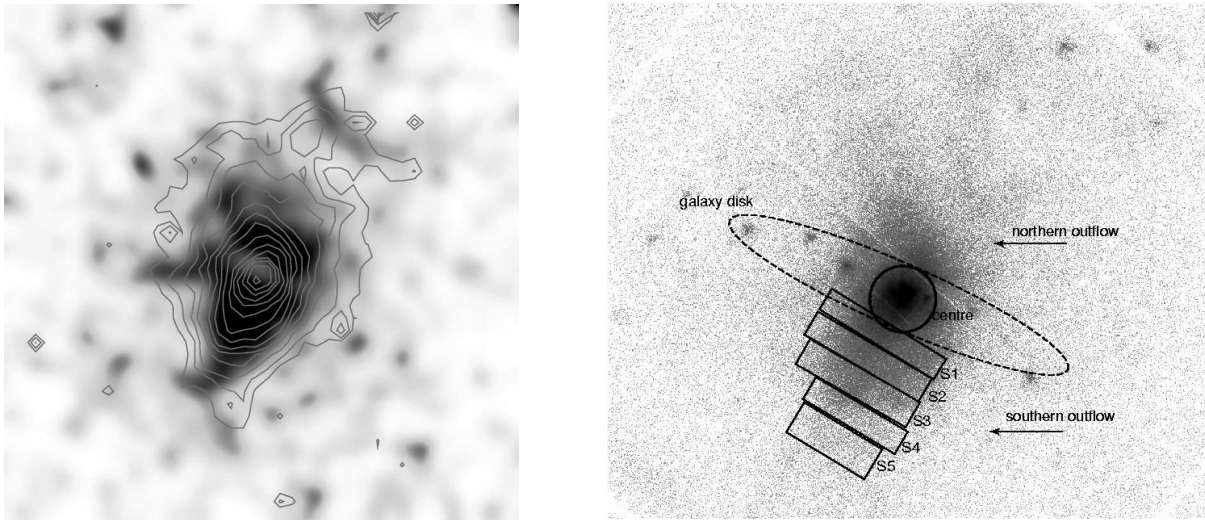


Figure 1. **Left:** *Ne X* abundance map. Gray scale: line/continuum flux ratio, tracking *Ne* abundance; darker means more abundant. Contours: 0.5–2.0 keV emission. **Right:** Image of 0.5–10 keV emission with a sketch of the regions used in the spectroscopical analysis.

Table 1. Chemical abundances in different regions with 90% errors. The abundances are given in solar units, i.e. Fe/Fe_{\odot} , following the Grevesse & Sauval (1998, *Sp.Sci.Rev.* 85, 161) scale. Region S4 is not shown since it falls mainly on CCD gaps. The “stars” region shows the results from infrared spectroscopy, while the “centre” region is referred to the PN+RGS data analysis in Origlia et al. (2004). The average height above the galactic plane is reported, assuming a distance of 2.94 Mpc (de Vaucouleurs et al., “Third reference catalogue of bright galaxies”, 1991, assuming $H_0 = 70$).

region	height (kpc)	Fe	O	Ne	Mg	Si	S
centre		$0.43^{+0.12}_{-0.08}$	$0.26^{+0.15}_{-0.09}$	$0.45^{+0.17}_{-0.12}$	$1.36^{+0.32}_{-0.26}$	$1.49^{+0.32}_{-0.26}$	$1.42^{+0.48}_{-0.40}$
S1	0.6	0.48 ± 0.01	0.57 ± 0.04	0.85 ± 0.05	1.33 ± 0.04	1.12 ± 0.05	0.75 ± 0.10
S2	1.0	0.57 ± 0.02	0.64 ± 0.04	1.26 ± 0.07	1.73 ± 0.07	1.33 ± 0.09	0.75 ± 0.17
S3	1.5	0.88 ± 0.04	1.04 ± 0.07	2.21 ± 0.14	3.06 ± 0.15	2.06 ± 0.17	1.29 ± 0.33
S5	2.5	0.78 ± 0.08	1.71 ± 0.16	3.31 ± 0.35	4.09 ± 0.48	2.65 ± 0.74	$0.53^{+1.93}_{-0.53}$
stars		0.5 ± 0.2	$1.0^{+0.5}_{-0.3}$	—	$1.1^{+0.4}_{-0.3}$	$1.1^{+1.0}_{-0.5}$	—

MOS (0.5–8.0 keV) and PN (1.0–9.0 keV) data, and fitted with a multi-temperature “mekal” thermal plasma model whose differential emission measure (DEM) is described by a 6th order polynomial in the 0.1–10 keV energy range. Background spectra were extracted from the blank-sky data files (Read & Ponman, 2003, *A&A*, 409, 395) after normalization to the background levels observed in the M82 data.

The best-fit chemical abundances are shown in Table 1 along with results from our previous paper (Origlia et al., 2004, *op. cit.*) relative to X-ray (EPIC and RGS) and infrared data for the central regions, marked in the Table as “centre” and “stars”, respectively. No significant changes are found in the temperature of the plasma. The only region whose spectra require absorption in excess of the Galactic value is S1. Our previous finding, that the inner region of M82 is somewhat devoid of the lighter α -element, is thus confirmed. Moreover, it is found that these elements are rather to be concentrated in the outflow. On the other hand, the heavier elements (Mg, Si, S) while following a similar spatial pattern seem to be more evenly distributed.

4. DISCUSSION

In M82 both the hot gas and the stellar phases trace a very similar Fe abundance. Indeed, since Fe is mainly produced by type Ia supernovae (SN), it is expected to be released in the ISM only after ~ 1 Gyr from the local onset of star formation. At variance, α -element (O, Ne, Mg, Si, S) are predominantly released by type II SN with massive progenitors on much shorter time scales. The overall α -element/Fe enhancement in the innermost region of M82 is consistent with a standard chemical evolution scenario only for heavier elements (Mg, Si, S).

However, the lighter elements (O, Ne) show a different distribution, in which the inner regions of the galaxy appears somewhat devoid of these metals, while in outer parts of the outflow they are found to be enhanced as the heavier α -element. When the entire sample of galaxies will be analyzed, we will better understand whether the bipolar distribution of O and Ne is peculiar of M82 or is a common feature in starburst galaxies.

XMM-NEWTON AND DEEP OPTICAL OBSERVATIONS OF THE OTELO FIELDS: THE GROTH-WESTPHAL STRIP

Miguel Sánchez-Portal¹, Ana M. Pérez-García², Jordi Cepa^{2,3}, Emilio Alfaro⁴, Héctor Castañeda², Jesús Gallego⁵, J. J. González-González⁶, and J. Ignacio González-Serrano⁷

¹Herschel Science Centre - INSA/ESAC, P.O. Box 50727, Madrid 28080, Spain

²Instituto de Astrofísica de Canarias, E-38205, La Laguna, Tenerife, Spain

³Universidad de La Laguna, La Laguna, Tenerife, Spain

⁴Instituto de Astrofísica de Andalucía (CSIC), Granada, Spain

⁵Departamento de Astrofísica, Universidad Complutense de Madrid, Spain

⁶Instituto de Astronomía, UNAM, México DF, México

⁷Instituto de Física de Cantabria, CSIC-UNICAN, Santander, Spain

ABSTRACT

We present a preliminary analysis of public EPIC data of one of the OTELO targets, the Groth-Westphal strip, gathered from the XMM-Newton Science Archive (XSA). EPIC images are combined with optical *BVRI* data from our broadband survey carried out with the 4.2m WHT at La Palma.

Key words: X-rays: surveys; X-rays: background; AGN; galaxies: morphology.

1. THE OTELO PROJECT AND ITS SCIENCE

OTELO (Cepa et al., 2003) will search for emission line objects using OSIRIS tunable filters at the 10m GTC telescope in La Palma in selected atmospheric windows (centred at the H_{α} line at $z = 0.24$ and $z = 0.4$) that are relatively free of sky emission lines. A total area of more than one square degree will be observed. The survey technique will allow for separation of the H_{α} and [NII] lines and therefore AGNs from starburst galaxies. A 5σ depth of 8×10^{-18} erg cm⁻² s⁻¹ will make OTELO the deepest emission line survey to date. OTELO science includes the evolution of galaxies, the evolution of star formation in the Universe, chemical evolution of galaxies, QSO spatial density determination, AGN evolution, the low-end of the galaxy luminosity function, galactic Astronomy etc. A complementary optical broadband survey is currently on-going (morphology, photometrical redshifts). It is intended to complement the optical survey with other ground or space-based facilities, from X-rays (XMM-Newton, Chandra) to FIR and sub-mm (Herschel, GTM). The present work is being performed in the framework of the multiwavelength study of the OTELO fields.

2. OBSERVATIONS AND DATA REDUCTION

XMM-Newton observations of the Groth-Westphal strip (Groth et al., 1994) were collected from the XMM Science Archive (XSA). The EPIC observations were re-processed using SAS v6.0.0 `emproc` and `epproc` standard procedures. High-radiation intervals were removed by inspecting the count rate curves. GTI files were created by means of the `tabgtigen` SAS task. These files were further included in standard filtering expressions. The observations were co-added by means of the SAS `merge` procedure. Attitude files were also merged. Final exposure times were about 82 ksec and 70 ksec in MOS and PN, respectively. Three energy bands were defined: 0.5 - 2 keV (soft band), 2 - 4.5 keV (medium band) and 4.5 - 10 keV (hard band). Sources were detected by means of the `edetect_chain` SAS procedure. We imposed a likelihood parameter $ML = -\ln(1 - P) > 14$, where P is the probability that the source exists. Furthermore, we considered only those sources for which $flux/err_{flux} > 2$, lying within the optical FOV. We have detected 75 sources fulfilling these conditions. Two hardness ratios have been also computed by this SAS procedure.

Optical *BVRI* observations were carried out at the prime focus of the 4.2m William Herschel Telescope (WHT) of the Observatorio del Roque de los Muchachos (La Palma). Image size is $16' \times 16'$ with a plate scale of 0.24 arcsec/pixel. Total exposure time at each of the three pointing directions is 9000 sec per filter. Reduction process followed standard steps using IRAF packages. Photometric calibration was obtained with several Landolt standard fields. Absolute astrometry was performed using the USNO B1 catalogue. Sources were extracted using SExtractor 2.2 (Bertin & Arnouts, 1996). The 50% detection level is 25.3 in B, 25.3 in V, 24.7 in R and 23.5

in I. Details on the optical observations can be found in Pérez-García et al. (in preparation).

3. SOURCE DETECTION

We have matched X-rays and optical sources by searching in $6'' \times 6''$ boxes centred in the X-rays coordinates. Upon comparison with published Chandra coordinates (Nandra et al., 2004) we found a bulk shift of $\langle \Delta\alpha \rangle = 4.5''$ and $\langle \Delta\delta \rangle = -2.7''$. After correcting for this global image shift, we found: (a) Unique match in all photometric bands for 43 sources (57.3%); (b) partial match (not detected in all bands) for 10 sources (13.3%); (c) multiple match for 10 sources (13.3%); (d) partial match + multiple match for 2 sources (2.7%); and (e) No optical counterpart found for 10 sources (13.3%)

4. RESULTS

Since photometric redshift values are still not available, we have concentrated our analysis in distance-independent parameters, as described below.

4.1. X/O Ratio Analysis

The X-rays to optical flux ratio (X/O) is a powerful means to discriminate between different classes of X-rays sources (Fiore et al., 2003; Della Ceca et al., 2004). Figure 1 shows a diagnostic diagram combining the 0.5–4.5 keV to optical R-band flux ratio and one of the hardness ratios. The dashed-dotted line corresponds to $X/O = 0.1$, typical of coronal-emitting stars, normal galaxies and heavily absorbed AGNs. Five of our sources (11.6%) lie below this line, and therefore are likely either normal galaxies or Compton-thick AGNs. The dashed-line box corresponds to the region containing the 85% of the optically identified broad-line AGNs in the XMM-Newton Bright Source Sample (BSS) (Della Ceca et al., 2004). 29 of our sources (67.4%) fall within the broad-line AGN region defined by this box. Objects with harder HR and large X/O (i.e. those to the right of the broad-line box) are likely narrow-line AGNs, according to the BSS and HBSS diagnostics from Della Ceca et al. (2004).

4.2. B/T Relation

We have derived the B/T (bulge-to-total luminosity) relation for the sample objects, comparing its distribution with a sample of active galaxies in the local Universe (Sánchez-Portal et al., 2004), as shown in figure 2. While not incompatible, B/T distributions are likely different, as proven by means of a K-S test: null hypothesis (that both samples are drawn from the same distribution) significance is only 17%. If we exclude LINERs from the local

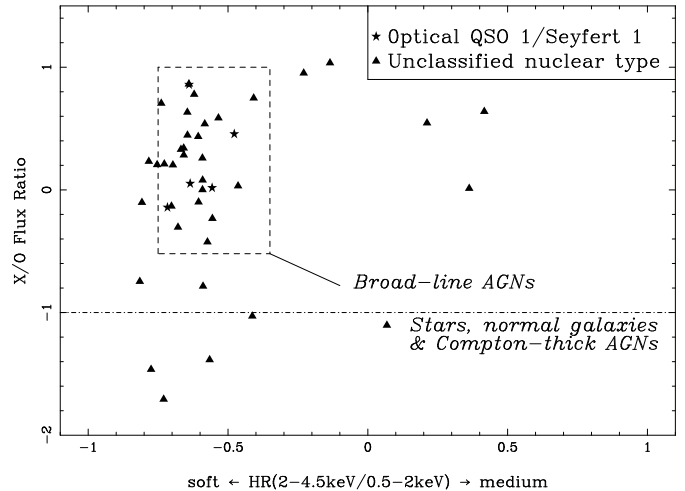


Figure 1. X/O relation vs. hardness ratio

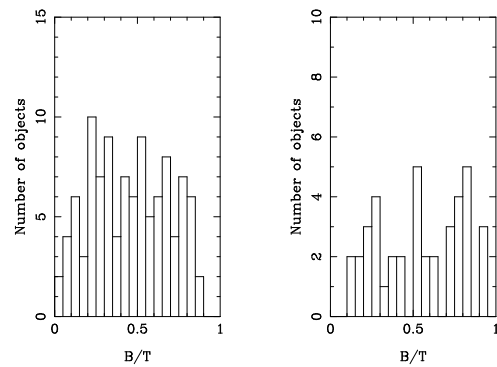


Figure 2. B/T relation in the local Universe (left) and in the X-rays selected sample

Universe sample (i.e. considering only Seyfert galaxies), the null hypothesis significance is higher but still reduced, 39%. The X-rays selected sample tends to higher B/T values and lacks very low B/T objects (generally present in latest Hubble types, $T \geq 4$). Finally, we don't find any correlation between X-rays hardness ratios and the B/T ratio.

REFERENCES

- Bertin and Arnouts 1996, A&AS 117, 393
- Cepa, J. et al., 2003 Rev. Mexicana Astron. Astrofis. (Serie de Conferencias), 16, 64
- Della Ceca, R. et al. 2004, A&A 428, 383
- Fiore, F. et al. 2003, A&A 409, 79
- Groth, E., et al. 1994, BAAS 185, 5309
- Nandra K., et al. 2005, MNRAS 356, 568
- Pérez-García, A. M., et al., in preparation
- Sánchez-Portal, M. et al., 2004, MNRAS, 350, 1087

2DF-XMM WIDE ANGLE SERENDIPITOUS SURVEY

J.A. Tedds¹, M.J. Page², and XMM-Newton Survey Science Centre³

¹Department of Physics & Astronomy, University of Leicester, Leicester LE1 7RH, UK

²Mullard Space Science Laboratory, UK

ABSTRACT

The XMM-Newton Survey Science Centre (SSC) is carrying out an identification and follow-up programme of serendipitous sources discovered in XMM-Newton observations. The goals of this survey include the detailed characterisation of the dominant X-ray source populations, e.g. AGN luminosity functions, absorption distribution and evolution, and the relationship between optical emission line and X-ray spectral properties. In addition to our ongoing core XID spectroscopic identification programme, we have now targetted over 3000 sources, spread evenly over 3 decades in X-ray flux, with the 2dF multi-fibre spectroscope on the AAT in 27 pointings, including the LSS survey fields. Critically we have now identified over 1000 sources with $F_{0.5-4.5keV} \geq 10^{-14}$ ergs⁻¹cm⁻² over a very large area > 15 deg² which is an unsurpassed resource with which to investigate the AGN population around the break in the X-ray source counts. We highlight the discovery of new and rare classes of sources such as BAL QSOs not seen in either the ROSAT wide area survey or current pencil beam X-ray surveys.

Key words: Surveys; X-rays.

1. SSC XID PROGRAMME

The SSC XID programme aims to provide statistical identifications for the whole of the XMM-Newton serendipitous catalogue (Watson et al. 2003). To achieve this we have undertaken a core programme to obtain spectroscopic IDs for ~ 1000 sources in a high b medium sample ($\sim 10^{-14}$ ergs⁻¹cm⁻²) in the North (AXIS, e.g. Barcons et al. 2002) and this 2dF sample in the South to identify the bulk of objects contributing to the X-ray background. A high b bright sample $\sim 10^{-13}$ ergs⁻¹cm⁻² has been completed by Della Ceca et al. (2004) and a Galactic Plane Sample ($\sim 7 \times 10^{-15}$ ergs⁻¹cm⁻²) is also underway (PI Motch). Deep optical imaging programmes are also being undertaken with the INT WFC (Yuan et al. 2003) and the ESO WFI (Dietrich et al. 2005) to provide photometric identifications

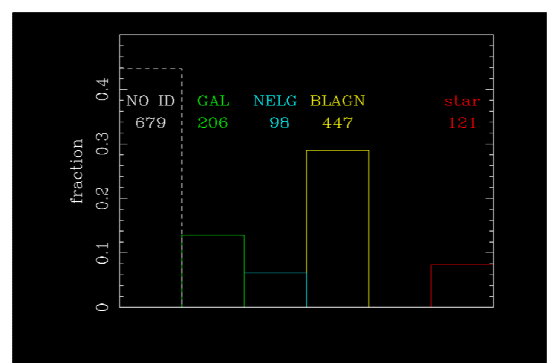


Figure 1. Provisional histogram of 2dF optical identifications.

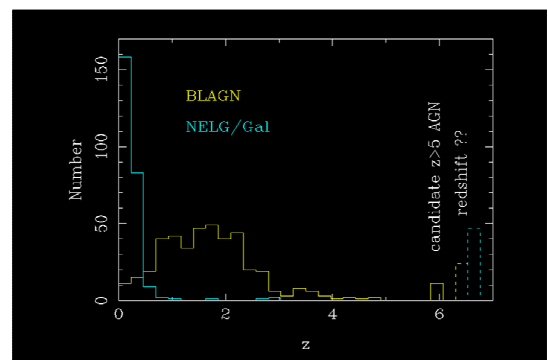


Figure 2. Provisional 2dF redshift distribution by optical class.

and redshifts for a much larger number of XMM-Newton fields and this includes $\frac{1}{2}$ of the 2dF sample to date.

2. 2DF OBSERVATIONS

We have obtained 2dF optical multi fibre spectroscopy in 27 pointings at the AAT (South) covering 68 XMM fields and including the LSS survey fields. Exposures were typically 1 hour and any X-ray source with an optical counterpart that could be allocated a fibre was ob-

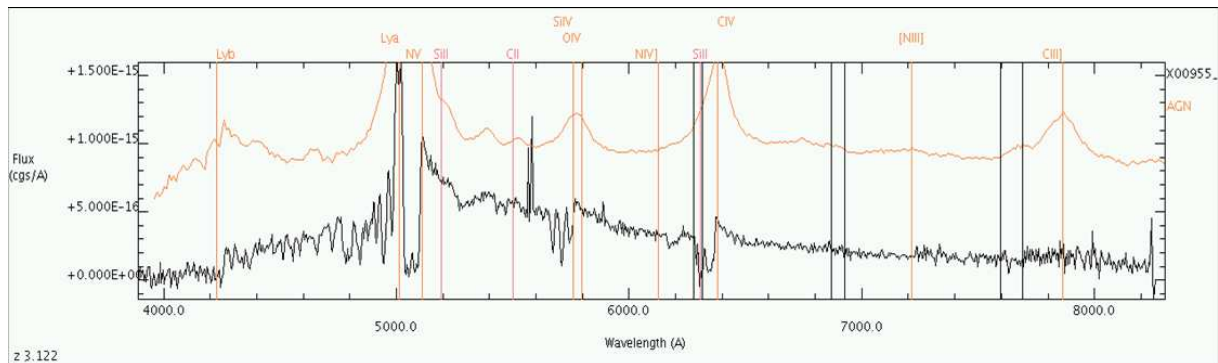


Figure 3. 2dF spectrum of a rare $z=3.122$ X-ray selected BAL QSO.

served, prioritised according to X-ray to optical offset on the sky. The identification stage is complete and we have beaten the barrier of 1000 sources brighter than $F_{0.5-4.5\text{keV}} \geq 10^{-14} \text{ ergs}^{-1}\text{cm}^{-2}$. In total ≥ 3000 X-ray sources have been observed and reduced. This opens up unique areas of parameter space.

3. PROVISIONAL 2DF ID STATISTICS

Figure 1 shows provisional identification statistics for $\sim 50\%$ of the final sample covering an area of $\sim 8\text{deg}^2$. The identification rate is $\geq 50\%$ having definite or probable IDs. Identification classes are simply based on optical properties alone, i.e. broad line AGN (BLAGN), absorption line galaxies (GAL), narrow emission line galaxies (NELG) and stars. Figure 2 shows the distribution of redshifts and highlights the outstanding feature of this survey which is that our wide coverage and large sample size gives us many more of the statistically rare objects at higher redshift than the pencil beam deep surveys.

4. UNIQUE SCIENCE EXAMPLE: SERENDIPITOUS BAL QSOS

Broad absorption line QSOs were virtually absent in previous X-ray surveys because of absorption. Indeed none were found in ROSAT surveys! We have already identified ≤ 20 BALQSOs in ~ 1000 QSOs which is $\sim 2\%$ of the X-ray QSO population and $\frac{1}{3}$ of the fraction found in past optical surveys. This is surprisingly large but is consistent with more recent SDSS results in which $\sim 15\%$ of the optical QSO population, $1.7 \leq z \leq 3.5$, are BALQSOs (Reichard et al. 2003). Figure 3 is an example 2dF spectrum of an X-ray detected, $z=3.122$ BAL QSO. X-ray selected objects will have the lowest X-ray absorption of the BALQSO population so we will study e.g. if their optical absorption lines are typical of the optically selected population and measure X-ray column densities.

5. X-RAY HR AND STACKING ANALYSIS

We have reprocessed over 100 XMM exposures for the 2dF fields using a test 2XMM catalogue pipeline and have made a catalogue which allows selection of objects by e.g. X-ray Hardness Ratio (HR). We can also select 2dF subsamples such as TyI or TyII QSOs by optical type and stack their X-ray spectra. There are ≥ 150 BLAGN having total EPIC counts ≥ 200 and we will present a stacked and rebinned spectrum (z -corrected 0.1keV bins) and hence determine mean power law continuum fits and resolve the presence of any residual Fe lines.

6. F_X - F_{OPT} CORRELATIONS

We have correlated our X-ray catalogue to SuperCOSMOS R,B mags and the XID WFC/WFI multiband imaging will probe up to 2 mags deeper than SDSS to $i \leq 23$ for $\frac{1}{2}$ of the 2dF sample to date. Initial studies suggest we may obtain photometric identifications and redshifts for up to $\sim 80\%$ of the final sample in this way. We want to explore the space density of $z \sim 4$ QSOs in X-ray surveys - do they decline at $z \geq 2$ in the same way that optical QSOs do? Finally this sample provides an excellent statistical ID training sample so that most XMM catalogue objects can in future be identified statistically based on their X-ray properties alone.

REFERENCES

- Barcons X. et al. 2002, A&A, 382, 522
- Della Ceca R. et al. 2004, A&A, 428, 383
- Dietrich J. et al. 2005, astro-ph, 0510223
- Reichard T. et al. 2003, AJ, 126, 2594
- Watson M.G. et al. 2003, AN, 324, 89
- Yuan et al. 2003, AN, 324, 178

AGN UNIFICATION AND THE X-RAY BACKGROUND

Ezequiel Treister^{1,2}, C. Megan Urry¹, and Paulina Lira²

¹Department of Astronomy, Yale University

²Departamento de Astronomía, Universidad de Chile

Abstract

The Great Observatories Origins Deep Survey (GOODS) combines deep HST and Spitzer imaging with the deepest Chandra/XMM observations to probe obscured AGN at higher redshifts than previous multiwavelength surveys. We present a self-consistent implementation of the AGN unification paradigm, which postulates obscured AGN wherever there are unobscured AGN, to successfully explain the infrared, optical, and X-ray number counts of X-ray sources detected in the GOODS fields. Assuming either a constant ratio of obscured to unobscured AGN of 3:1 (the local value), or a ratio that decreases with luminosity, and including Compton-thick sources, we can explain the spectral shape and normalization of the extragalactic X-ray “background” as a superposition of unresolved AGN, predominantly at $z \sim 0.5$ -1.5 and $L_x \sim 10^{43}$ - 10^{44} ergs/s. The possible dependence of the obscured to unobscured ratio with redshift is not well constrained; present data allow it to decrease or increase substantially beyond $z \sim 1$.

Method

The two main ingredients used to predict the AGN number counts and contribution to the X-ray background are: (i) The AGN luminosity function and its evolution. We used the luminosity function of Ueda et al. (2003), which is based on hard X-ray observations and thus relatively free of bias against obscured AGN. (ii) The AGN SED, in terms of intrinsic luminosity and neutral hydrogen column density (N_H) along the line of sight. We assumed an underlying power-law X-ray spectrum ($E > 0.5$ keV) with photon index of Γ 1.9, typical of unobscured AGN. In the optical ($\lambda = 0.1$ -1 microns), we used the Sloan Digital Sky Survey Composite Quasar Spectrum (Vanden Berk et al., 2001) plus Milky-Way-type reddening laws and a standard dust-to-gas ratio to convert N_H to A_V . An L^* elliptical host galaxy was then added to the resulting optical spectrum. In the infrared ($\lambda > 1$ micron) we used dust emission models by Nenkova et al. (2002) with the corresponding conversion from N_H value to viewing angle. AGN models with the same intrinsic luminosities were normalized at 100 microns. The standard X-ray to optical luminosity ratio was used to fix the scale of the different models.

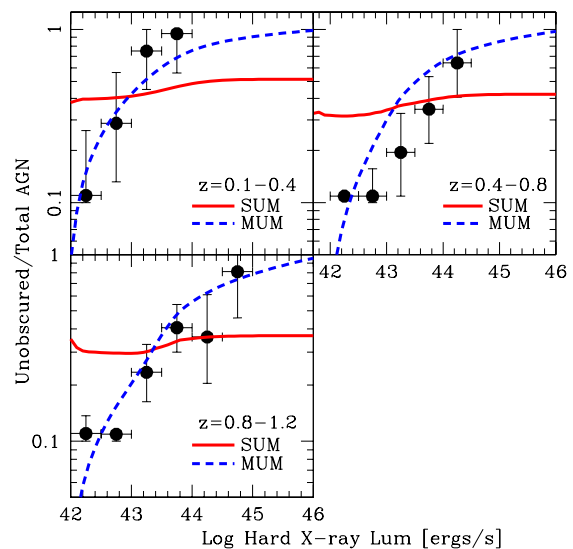


Figure 1. Unobscured AGN ratio as a function of hard X-ray luminosity. Filled circles: data from Barger et al. (2005) combined with our sample. (Solid lines:) Ratio predicted by our simple unified model. The discrepancy between predictions and observations is very clear. In this redshift range, the discrepancy cannot be attributed to selection effects since the observed sample is mostly complete both for obscured and unobscured AGN. Therefore, we also used a modified unified model (Dashed lines) in which the obscured-to-unobscured AGN ratio decreases linearly with luminosity.

Summary

Using the simplest AGN unification model we have explained the spectral shape and intensity of the X-ray background. This is the first demonstration that a model assuming a constant ratio of obscured to unobscured AGN, independent of redshift or luminosity, can simultaneously explain the observed X-ray background and the optical and X-ray counts of AGN detected in deep X-ray surveys (Treister et al., 2004). At the same time, a model that incorporates a changing ratio with luminosity, as suggested by recently available observations (Fig. 1), can also successfully explain the X-ray background properties (Treis-

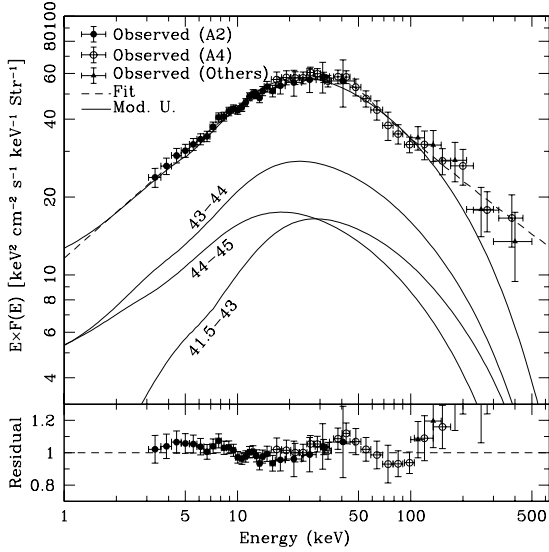


Figure 2. X-ray background population synthesis for an AGN unification model in which the fraction of obscured AGN decreases with increasing luminosity (solid line). The agreement with observations (data points, dashed line) is very good, with a reduced χ^2 of 0.648. Labeled solid lines show the contribution from sources in different X-ray luminosity bins. The maximum contribution to the X-ray background comes from sources with $\log LX=43-44$, that is, moderate luminosity AGN.

ter & Urry, 2005), as shown in Fig. 2.

The integral constraint of the X-ray background clearly does not provide a sensitive probe of the fraction of the obscured AGN; other observations, in particular a high-flux X-ray sample ($\gtrsim 10^{-14}$ erg cm $^{-2}$ s $^{-1}$) with a very high spectroscopic completeness level ($>90\%$), is needed to test whether the ratio depends on redshift, i.e., whether the evolution of obscured and unobscured AGN is different. As shown in Fig. 3, unification by orientation — in which obscured and unobscured AGN have the same evolution — is consistent with the data. In order to obtain this highly complete sample, accurate redshifts for sources with optical magnitudes $24 \lesssim R \lesssim 27$ are needed. This is impossible with current state-of-the-art 8m-class telescopes. However, good photometric redshifts using medium-band filters down to these magnitudes are possible and will allow to solve the redshift dependence problem.

The resolved fraction of the X-ray background is $\lesssim 50\%$ in the 7-10 keV band and decreases with increasing energy. If the unification model presented here is correct, $\sim 50\%$ of AGN are currently missed by deep *Chandra* or *XMM* surveys. These are very obscured AGN that will be detected only by hard X-ray observatories, like the Black Hole Finder probe, at X-ray energies where the effects of dust obscuration are negligible. These surveys will detect a large fraction of the most obscured AGN, providing for the first time an unbiased census of the black hole activity

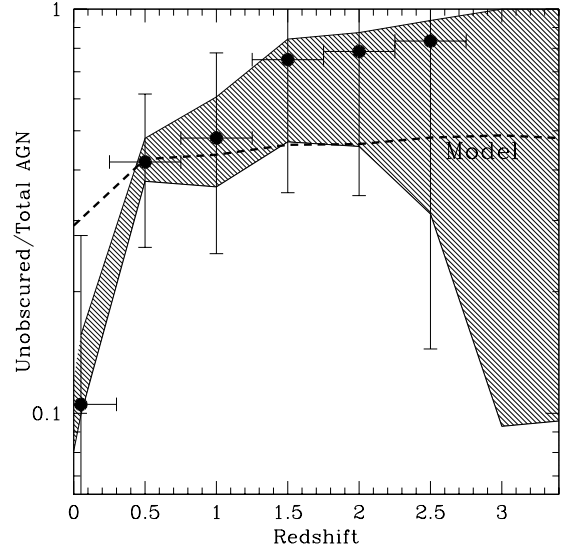


Figure 3. Ratio of unobscured-to-total AGN as a function of redshift. Circles: Observed data points from a sample compiled from several X-ray surveys for which the total spectroscopic completeness level is 66%. Thin solid lines: effects of adding the unidentified sources to each bin, weighting by the comoving volume on each redshift bin, assuming that all the unidentified sources are obscured (lower line) or unobscured (upper line) AGN. Dashed line: Predicted ratio as a function of redshift for a unified model in which the ratio (geometry) depends only on luminosity, not redshift. That the data points lie systematically above our model is not unexpected, since obscured AGN are preferentially missed. The significant incompleteness at $z > 1.5$ makes it impossible, given the current data, to rule out a constant ratio with redshift.

in the Universe.

ET would like to thank the support of Fundación Andes, Centro de Astrofísica FONDAP and the Sigma-Xi foundation through a Grant in-aid of Research. This work was supported in part by NASA grant HST-GO-09425.13-A.

References

- Barger, A. J., Cowie, L. L., Mushotzky, R. F., Yang, Y., Wang, W.-H., Steffen, A. T., & Capak, P. 2005, *AJ*, 129, 578
- Nenkova, M., Ivezić, Ž., & Elitzur, M. 2002, *ApJ*, 570, L9
- Treister, E. et al. 2004, *ApJ*, 616, 123
- Treister, E., & Urry, C. M. 2005, *ApJ*, 630, 115
- Ueda, Y., Akiyama, M., Ohta, K., & Miyaji, T. 2003, *ApJ*, 598, 886
- Vanden Berk, D. E. et al. 2001, *AJ*, 122, 549

MEDIUM-DEEP OBSERVATIONS OF QSOS/AGNS IN THE FIELD OF SA 57

D. Trevese¹, F. Fiore², S. Puccetti², M. Tomei¹, F. Vagnetti³

¹ Dip. Fisica - Università di Roma "La Sapienza", P.le A. Moro 2, I-00185 Roma, Italy

² INAF - Osservatorio Astronomico di Roma, via Frascati 33, I-00044 Monteporzio, Italy

³ Dip. Fisica - Università di Roma "Tor Vergata", via della Ricerca Scientifica 1, I-00133 Roma, Italy

ABSTRACT

The Selected Area 57 is one of the best studied fields of the sky at all wavelengths and AGN samples have been selected with different techniques, including optical variability. We present preliminary analysis of a medium-deep XMM-Newton observation of the field, yielding 140 X-ray sources, 90 of which are identified in the optical band.

Key words: Active Galactic Nuclei; X-ray surveys.

1. INTRODUCTION

In recent years consensus has grown on a fast increase in cosmic time of the number density of QSOs, down to $z \sim 3$, followed by a slower decline of the luminosity function (LF), which can be described by a QSO luminosity evolution. The quantification of this behavior is currently based on the 2QZ survey (Croom et al. 2001) for $z < 2$, on Warren et al. (1994) and Schmidt et al. (1995) surveys for $z > 3$ and, most recently, on SDSS data (Fan et al. 2001) for $z > 4$. None of the above surveys adequately covers the redshift region $z \sim 2 - 3$ where the maximum of QSOs density is located. Moreover, higher redshift data are restricted to the bright end of QSO LF and even low redshift data do not sample the evolution of objects fainter than $M_B \sim -23$. While the evolution of the number density of *high luminosity, X-ray selected*, AGNs resembles that of optically selected quasars (Fiore et al. 2003), little is known about the evolution of *low luminosity, optically selected* AGNs, because *standard color techniques cannot be used when the nuclear luminosity becomes smaller than the host galaxy luminosity*. The most accurate location to date of the time of maximum QSO number density is provided by Wolf et al. 2003, through a color-selected sample which extends down to $M_B > -21.5$. Fainter AGNs in the field of SA 57 were selected by Bershadsky, Trevese, & Kron (1998) (BTK) searching for *variable galaxies*, i.e. active nuclei

comparable or fainter than their host galaxy, monitored in ~ 15 years of observations at Kitt Peak National Observatory (KPNO) 4m telescope, reaching so far a limit of $M_B < -19$, after the spectroscopical confirmation of the 5 brightest objects of the sample. While hard X-ray selected samples are, confirming the predictions of standard AGN synthesis models for the CXB (e.g. Comastri et al. 2001) somewhat surprising results are also emerging: 1) the sources making the CXB peak at a redshift ($z \sim 1$) lower than predicted by synthesis models (e.g. Hasinger 2003); 2) there is evidence that low luminosity sources peak at later cosmic time (Hasinger 2003, Fiore et al. 2003). Understanding the evolution of faint AGN, particularly around the epoch of maximum density, requires the analysis of a field where deep AGN samples *selected in both optical and X-ray bands* are present, to allow an accurate break down in classes of object like QSOs, different types of Seyfert galaxies, star-burst galaxies, LINERs and possibly obscured *quasar-2* type objects.

2. THE SELECTED AREA 57

The Selected Area 57 is one of the best studied fields of the sky at all wavelengths: radio FIRST Survey (Becker et al. 1995), IR deep ISOPHOT Survey (Lynden-Vornle et al. 2000), soft X-ray ROSAT HRI (Miyaji et al. 1997). A field of ~ 35 arcmin in diameter has been repeatedly observed since 1975 in the U , B_J , R_F , I_N bands. In a series of papers (Koo, Kron & Cudworth 1996 ; Koo & Kron 1988 ; Trevese et al. 1989, 1994; Bershadsky et al. 1998 (BTK)) a number of search techniques for QSOs/AGNs detection to faint limits ($B=22.5$) has been elaborated, including non-stellar color, absence of proper motion, and variability. In January 2005 we observed the field of SA 57 for 65 ks with XMM-Newton. We present preliminary results concerning the optical identification and classification of the detected sources. We detected a total of 140 sources on four images obtained in the 0.5-10, 0.5-2, 2-10, 5-10 keV bands by combining MOS1, MOS2 and PN data. The flux limit in the 2-10 keV band is approximately $4 \cdot 10^{-15}$ erg cm⁻² s⁻¹ at $S/N \sim 3$. The

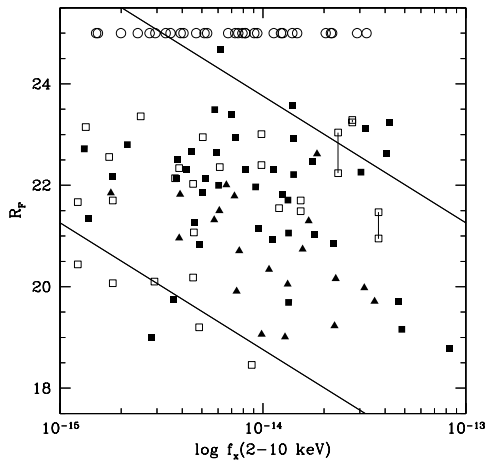


Figure 1. The optical R_F magnitude versus X-ray (2-10 keV) flux. Filled symbols: secure identifications, open symbols: less secure identifications; triangles: QSOs, squares: other identified objects; connected points: ambiguous identifications; open circles: optically unidentified.

photographic survey of SA57 has been conducted with the prime focus camera at KPNO since 1974 and is described in and Koo (1986). A photometric catalogue of about 8000 objects in a field of $\sim 0.3 \text{ deg}^2$, complete to $B_J \sim 23$ was used for optical identifications of the X-ray detected sources. Six sources not identified within the above list were identified with NGPFG objects (Infante et al. 1995). A total of 99 objects has been identified with optical sources. Of these, 74 are the most secure identifications (single optical sources within 5 arcsec from the X-ray position), 25 are less secure or ambiguous and 41 are not identified. Of the 74 most secure identifications 24 are confirmed QSOs/AGNs and 1 is the extended source corresponding to the galaxy cluster II Zw 1305.4+2941 at $z = 0.24$. The surface density of all X-ray sources is about 700 deg^{-2} , of which 290 deg^{-2} are detected in the 2-10 keV band. For comparison with previous studies (Mignoli et al. 2004), we report in Figure 1 the R_F magnitude versus the 2-10 keV flux. Most of the objects not detected in optical images, and reported as upper limits $R_F > 25 \text{ mag}$, have an X-ray to optical ratio $X/O > 30$ and are good *quasar-2* candidates, according to Fiore et al. (2003). An analysis of the X-ray spectra is in progress. Of the 42 confirmed QSOs/AGNs of the optical SA 57 survey (40 from Trevese et al. 2001), 29 fall within the X-ray field: 26 point-like objects, and 3 variable galaxies belonging to the BTK sample. Of the 26 point-like QSOs in the XMM field, 25 are detected as X-ray sources, i.e. 96%. Of the 3 variable extended BTK sources only 2 are detected in X-ray band. The third, BTK 512, has a secure redshift $z = 0.215$ and observed variability of the optical spectrum. Other 3 non confirmed BTK objects are detected in X-rays, supporting their AGN character.

3. CONCLUSIONS

- The large amount of data available in the field of SA 57 allows to detect and classify at once a large fraction of the X-ray detected objects.
- The present X-ray survey, with 58 objects detected in the hard 2-10 keV band in $\sim 0.2 \text{ deg}^2$, is slightly deeper than the HELLAS2XMM 1dF survey (Fiore et al. 2003) which contains 122 sources in 0.9 deg^2 .
- The distribution of the sources in the R_F vs $F_x(2-10 \text{ keV})$ plane, shows the existence of ~ 20 *quasar-2* candidates with high X/O ratio.
- Virtually all the point-like AGNs in the field are detected in X-rays.
- We detect altogether 9 objects found through variability (extended (BTK), or point-like (Trevese et al. 1989)) and not detected by colors or other techniques.
- Deep K-band images ($K \sim 24$) of this field are highly desirable to further investigate the possible *quasar-2* character of the high X/O sources.
- Spectroscopy of the unconfirmed variable galaxies, as well as of the remaining optically identified X-ray sources, is needed to constrain the cosmic evolution of the faint AGNs in both optical and X-ray bands.

REFERENCES

- Becker et al. 1995, ApJ, 450, 559
 Bershadsky, Trevese, Kron 1998, ApJ, 496, 103 (BTK)
 Comastri et al. 2001, MNRAS, 327, 781
 Croom et al. 2001, MNRAS, 322, L29
 Damiani et al. 1997, ApJ, 483, 370
 Fan et al. 2001, AJ, 121, 54
 Fiore et al. 2003, A&A, 409, 79
 Hasinger 2003, AIP Conf. Proc., 666, 227
 Infante et al. 1995 J. Astron. Data (JAD), 1, 2
 Koo 1986, ApJ, 311, 651
 Koo & Kron 1988, ApJ, 325, 92
 Koo, Kron & Cudworth 1996, PASP, 98, 28
 Lynden-Vornle et al. 2000, A&A, 359, 51
 Mignoli et al. 2004 A&A 418, 827
 Miyaji et al. 1997, A&A, 323, L37
 Schmidt et al. 1995, AJ, 110, 68
 Trevese et al. 1989, AJ, 98, 108
 Trevese et al. 1994, ApJ, 433, 494
 Trevese et al. 2001, ApJ, 551, 103
 Warren et al. 1994, ApJ, 421, 412
 Wolf et al. 2003 A&A, 408, 499

THE EXTENDED CHANDRA DEEP FIELD-SOUTH SURVEY: OPTICAL PROPERTIES OF X-RAY DETECTED SOURCES

Shanil Virani¹, Ezequiel Treister^{1,2}, C. Megan Urry¹, Eric Gawiser¹, and the MUSYC Collaboration³

¹Department of Astronomy, Yale University

²Departamento de Astronomia, Universidad de Chile

³<http://www.astro.yale.edu/musyc>

ABSTRACT

The Extended *Chandra* Deep Field-South (E-CDF-S) survey consists of 4 *Chandra* ACIS-I pointings and covers ≈ 1100 square arcminutes (≈ 0.3 deg²) centered on the original CDF-S field to a depth of approximately 228 ks (PI: Niel Brandt; Lehmer et al., 2005). This is the largest *Chandra* survey ever conducted at such depth. In our analysis (Virani et al., 2005), we detect 651 unique sources — 587 using a conservative source detection limit and 64 using a lower source detection limit. Of these 651 sources, 561 are detected in the full 0.5–8.0 keV band, 529 in the soft 0.5–2.0 keV band, and 335 in the hard 2.0–8.0 keV band. For point sources near the aim point, the limiting fluxes are approximately 1.7×10^{-16} erg cm⁻² s⁻¹ and 3.9×10^{-16} erg cm⁻² s⁻¹ in the 0.5–2.0 keV and 2.0–8.0 keV bands, respectively. We present the optical properties of these X-ray sources, specifically the *R*-band magnitude distribution and a preliminary spectroscopic redshift distribution. One exciting result is the discovery of 7 new Extreme X-ray-to-Optical flux ratio objects (EXOs) found in the E-CDF-S field.

Key words: diffuse radiation — surveys: observations.

1. SOURCE DETECTION

We report on the sources detected in three standard X-ray bands: 0.5–8.0 keV (full band), 0.5–2.0 keV (soft band), and 2.0–8.0 keV (hard band). To perform X-ray source detection, we applied the CIAO wavelet detection algorithm *wavdetect* using a “ $\sqrt{2}$ sequence” of wavelet scales; scales of 1, $\sqrt{2}$, 2, $2\sqrt{2}$, 4, $4\sqrt{2}$, and 8 pixels were used. Our criterion for source detection is that a source must be found with a false-positive probability threshold (p_{thresh}) of 1×10^{-7} in at least one of the three standard bands. We also produced a second catalog using a more liberal probability threshold of 1×10^{-6} . This scheme resulted in a total of 651 unique X-ray sources detected in the E-CDF-S survey field (Virani et al., 2005)¹. Figure 1 presents the hard X-ray flux versus the *R*-band magnitude.

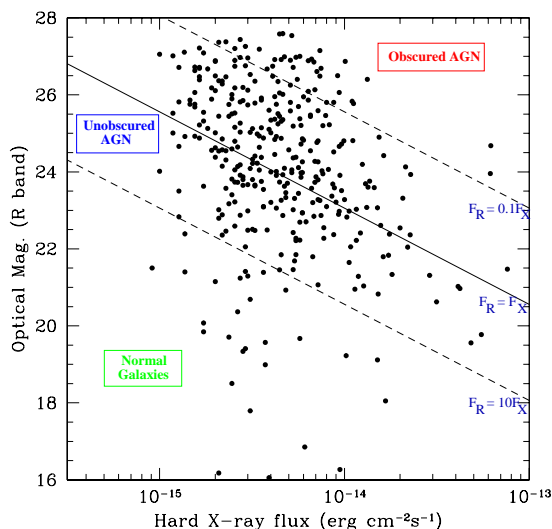


Figure 1. 2–8 keV flux vs. *R*-band magnitude (AB) for sources in the E-CDF-S. Unobscured AGN typically populate the region between the dashed lines, while obscured AGN typically lie above this region, and “normal” galaxies lie below this region.

2. MULTIWAVELENGTH SURVEY BY YALE-CHILE (MUSYC)

MUSYC is a square-degree survey to AB limiting depths of U,B,V,R=26 and K=22 (K=23 in the central $10' \times 10'$ of each field), with extensive follow-up spectroscopy (Gawiser et al., 2005). Table 1 lists the 5σ point source limits in each of the filters for the E-CDF-S field. The project comprises four $30' \times 30'$ fields, of which the E-CDF-S is one. Ground-based imaging has been completed and deep follow-up spectroscopy (to $R \sim 25$) is underway (Magellan/IMACS, VLT/VIMOS, Gemini/GNIRS).

3. OPTICAL COUNTERPARTS AND SPECTROSCOPY

In the primary (10^{-7}) catalog, 420 out of 587 sources (72%) have a unique optical counterpart within $1.5''$ of the X-ray source position (3 X-ray sources have multi-

¹X-ray catalog and images available at <http://www.astro.yale.edu/svirani/ecdfs>

Table 1. MUSYC-ECDFs 5σ AB Point Source Limits

BVR	U	B	V	R	I	z	NB5000
27.1	26.0	26.9	26.4	26.4	24.6	23.6	25.5

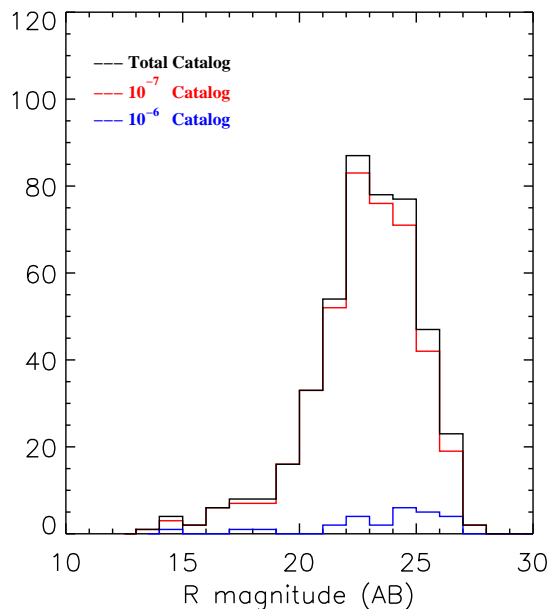


Figure 2. R -band magnitude distribution for the optical counterparts to the X-ray detected sources. Most of the sources have R -band magnitudes < 25 mag making them suitable for spectroscopic follow-up.

ple optical counterparts) in the deep MUSYC catalog of 84,410 BVR -selected sources. In the secondary (10^{-6}) catalog, 26 out of 64 sources (41%) have unique optical counterparts. Figure 2 shows the R -band magnitude distribution for these sources. Figure 3 shows the spectroscopic redshift distribution for 91 X-ray sources obtained thus far. Most are broad line, unobscured AGN (Figure 4). Additional spectroscopic observation runs are scheduled. Lastly, there are 7 sources, referred to as Extreme X-ray-to-Optical flux ratio objects (EXOs; Koekemoer et al., 2004), that are undetected in the deep BVR imaging but are robustly detected in MUSYC K -band imaging of this field (Virani et al, in prep).

REFERENCES

- Gawiser, E. et al. 2005, ApJS, in press, astro-ph/0509202
- Koekemoer, A. et al. 2004, ApJ, 600, L123
- Lehmer, B. D. et al. 2005, ApJ, in press
- Szokoly, G. P. et al. 2004, ApJS, 155, 271.
- Virani, S. N. et al. 2005, AJ submitted, astro-ph/0506551

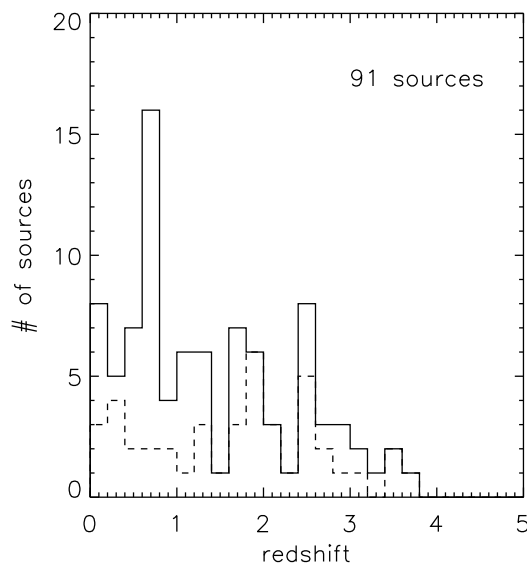


Figure 3. Spectroscopic redshifts for 91 X-ray sources in the E-CDF-S (solid line). This plot includes ~ 50 redshifts from the Szokoly et al. (2004) catalog, as well as ~ 40 redshifts determined from Magellan/IMACS spectroscopy (dashed line) performed as part of the MUSYC survey.

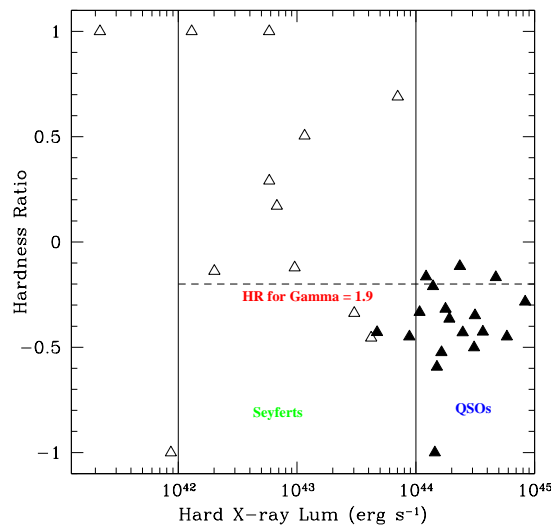


Figure 4. Hardness ratio vs. the hard X-ray luminosity for the ~ 40 sources for which spectroscopic redshifts were determined as part of the MUSYC survey. Early results indicate that luminous AGN are less obscured; more obscured AGN at low luminosities. This is partly a selection effect and partly real.